Resonance fluorescence of novel quantum emitters

Rima Al-Khuzheyri

Submitted for the degree of Doctor of Philosophy

Heriot-Watt University
School of Engineering and Physical Sciences
Institute of Photonics and Quantum Sciences

June 2016

Abstract

Quantum dots (QD) emitting near the telecommunication O-band and excitons believed to be localized on defects in WSe_2 monolayers are investigated using optical spectroscopy and resonance fluorescence (RF). The development of light sources emitting around 1300 nm is motivated primarily by the possibility of their use in information communication applications. The results presented in this thesis pave the way towards coherently generated indistinguishable single photons and entangled photon pairs at telecom wavelengths. WSe_2 monolayers are highly stable and are characterized by a higher extraction efficiency of photons compared to photon sources embedded in bulk materials. The experiments on confined excitons described here set the stage for the characterization of the effect of valley pseudospin on localized exciton emission properties.

A perturbative Coulomb blockade model is applied to telecom wavelength QDs to extract confinement and interaction energies, demonstrating that carriers are in the strong confinement regime. To examine the effect of strong confinement on carrier properties, photoluminescence (PL) spectroscopy of single QDs in the presence of external electric and magnetic fields is performed, and the permanent dipole moment, polarizability, diamagnetic coefficient, and g-factor of excitons localized within them are measured. Temporal measurements on neutral and charged excitons are performed, and a bi-exponential decay is observed in the former case, which necessitates a spin-flip interaction with the Fermi sea.

RF of telecom wavelength QDs is demonstrated, and numerical simulations are used to characterize the effect of spectral fluctuations resultant from charge noise on RF linewidth. Performing high-resolution spectroscopy, the Mollow triplet is observed and dephasing in the system is shown to be negligible.

Second-order correlation function measurements of emission from a localized exciton in a WSe_2 monolayer cooled to 4 K under non-resonant and resonant excitation

demonstrate its single photon nature. High-resolution PL excitation spectroscopy is used to identify a weakly-fluorescent exciton state blue-shifted from the ground-state exciton. Resonance excitation of the blue-shifted exciton is shown to produce single photons of high purity from the lowest energy exciton state.

Acknowledgements

First of all, I would like to thank my supervisor Professor Brian D. Gerardot for providing me with an opportunity to work in a world-class laboratory and his guidance throughout my PhD. Additionally, I extend my thanks to my second supervisor Dr Paul Dalgarno, who had been a source of inspiration and support. Finally, my thanks go to all current and former members of our research group that I have had an opportunity to work with over the last four years, in particular, Dr Luca Sapienza for his instruction and patience in the early stages of my PhD.

ACADEMIC REGISTRY
Research Thesis Submission

Name:	Rima Al-Khuzheyri		
School/PGI:	School of Engineering and Physical Sciences		
Version: *(i.e. First, Resubmission, Final)*	Final	Degree Sought (Award **and** Subject area)	Doctor of Philosophy, Physics

Declaration

In accordance with the appropriate regulations I hereby submit my thesis and I declare that:

1) the thesis embodies the results of my own work and has been composed by myself
2) where appropriate, I have made acknowledgement of the work of others and have made reference to work carried out in collaboration with other persons
3) the thesis is the correct version of the thesis for submission and is the same version as any electronic versions submitted*.
4) my thesis for the award referred to, deposited in the Heriot-Watt University Library, should be made available for loan or photocopying and be available via the Institutional Repository, subject to such conditions as the Librarian may require
5) I understand that as a student of the University I am required to abide by the Regulations of the University and to conform to its discipline.

* *Please note that it is the responsibility of the candidate to ensure that the correct version of the thesis is submitted.*

Signature of Candidate:		Date:	24.08.2016

Submission

Submitted By *(name in capitals):*	
Signature of Individual Submitting:	
Date Submitted:	

For Completion in the Student Service Centre (SSC)

Received in the SSC by *(name in capitals):*			
Method of Submission *(Handed in to SSC; posted through internal/external mail):*			
E-thesis Submitted ***(mandatory for final theses)***			
Signature:		Date:	

Table of contents

List of tables

List of figures

Chapter 1

Introduction

The main objective of this thesis is to characterize two types of novel quantum emitters: self-assembled InGaAs quantum dots (QDs) that emit around the telecommunication O-band ($\lambda = 1310$ nm) and excitons localized at what are believed to be crystal lattice defects in WSe_2 monolayers. The motivation behind the study of emission at telecommunication wavelengths is related to the aim of obtaining a source of single photons that can be used in secure communication and quantum computation (i.e. boson sampling), and entangled photons for use in quantum key distribution and quantum repeaters. The main benefit of WSe_2 monolayers is based on the ease of their integration on-chip, as well as the ability to deterministically position the confined quantum emitters using localized strain pockets.

This introductory chapter discusses the theory behind resonance fluorescence (RF), that is light emission from a two-level system that is the result of its interaction with a resonant optical field, and summarizes the main experimental developments in QD RF. QDs, including those emitting at telecom wavelengths, are briefly discussed. Finally, some of the reported results of experiments on two-dimensional (2D) transition metal dichalcogenide (TMD) monolayers are outlined.

1.1 A driven two-level system

Resonance fluorescence is observed when a two-level system is driven by a near-resonant electromagnetic field. A classical example of a two-level system is an atom. QDs are referred to as artificial atoms due to their discrete energy levels, and in many cases can be approximated as two-level systems. The dynamics of the interaction of a two-level system and an optical field are described in many textbooks, such

as Refs [1, 2]. In this section the theory of resonance fluorescence is examined in the semiclassical approach as presented in Ref. [1]. First, the expression for the RF spectrum from a resonantly driven two-level system is derived by considering the Hamiltonian describing the interaction of a two-level system with a driving field (Section 1.1.1) and the electric field operator (Section 1.1.2). Secondly, the derivation for the normalized second order correlation function is outlined.

1.1.1 Interaction Hamiltonian

In the dipole approximation the driving field of a two-level system is considered to be constant throughout. The Hamiltonian describing the interaction of a two-level system containing one electron and a multi-mode field $\mathbf{E}$ can be written as the sum of three parts:

$$\hat{\mathcal{H}} = \hat{\mathcal{H}}_{atom} + \hat{\mathcal{H}}_{field} - e\mathbf{r} \cdot \mathbf{E}. \tag{1}$$

The first two parts are the Hamiltonians of the non-interacting two-level system and driving field, and $e\mathbf{r}$ is the dipole moment of the two-level system.

Using the creation and annihilation operators $\hat{a}^\dagger_{\mathbf{k}}$ and $\hat{a}_{\mathbf{k}}$, where $\mathbf{k}$ is the wave vector, the non-interaction Hamiltonian of the field can be written as

$$\hat{\mathcal{H}}_{field} = \sum_{\mathbf{k}} \hbar\nu_k \left(\hat{a}^\dagger_{\mathbf{k}} \hat{a}_{\mathbf{k}} + \frac{1}{2} \right). \tag{2}$$

The non-interaction Hamiltonian of the atom can be written in the following form using the atom transition operator $\hat{\sigma}_{ij} = |i\rangle \langle j|$ and the expression $\hat{\mathcal{H}}_{atom} |i\rangle = E_i |i\rangle$:

$$\hat{\mathcal{H}}_{atom} = \sum_i E_i |i\rangle \langle i| = \sum_i E_i \hat{\sigma}_{ii}. \tag{3}$$

The sum is performed over all the levels of the system i.

As $\sum_i |i\rangle \langle i| = 1$, the dipole component of the Hamiltonian can be rewritten as

$$e\mathbf{r} = \sum_{i,j} e |i\rangle \langle i| \mathbf{r} |j\rangle \langle j| = \sum_{i,j} \wp_{ij} \hat{\sigma}_{ii}. \tag{4}$$

Here the electric-dipole transition matrix element for the two levels is written as $\wp_{ij} = e \langle i| \mathbf{r} |j\rangle$.

The quantized electric field is given by the following:

$$\mathbf{E} = \sum_{\mathbf{k}} \hat{\epsilon}_{\mathbf{k}} \mathcal{E}_{\mathbf{k}} (\hat{a}_{\mathbf{k}} + \hat{a}^\dagger_{\mathbf{k}}). \tag{5}$$

Here $\hat{\epsilon}_{\mathbf{k}}$ is the unit polarization vector, $\mathcal{E}_{\mathbf{k}} = (\hbar\nu_k/2\epsilon_0 V)^{1/2}$ has the dimensions of an electric field, ϵ_0 is the vacuum permittivity, and V has the dimensions of a volume.

Using Eqs 2 to 5 and introducing $g_{\mathbf{k}}^{ij} = -\hat{\wp}_{ij} \cdot \hat{\epsilon}_{\mathbf{k}}\mathcal{E}_{\mathbf{k}}/\hbar$, Eq. 1 can be rewritten as

$$\hat{\mathcal{H}} = \sum_{\mathbf{k}} \hbar\nu_k \hat{a}_{\mathbf{k}}^\dagger \hat{a}_{\mathbf{k}} + \sum_i E_i \hat{\sigma}_{ii} + \hbar \sum_{i,j} \sum_{\mathbf{k}} g_{\mathbf{k}}^{ij} \hat{\sigma}_{ii} (\hat{a}_{\mathbf{k}} + \hat{a}_{\mathbf{k}}^\dagger). \tag{6}$$

For a two-level system ($\hat{\wp}_{ab} = \hat{\wp}_{ba}$) Eq. 6 can be rewritten as

$$\hat{\mathcal{H}} = \sum_{\mathbf{k}} \hbar\nu_k \hat{a}_{\mathbf{k}}^\dagger \hat{a}_{\mathbf{k}} + (E_a \hat{\sigma}_{aa} + E_b \hat{\sigma}_{bb}) + \hbar \sum_{\mathbf{k}} g_{\mathbf{k}} (\hat{\sigma}_{ab} + \hat{\sigma}_{ba})(\hat{a}_{\mathbf{k}} + \hat{a}_{\mathbf{k}}^\dagger). \tag{7}$$

Next, the following operators are introduced: $\hat{\sigma}_z$; $\hat{\sigma}_+$, which transfers the system from the excited to the ground state; and $\hat{\sigma}_-$, which does the opposite:

$$\hat{\sigma}_z = \hat{\sigma}_{aa} - \hat{\sigma}_{bb}; \tag{8}$$

$$\hat{\sigma}_+ = \hat{\sigma}_{ab}; \tag{9}$$

$$\hat{\sigma}_- = \hat{\sigma}_{ba}. \tag{10}$$

Using expressions $E_a - E_b = \hbar\omega$, where ω is the atomic transition frequency, and $\hat{\sigma}_{aa} + \hat{\sigma}_{bb} = 1$, and applying the rotating-wave approximation, Eq. 7 can be rewritten as

$$\hat{\mathcal{H}} = \sum_{\mathbf{k}} \hbar\nu_k \hat{a}_{\mathbf{k}}^\dagger \hat{a}_{\mathbf{k}} + \frac{1}{2}\hbar\omega\hat{\sigma}_z + \hbar \sum_{\mathbf{k}} g_{\mathbf{k}} (\hat{\sigma}_+ \hat{a}_{\mathbf{k}} + \hat{a}_{\mathbf{k}}^\dagger \hat{\sigma}_-). \tag{11}$$

The rotating-wave approximation allows to neglect the rapidly oscillating terms that have an average equal to zero over long timescales. Applying the rotating-wave approximation in this procedure corresponds to eliminating the energy-non-conserving terms in the Hamiltonian such as $\hat{\sigma}_- \hat{a}_{\mathbf{k}}$ (net loss of $2\hbar\omega$) and $\hat{\sigma}_+ \hat{a}_{\mathbf{k}}^\dagger$ (net gain of $2\hbar\omega$).

1.1.2 Electric field operator

The operator for a quantized electric field can be written in the following form:

$$\hat{\mathbf{E}}(\mathbf{r}, t) = \hat{\mathbf{E}}^+(\mathbf{r}, t) + \hat{\mathbf{E}}^-(\mathbf{r}, t). \tag{12}$$

Here the positive and negative frequency contributions are

$$\hat{\mathbf{E}}^+(\mathbf{r}, t) = \sum_{\mathbf{k},p} \hat{\epsilon}_{\mathbf{k}}^{(p)} \mathcal{E}_{\mathbf{k}} \hat{a}_{\mathbf{k},p}(t) e^{i\mathbf{k}\cdot\mathbf{r}}; \tag{13}$$

$$\hat{\mathbf{E}}^-(\mathbf{r}, t) = \sum_{\mathbf{k},p} \hat{\epsilon}_{\mathbf{k}}^{(p)} \mathcal{E}_{\mathbf{k}} \hat{a}_{\mathbf{k},p}^\dagger(t) e^{-i\mathbf{k}\cdot\mathbf{r}}. \tag{14}$$

For a two-level system interacting with a driving field, operators $\hat{a}_{\mathbf{k},p}$ and $\hat{\sigma}_-$, where p is the polarization, can be written as

$$\hat{a}_{\mathbf{k},p}(t) = \hat{\tilde{a}}_{\mathbf{k},p}(t)e^{-i\nu_k t}; \tag{15}$$

$$\hat{\sigma}_- = \hat{\tilde{\sigma}}_-(t)e^{-i\omega t}. \tag{16}$$

Writing the Heisenberg equations of motion for operators in Eqs 15, 16 and applying an integration procedure to them, Eq. 13 can be written in the following form:

$$\hat{\mathbf{E}}^+(\mathbf{r},t) = \left(\frac{i}{16\pi^3\epsilon_0}\right) e^{-i\omega t} \int d^3k \sum_p \hat{\epsilon}^p_{\mathbf{k}}[\epsilon^p_{\mathbf{k}} \cdot \hat{\wp}]\nu_k e^{i\mathbf{k}\cdot(\mathbf{r}-\mathbf{r}_0)} \int_0^t dt' \hat{\tilde{\sigma}}_-(t') e^{i(\omega-\nu_k)(t-t')}. \tag{17}$$

Here the sum over indices $\mathbf{k}$ has been replaced with an integral.

Using the expression $\sum_p \hat{\epsilon}^{(p)}_{\mathbf{k}} \hat{\epsilon}^{(p)}_{\mathbf{k}} = 1 - \mathbf{kk}/k^2$ and defining vectors $\mathbf{k}$ and $\hat{\wp}$ in polar coordinates in such a way that the z-axis is aligned with the vector $|\mathbf{r}-\mathbf{r}_0|$, and the dipole is positioned in the xz-plane forming an angle η with the z axis, the integrals in Eq. 17 can be evaluated to obtain the following:

$$\hat{\mathbf{E}}^+(\mathbf{r},t) = \left(\frac{c\hat{\wp}\sin\eta\ \hat{x}}{8\pi^2\epsilon_0\,|\mathbf{r}-\mathbf{r}_0|}\right) e^{-i\omega t} \int_0^\infty dk k^2 \left(e^{ik|\mathbf{r}-\mathbf{r}_0|} - e^{-ik|\mathbf{r}-\mathbf{r}_0|}\right) \times \\ \times \int_0^t dt' \hat{\tilde{\sigma}}_-(t') e^{i(\omega-\nu_k)(t-t')}. \tag{18}$$

Performing integration over k Eq. 18 becomes

$$\hat{\mathbf{E}}^+(\mathbf{r},t) = \left(\frac{c\hat{\wp}\sin\eta\ \hat{x}}{8\pi^2\epsilon_0\,|\mathbf{r}-\mathbf{r}_0|}\right) \times \\ \times \left[e^{-i\omega(t-|\mathbf{r}-\mathbf{r}_0|/c)} \int_0^t dt' \hat{\tilde{\sigma}}_-(t') \delta\left(t - t' - \frac{|\mathbf{r}-\mathbf{r}_0|}{c}\right) - \right. \\ \left. - e^{-i\omega(t+|\mathbf{r}-\mathbf{r}_0|/c)} \int_0^t dt' \hat{\tilde{\sigma}}_-(t') \delta\left(t - t' + \frac{|\mathbf{r}-\mathbf{r}_0|}{c}\right)\right]. \tag{19}$$

Using Eq. 16 to reintroduce $\hat{\sigma}_-$ and eliminating the incoming wave contribution, the following expression for the far field is obtained:

$$\hat{\mathbf{E}}^+(\mathbf{r},t) = \frac{\omega^2\hat{\wp}\sin\eta\ \hat{x}\hat{\sigma}_-}{4\pi\epsilon_0 c^2\,|\mathbf{r}-\mathbf{r}_0|} \left(t - \frac{|\mathbf{r}-\mathbf{r}_0|}{c}\right) \sim \hat{\sigma}_-. \tag{20}$$

The above shows that the scattered field in the far field is polarized in the x-direction.

1.1.3 RF spectral properties in a weak driving field

If a weak resonant field ($\Omega_R \ll \Gamma/4$) characterized by bandwidth D and central frequency ν interacts with a two-level system with bandwidth Γ and central frequency ω, the expression for the light scattered off the field induced dipole is given in Eq. 20. The expectation value of $\hat{\mathbf{E}}^+(\mathbf{r},t)$ can be approximated as

$$\left\langle \hat{\mathbf{E}}^+(\mathbf{r},t) \right\rangle \sim \langle \hat{\sigma}_-(t) \rangle = \rho_{ab}(t). \tag{21}$$

Here ρ_{ab} is an element of the density operator, which can be written in matrix form as

$$\rho = \begin{bmatrix} \rho_{aa} & \rho_{ab} \\ \rho_{ba} & \rho_{bb} \end{bmatrix}. \tag{22}$$

The diagonal elements determine the probability of finding the electron in the ground and excited states, and the off diagonal elements indicate atomic polarization.

After applying the rotating-wave approximation, at long timescales $t \gg \Gamma^{-1}$ the following result is obtained:

$$\left\langle \hat{\mathbf{E}}^+(\mathbf{r},t) \right\rangle \sim \langle \hat{\sigma}_- \rangle = \rho_{ab}(t) = \frac{-i\Omega_R e^{-i\nu t}}{2i(\omega-\nu)+\Gamma} \left[\rho_{aa}(0) - \rho_{bb}(0)\right]. \tag{23}$$

Here the Rabi frequency is defined as $\Omega_R = \hat{\wp}\mathcal{E}/\hbar$. Eq. 23 shows that the oscillation frequency of the electric field induced dipole is determined by the driving field, and the scattered light has the same bandwidth as the driving field for $\Omega_R \ll \Gamma$.

1.1.4 RF spectral properties in a strong driving field

The weak driving field approximation is no longer valid when $\Omega_R \geq \Gamma/4$, in other words, when the Rabi frequency becomes much larger than the linewidth of the transition. The interaction of a strong driving field with a two-level system can be considered in the dressed state model.

For the interaction of a single-mode field characterized by frequency ν with a two-level system, Eq. 11 can be rewritten as

$$\hat{\mathcal{H}} = \hbar\nu\hat{a}^\dagger\hat{a} + \frac{1}{2}\hbar\omega\hat{\sigma}_z + \hbar g(\hat{\sigma}_+\hat{a} + \hat{a}^\dagger\hat{\sigma}_-). \tag{24}$$

The part of the Hamiltonian that corresponds to the interaction of the driving field with the system is $\mathcal{V} = \hbar g\left(\hat{\sigma}_+\hat{a} + \hat{a}^\dagger\hat{\sigma}_-\right)$, and its eigenstates are

$$|\pm, n\rangle = \frac{|a,n\rangle \pm |b,n+1\rangle}{\sqrt{2}}. \tag{25}$$

According to Eq. 25 upon interacting with a strong driving field the two levels in the system each split into a doublet. The eigenvalues that correspond to eigenstates in Eq. 25 are $\pm\hbar g\sqrt{n+1} = \pm\hbar\Omega_R/2$, and Ω_R corresponds to the splitting of the states within each doublet. These matter-light modes are referred to as dressed states [3]. Considering the dressed state picture, the system emission under a strong driving field has three peaks, consisting of a central peak at frequency ν and two sidebands at frequencies $\nu \pm \Omega_R$, referred to as the Mollow triplet. The intensity of the central peak equals to twice the intensity of each of the sidebands.

1.1.5 RF spectrum for a resonantly driven two-level system

The RF spectrum of light emitted from a two-level system along the x-axis upon interaction with a driving field is given by the following expression:

$$S(\mathbf{r},\omega_0) = \frac{1}{\pi} Re \int_0^\infty d\tau \left\langle E^-(\mathbf{r},t)E^+(\mathbf{r},t+\tau)\right\rangle e^{i\omega_0\tau} = \\ = \frac{1}{\pi} Re \int_0^\infty d\tau I_0(\mathbf{r}) \left\langle \hat{\sigma}_+(t)\hat{\sigma}_-(t+\tau)\right\rangle e^{i\omega_0\tau}; \quad (26)$$

$$I_0(\mathbf{r}) = \left(\frac{\omega^2 \hat{\wp} \sin\eta}{4\pi\epsilon_0 c^2 |\mathbf{r}-\mathbf{r}_0|}\right)^2. \quad (27)$$

For a field in the steady state, where parameters are time-independent, the two-time correlation function $\langle\hat{\sigma}_+(t)\hat{\sigma}_-(t+\tau)\rangle$ is dependent on only τ. Here the angle brackets indicate an ensemble average, and this expression can be written as

$$\langle\hat{\sigma}_+(t)\hat{\sigma}_-(t+\tau)\rangle = \frac{1}{T}\int_0^T \hat{\sigma}_+(t)\hat{\sigma}_-(t+\tau)dt. \quad (28)$$

The values of all higher order correlation functions including of that in Eq. 26 can be calculated by the quantum regression theorem using the single-time correlation functions. The obtained result is written in the following form:

$$\left\langle E^-(\mathbf{r},t)E^+(\mathbf{r},t+\tau)\right\rangle = I_0(\mathbf{r})\left\langle\hat{\sigma}_+(t)\hat{\sigma}_-(t+\tau)\right\rangle = I_0(\mathbf{r})e^{-i\omega\tau}\left(\frac{\Omega_R^2}{\Gamma^2+2\Omega_R^2}\right)\times \\ \times\left\{\frac{\Gamma^2}{\Gamma^2+2\Omega_R^2} + \frac{e^{-\Gamma\tau/2}}{2} + \frac{e^{-3\Gamma\tau/4}}{4}\left[e^{-i\mu\tau}(P+iQ)+e^{i\mu\tau}(P-iQ)\right]\right\}. \quad (29)$$

Here the constants P and Q are

$$P = \frac{2\Omega_R^2-\Gamma^2}{2\Omega_R^2+\Gamma^2}; \quad (30)$$

$$Q = \left(\frac{\Gamma}{4\mu}\right)\left(\frac{10\Omega_R^2-\Gamma^2}{2\Omega_R^2+\Gamma^2}\right); \quad (31)$$

$$\mu = \left(\Omega_R^2 - \frac{\Gamma^2}{16}\right)^{1/2}. \quad (32)$$

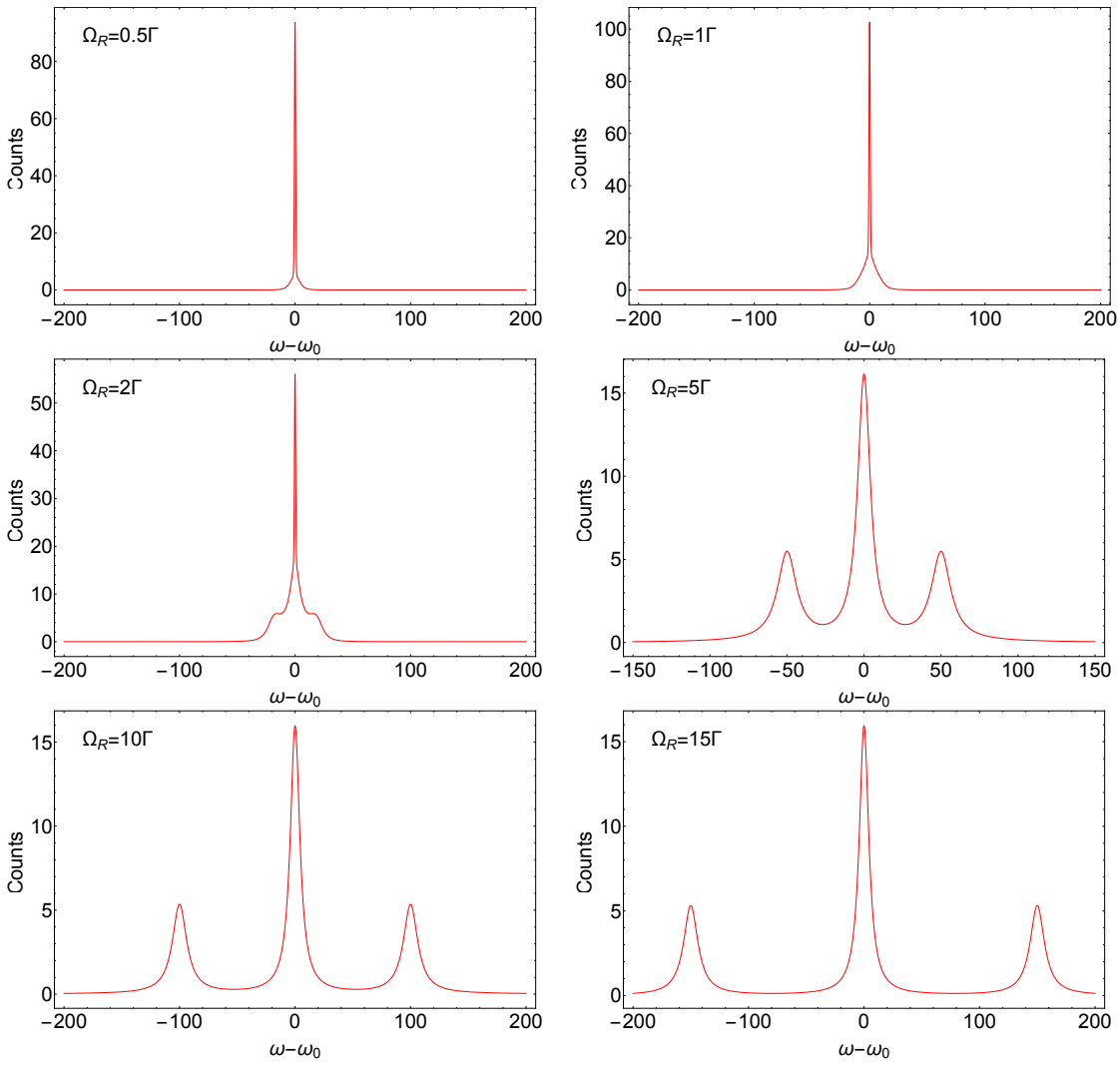

Figure 1.1: Plots showing the RF spectrum of light emitted from a driven two-level system for different Rabi frequencies. A weak driving field corresponds to $\Omega_R \leq \Gamma/4$, resulting in Rayleigh scattering. At stronger driving fields ($\Omega_R \geq \Gamma/4$) the Mollow-triplet becomes visible. In the modeling, the delta function is replaced by a Gaussian function with a narrow width due to a limit on the resolution of the image.

In a weak driving field ($\Omega_R \ll \Gamma/4$) Eq. 26 and Eq. 29 simplify to the following:

$$\left\langle E^-(\mathbf{r},t)E^+(\mathbf{r},t+\tau)\right\rangle \cong I_0(\mathbf{r})\left(\frac{\Omega_R^2}{\Gamma}\right)^2 e^{-i\omega\tau}, \tag{33}$$

$$S(\mathbf{r},\omega_0) = I_0(\mathbf{r})\left(\frac{\Omega_R^2}{\Gamma}\right)^2 \delta(\omega-\omega_0). \tag{34}$$

Eq. 34 demonstrates that upon excitation of a two-level system by a weak driving field the emission spectrum is given by a δ-function. This is the case of elastic Rayleigh scattering (see Fig. 1.1, $\Omega_R = 0.5\Gamma$), which confirms the results of Section 1.1.3.

When a two-level system is interacting with a strong driving field ($\Omega_R \geq \Gamma/4$), Eq. 26 simplifies to the following:

$$S(\mathbf{r},\omega_0) = \frac{I_0(\mathbf{r})}{4\pi}\left(\frac{\Omega_R^2}{\Gamma^2+2\Omega_R^2}\right)\times \\ \times\left\{\frac{4\pi\Gamma^2}{\Gamma^2+2\Omega_R^2}\delta(\omega-\omega_0)+\frac{\Gamma}{(\omega-\omega_0)^2+(\Gamma/2)^2}+\right. \\ \left.+\frac{\alpha_+}{(\omega+\mu-\omega_0)^2+(3\Gamma/4)^2}+\frac{\alpha_-}{(\omega-\mu-\omega_0)^2+(3\Gamma/4)^2}\right\}. \tag{35}$$

Here $\alpha_\pm = (3/4)\Gamma P \pm Q(\omega\pm\mu-\omega_0)$. Eq. 35 indicates that at stronger driving fields the emission from a two-level system becomes a combination of four peaks: two at the center frequency ω and two sidebands at $\omega\pm\Omega_R$ (see Fig. 1.1, $\Omega_R = 1\Gamma$ and $\Omega_R = 2\Gamma$). One of the central peaks is given by a δ-function, while the other has a width of $\Gamma/2$. The width of the sideband peaks is $3\Gamma/4$. In the case of very strong driving fields ($\Omega_R \gg \Gamma/4$) the elastic peak disappears (see Fig. 1.1, $\Omega_R = 5\Gamma$, $\Omega_R = 10\Gamma$, and $\Omega_R = 15\Gamma$) and the ratio of intensities of the central peak to one of the sidebands is 3 : 1 (ratio of integrated intensities is 2 : 1):

$$S(\mathbf{r},\omega_0) = \frac{I_0(\mathbf{r})}{8\pi}\times\left\{\frac{\Gamma}{(\omega-\omega_0)^2+(\Gamma/2)^2}+\right. \\ \left.+\frac{3\Gamma/4}{(\omega+\Omega_R-\omega_0)^2+(3\Gamma/4)^2}+\frac{3\Gamma/4}{(\omega-\Omega_R-\omega_0)^2+(3\Gamma/4)^2}\right\}. \tag{36}$$

These results are in line with the conclusions of Section 1.1.4.

In summary, elastic scattering from a two-level system occurs when a low intensity monochromatic beam is used for excitation. In this case the linewidth of emitted light is characterized by the linewidth of the incident light. At higher driving field intensities Rabi oscillations occur, broadening the linewidth, and the Mollow-triplet emission spectrum can be observed.

1.1.6 Photon antibunching

The annihilation field operator $\hat{\mathbf{E}}^{+}(\mathbf{r},t)$ is responsible for the process of generating a photoelectron in a single photon detector when detecting emission from a two-level system. A photon is detected at point $\mathbf{r}$ in the time interval from t to $t+dt$ with a probability proportional to $w_1(\mathbf{r},t)$:

$$w_1(\mathbf{r},t) = \left|\langle f|\,\hat{\mathbf{E}}^{+}(\mathbf{r},t)\,|i\rangle\right|^2 = \langle i|\,\hat{\mathbf{E}}^{-}(\mathbf{r},t)\hat{\mathbf{E}}^{+}(\mathbf{r},t)\,|i\rangle\,. \tag{37}$$

Here $|i\rangle$ and $\langle f|$ are the states of the field before and after the detection event, respectively.

Eq. 37 can be rewritten by introducing the density operator $\rho = \sum_i P_i\,|i\rangle\,\langle i|$:

$$w_1(\mathbf{r},t) = \mathrm{Tr}[\rho\hat{\mathbf{E}}^{-}(\mathbf{r},t)\hat{\mathbf{E}}^{+}(\mathbf{r},t)]. \tag{38}$$

In analogy, the joint probability of observing a detection event at point $\mathbf{r}_1$ in the time interval from t_1 to t_1+dt_1 and another at point $\mathbf{r}_2$ in the time interval from t_2 to t_2+dt_2 ($t_1 \le t_2$) is proportional to

$$\begin{aligned} w_1(\mathbf{r}_1,t_1,\mathbf{r}_2,t_2) = \left|\langle f|\,\hat{\mathbf{E}}^{+}(\mathbf{r}_2,t_2)\hat{\mathbf{E}}^{+}(\mathbf{r}_1,t_1)\,|i\rangle\right|^2 = \\ = \mathrm{Tr}[\rho\hat{\mathbf{E}}^{-}(\mathbf{r}_1,t_1)\hat{\mathbf{E}}^{-}(\mathbf{r}_2,t_2)\hat{\mathbf{E}}^{+}(\mathbf{r}_2,t_2)\hat{\mathbf{E}}^{+}(\mathbf{r}_1,t_1)]. \end{aligned} \tag{39}$$

From Eq. 39 the normalized second order correlation function can be written as

$$g^{(2)}(\mathbf{r},t) = \frac{\left\langle \hat{\mathbf{E}}^{-}(\mathbf{r},t)\hat{\mathbf{E}}^{-}(\mathbf{r},t+\tau)\hat{\mathbf{E}}^{+}(\mathbf{r},t+\tau)\hat{\mathbf{E}}^{+}(\mathbf{r},t)\right\rangle}{\left\langle \hat{\mathbf{E}}^{-}(\mathbf{r},t)\hat{\mathbf{E}}^{+}(\mathbf{r},t)\hat{\mathbf{E}}^{-}(\mathbf{r},t+\tau)\hat{\mathbf{E}}^{+}(\mathbf{r},t+\tau)\right\rangle}. \tag{40}$$

For a two-level system Eq. 40 becomes [4]

$$g^{(2)}(\tau) = 1 - \left(\cos\nu\tau + \frac{1}{2\nu}\left(\frac{1}{T_1}+\frac{1}{T_2}\right)\sin\nu\tau\right)e^{-\frac{1}{2}\left(\frac{1}{T_1}+\frac{1}{T_2}\right)\tau}; \tag{41}$$

$$\nu = \sqrt{\Omega_R^2 - \frac{1}{4}\left(\frac{1}{T_1}+\frac{1}{T_2}\right)}. \tag{42}$$

Here $T_2/2 = 1/\Gamma$. T_1 is the lifetime of the excited state and T_2 is the coherence time of emission from the system, which is the time during which the light can interfere with itself. The expression $T_2 = 2T_1$ is valid for systems with no pure dephasing. Pure dephasing is loss of coherence (or phase) not accompanied by a population transfer.

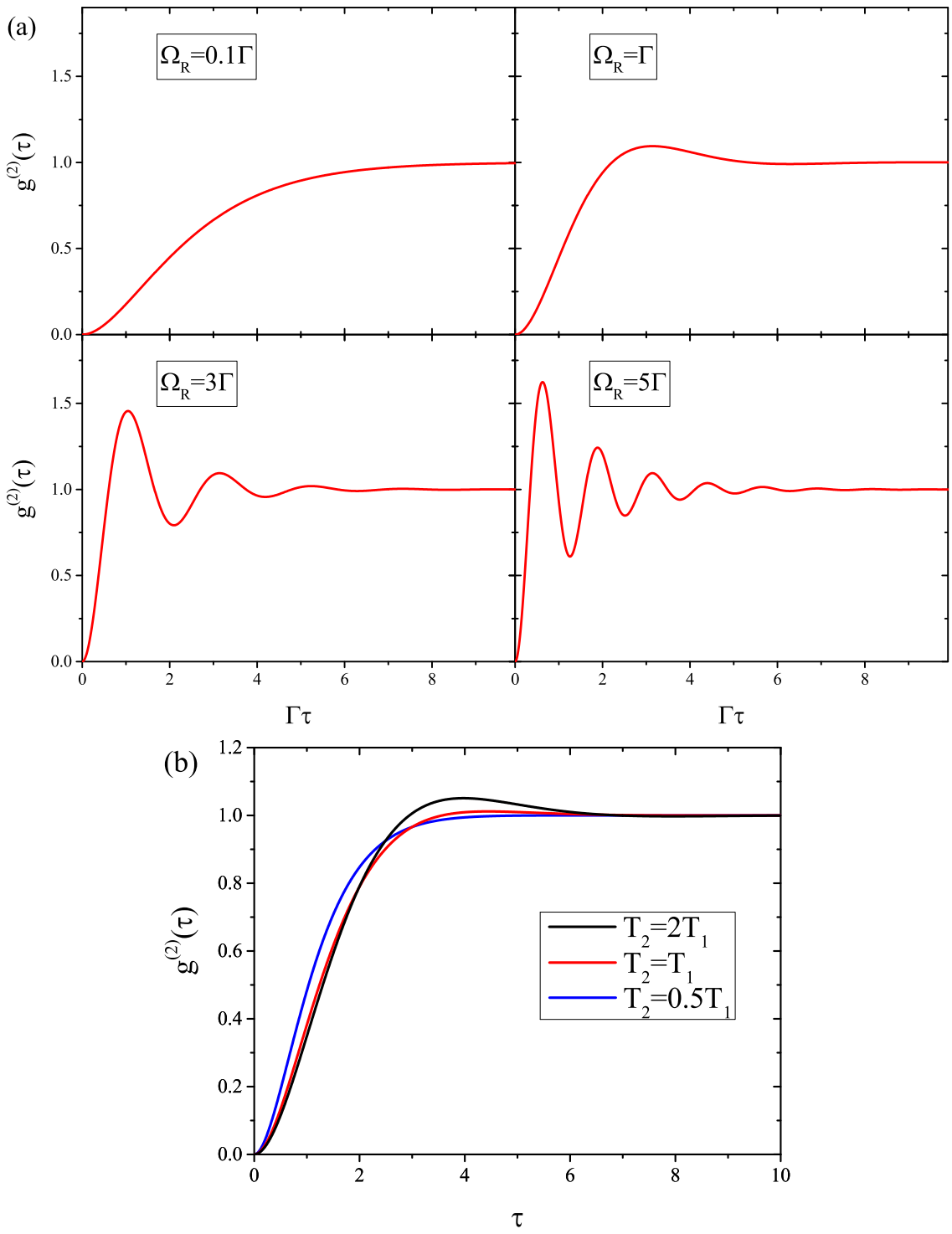

Figure 1.2: Plots showing the normalized second order correlation function of a driven two-level system for different Rabi frequencies (a) and coherence times (b). A weak driving field corresponds to $\Omega_R \leq \Gamma/4$, resulting in the gradual increase of $g^{(2)}(\tau)$ from 0 to 1 with $\Gamma\tau$. At stronger driving fields ($\Omega_R \geq \Gamma/4$) $g^{(2)}(\tau)$ oscillates around time zero.

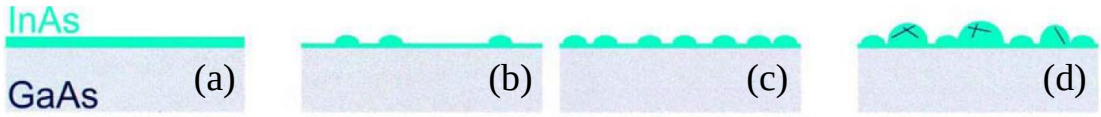

Figure 1.3: A schematic diagram illustrating self-assembled quantum dot growth. Until the QD layer thickness is about a monolayer, growth of the QD material on top of the substrate material is two-dimensional (a). At the critical thickness (about a monolayer), three-dimensional strain-free QDs begin to form (b). The density of QDs increases with layer thickness (c). At the QD layer thickness increases significantly above a monolayer, dislocations within the QDs appear (d). Figure from Ref. [8].

At time zero $g^{(2)}(0) = 0$, which is referred to as photon antibunching. The physical meaning of photon antibunching in a two-level system is that it can only emit one photon at a time, revealing its quantum behavior [3]. In weak optical fields $g^{(2)}(\tau)$ increases gradually from 0 to 1 with τ, in strong optical fields $g^{(2)}(\tau)$ is characterized by Rabi oscillations around time zero, with the oscillation amplitude decreasing as τ increases due to dephasing (see Fig. 1.2).

1.2 Overview of quantum dots

Quantum dots (QDs), also called artificial atoms, are nanometer-sized objects that are formed when a low band gap semiconductor layer is sandwiched between a higher band gap semiconductor. The charge carriers within a QD are confined in three spatial dimensions in a region the size of the particles' de Broglie wavelength, leading to the formation of discrete energy levels within the dot, similar to those of real atoms. Quasi zero-dimensional confinement results in a δ-like QD density of states and narrow linewidth optical spectra [5]. Electrons and holes relax to the ground state before recombination [5]. Typical homogeneous (natural) linewidths of QDs are about 1 μeV [6]. Homogeneous linewidths of QDs are determined by the uncertainty principle.

1.2.1 QD growth and self-assembly

Self-assembled InAs QDs on a GaAs substrate are grown in the Stranski-Krastanov growth mode by solid source molecular beam epitaxy (MBE) in a high vacuum chamber. The source materials are placed around the substrate located on a rotating platform. Heating the chambers with the solid source materials results in the evaporation of the material and its condensation on the substrate. A uniform layer thickness is produced by rotating the substrate. Alternatively, a QD density gradient is created by stopping the rotation of the substrate during QD growth.

Semiconductors InAs and GaAs have different lattice constants with a mismatch of 7%, and the QD wetting layer generally adapts the lattice constant of the substrate [7]. However, the mismatch leads to strain within the InAs wetting layer, which accumulates with layer thickness until two-dimensional planar growth is no longer possible [5]. To reduce the strain randomly distributed three-dimensional islands form [8]. A decrease of strain corresponds to an increase of surface energy and, in order to minimize the total energy of the system, the growth should be stopped upon reaching equilibrium energy between the two processes [9]. Under carefully chosen growth conditions the islands grow to be free of defects and are approximately equal-sized with linear dimensions on the order of the semiconductor exciton Bohr radius [7]. Fig. 1.3 is a diagram illustrating the Stranski-Krastanov growth mode of InAs QDs on a GaAs substrate. However, growth conditions cannot be fully controlled, leading to QDs having a distribution in size, resulting in a distribution in emission energy of excitons [7]. This effect can be observed as broad ensemble photoluminescence (PL) in a spectrum.

1.2.2 Noise in semiconductors

Two sources of noise in semiconductors can be identified. Charge noise is caused by a fluctuating electric field in the immediate surroundings of the QD, which affects it through the Stark effect and leads to shifts in transition energy, inhomogeneously broadening the emission linewidth [10], since spatially separated QDs are affected differently depending on the local electric field around each one. The effects of charge noise can be partially suppressed by working with ultra-pure materials [11]. Spin noise is a result of fluctuations in the local magnetic environment caused by fluctuating nuclear spins in the QD, which affect the transition energy via the Zeeman

effect.

1.3 Experimental observation of RF

The main benefit of RF over non-resonant microphotoluminescence (μ-PL) is enhanced coherence of the generated photons due to a decreased influence of the host material. Single indistinguishable photons can be generated on-demand [12, 13], opening up the possibilities of quantum state preparation [14], generation of polarization-entangled photon pairs [15], and quantum computing [16].

The first RF experiments were performed on beams of sodium atoms [17, 18]. In those experiments, the RF was isolated from the scattered laser light by using a cross-beam geometry, where the RF was detected along a spatial direction that is orthogonal to both the resonant excitation and sodium atomic beam directions. Since then RF has been used to probe the dynamics of many systems and in 2007 was performed on QDs for the first time.

1.3.1 RF in single quantum dots

Ref. [19] was among the first to report resonance fluorescence under continuous wave (cw) excitation of a QD. The self-assembled QDs were grown between two distributed Bragg reflectors, which not only enhanced photon emission, but also guided the excitation beam in a direction orthogonal to that in which detection was carried out. The measured linewidth was 2.8 μeV at weak driving fields, with that value increasing with excitation power. Rabi oscillations in the first-order correlation function were observed at stronger driving fields. The second-order correlation function measurements revealed antibunching, providing evidence of the quantum nature of the emission. The Rabi frequency was found to be linearly dependent on the square root of excitation power. The exciton lifetime T_1 and the reverse of the dephasing rate T_2 were measured to be 290 ps and 380 ps.

RF from QDs embedded in an optical waveguide under picosecond laser excitation have also been observed [20], with Rabi oscillations of the emission intensity as a function of driving field appearing at increased pulse intensities. Oscillations in the second-order correlation function at higher laser Rabi frequencies were reported in Ref. [4].

Experimental observation of the Mollow triplet representing Rabi oscillations in the spectral domain was reported in Ref. [21] for measurements at high driving powers ($\Omega_R < \Gamma$). The position of sidebands was found to be dependent on the laser detuning from resonance.

RF had also been used to probe the dynamics of electron spins [3]. Ref. [22] measured electron spin lifetimes of 20 ms using the following procedure. First, a magnetic field was applied to a QD in order to split the ground state energy levels. Next, the spins were shelved into one of the states (spin-down) by driving the higher energy transition. Last, after a specific period of time the same driving laser was used to check the system for the presence of spin-up electrons. If a spin had decayed during the waiting time, RF counts were registered. The spin flips were accomplished through electron cotunneling into the QD from the n-doped layer [23].

The indistinguishability of photons under resonant excitation has been investigated in Refs [12, 13, 24–27]. The properties of indistinguishable photons are identical, and the canonical test of photon indistinguishability is the Hong-Ou-Mandel (HOM) two-photon interference measurement carried out with a Mach-Zehnder interferometer and introduced in [28]. Ref. [12] reports on two-photon interference of indistinguishable single photons under resonant pulsed excitation with HOM visibilities near unity (97.2%). The in-plane component of the net nuclear spin has been found to lead to Raman scattering for negatively charged QDs, reducing the two-photon interference visibility [29]. It was reported that an applied magnetic field screens the electrons from the effect of the nuclear field fluctuations, reducing Raman scattering and restoring the two-photon interference visibility [29].

1.4 Telecom wavelength QDs

QDs emitting photons in the telecommunication O-band ($\lambda = 1310$ nm) or C-band ($\lambda = 1550$ nm) are attracting a lot of attention in the scientific community in recent years due to their suitability to facilitate efficient quantum communication. Attenuation in optical fibers is smaller for light at telecom wavelengths, which makes the study of quantum dots emitting at these wavelengths important from a standpoint of practical technological implementation. Despite this, up to now relatively little research has been devoted to these QDs compared to those emitting at shorter wavelengths ($\lambda < 1$ μm). There are two main reasons for this. First of all, growth

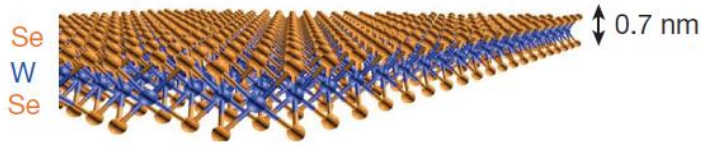

Figure 1.4: Schematic showing the structure of a WSe_2 monolayer. Figure from Ref. [39].

techniques for these QDs are not as well-developed. In this project the QDs were grown in a $In_{0.18}Ga_{0.82}As$ quantum well, resulting in larger QD dimensions in the vertical direction due to strain relaxation. An increase in size corresponds to a reduction in the energy distance between the excited exciton state and the ground state, red-shifting the emission wavelength of such dot-in-a-well or DWELL structures [30] to the telecom O-band at 4 K.

The second challenge of working at telecom wavelengths is the difficulty of single photon detection at $\lambda \approx 1300$ nm. This efficiency is somewhat lower than that of the Si-based detectors used at $\lambda < 1$ μm (see Section 2.2.12).

Under non-resonant excitation telecom wavelength QDs were found to be sources of single indistinguishable [31] and entangled photon pairs [32].

1.5 Two-dimensional semiconductors

Two-dimensional (2D) materials came to the attention of the scientific community in 2004 with the isolation of graphene [33], for which A. Geim and K. Novoselov were awarded the 2010 Nobel prize in physics. In the last few years, monolayers and bilayers of transition metal dichalcogenide (TMD) crystals have emerged as interesting optoelectronic materials due to their unique electronic and optical properties. The most commonly studied TMD semiconducting monolayers include MoS_2, $MoSe_2$, WS_2, and WSe_2, with the latter being of particular relevance for this work.

Potential application of TMD monolayers include field effects transistors [34], light emitting diodes [35, 36], solar cells [37], photodetectors [38], and nanoscale laser systems [39].

1.5.1 TMD structure and monolayer sample preparation

In a TMD monolayer, each metal atom forms an ionic-covalent bond with two chalcogen atoms. The metal atoms organize hexagonally and are surrounded on both sides by two layers of chalcogen atoms in a trigonal prismic coordination. A single monolayer of WSe_2 is about 0.7 nm thick and contains just one layer of metal atoms sandwiched between two layers of chalcogen atoms (see Fig. 1.4), with the structure held together by weak van der Waals forces. Such a monolayer structure is stable and mechanically durable, as well as robust over long timescales. Due to their 2D structure, TMD monolayers have reduced dielectric screening by the host material in two dimensions, which leads to very strong electron-hole Coulomb interactions and large exciton binding energies [40, 41].

TMD monolayer samples are relatively easy to prepare from a bulk crystal using a modification of the mechanical exfoliation method ('Scotch tape method'). An all-dry method was demonstrated in [42] that showed a 100% success rate. By avoiding wet chemistry, the monolayer surface is kept free of contaminants, and freely suspended structures can easily be fabricated. For instance, the authors report a successful transfer of a WSe_2 flake over a substrate patterned with holes.

1.5.2 TMD 2D exciton photoluminescence

A multilayer WSe_2 structure has a indirect band gap, leading to a low intensity PL signal, which experiences a red-shift and gradually disappears as the number of layers is increased [43, 44]. For a WSe_2 and $MoSe_2$ monolayer the band gap is direct, and the PL signal in the visible spectral range is very bright as a consequence [43].

Microphotoluminescence (μ-PL) from WSe_2 monolayers is characterized by the presence of a low intensity 2D free exciton peak at around $E_{2D-X} \approx 1.74$ eV with a linewidth of about 10 meV [45] and a primary lifetime of less than 4 ps [46]. The lower intensity peak from a delocalized trion state is visible at slightly lower energies ($E_{2D-T} \approx 1.71$ eV) [45], with linewidths of 15 meV and exciton lifetimes of 18 ps [46]. These delocalized excitonic states are always present in WSe_2 monolayers due to unintentional doping of the crystal. PL intensity from these excitons is linearly dependent on excitation power, and generally requires high excitation powers to be clearly seen [46]. The linewidth of emission of delocalized excitons is not broadened with power [47].

Free exciton binding energies in WSe_2 monolayers are generally on the order of a few hundred meV, while delocalized trions have binding energies usually in the 20-30 meV range [48]. Large binding energies may indicate the presence of excitons containing several particles. The binding energy of a biexciton is defined as the difference between the energy of two excitons and a biexciton. In Ref. [48] the authors investigate a PL peak visible at high excitation power with an intensity dependence on excitation power that is superlinear to the free exciton intensity dependence. They identify the emission as originating from a delocalized biexciton and measure its binding energy to be in the 50-70 meV range, an order of magnitude higher that in 2D quantum wells in III-V semiconductors. In Ref. [49] a computational technique using the effective mass model is applied to the system that correctly predicts the binding energies of the free exciton and trion measured in Ref. [48], but fails to accurately estimate the biexciton binding energy. According to the model, the binding energy of the biexciton should be less than that of the trion. The authors suggest that the state observed in Ref. [48] is actually an excited state of the delocalized biexciton.

The lowest energy transition in a WSe_2 monolayer is an optically dark state, which quenches emission from the 2D free exciton at lower temperatures, while the opposite is true for MoS_2 and $MoSe_2$ monolayers, indicating a bright lowest energy transition (2D free exciton) [50, 51].

An exciton charge-tunable device based on a WSe_2 monolayer that enables second-harmonic generation was demonstrated in [52]. This non-linear effect is a result of photon scatter on the exciton or trion. The energy of the second harmonic is dependent on the excitation energy. The doping level is controlled by the bias applied to the device: at high doping levels the density of states is dominated by the trion, while low doping levels correspond to the neutral exciton. Thus, charge-tuning the device changes its efficiency.

1.5.3 Band structure and valley pseudo spin

The valence band maximum and the conduction band minimum of a WSe_2 monolayer are located at the K point in the first Brillouin zone. Strong spin-orbit coupling results in lifting the degeneracy of the valleys, which splits the valence band by several hundred meV and the conduction band by a few microelectronvolts. As

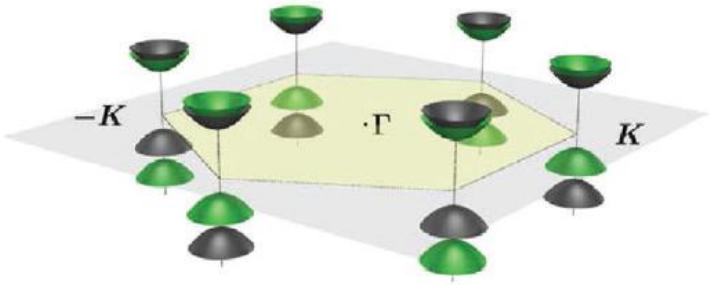

Figure 1.5: Schematic of the hexagonal Brillouin zone of a WSe_2 monolayer with non-equivalent K valleys clearly visible. Black (green) color of the conduction and valence bands corresponds to spin-up (-down) excitonic states. Figure from Ref. [68].

a consequence, there are two non-equivalent K valleys (K_+ and K_-) in the first Brillouin zone in WSe_2 monolayers (see Fig. 1.5) [46]. The non-equivalency of the valleys leads to an additional degree of freedom for carriers and determines the valley-dependent optical selection rules for excited electron-hole pairs [45, 46].

Optical pumping of carriers into a specific valley in TMD monolayers was demonstrated in Refs [45, 53–55] (see Fig. 1.6). Using polarization-resolved PL measurements, the authors have been able to show that excitation with circularly polarized light results in the excitation of an electron-hole pair in a specific valley (K_+ or K_-), and emission leads to the emitted photons having predominantly the same polarization as the excitation light. The conservation of polarization was made possible by minimal intervalley scattering and long exciton valley pseudospin dephasing times [45]. The former is a result of large momentum separation between valleys due to strong spin-orbit splitting [46]. The valley coherence time was demonstrated to be longer than the exciton lifetime [45].

1.5.4 TMD single photon emitters

Monolayer sample preparation by mechanical exfoliation and even chemical vapor deposition leads to the formation of atomic defects, which are believed to be efficient carrier trapping centers [56–60]. Alternate sources of localized excitons are theorized to be impurities introduced during mechanical exfoliation [61]. In both cases, localized states form within the WSe_2 bandgap, explaining the emission energy of localized state being below that of delocalized excitons [61]. Either of the

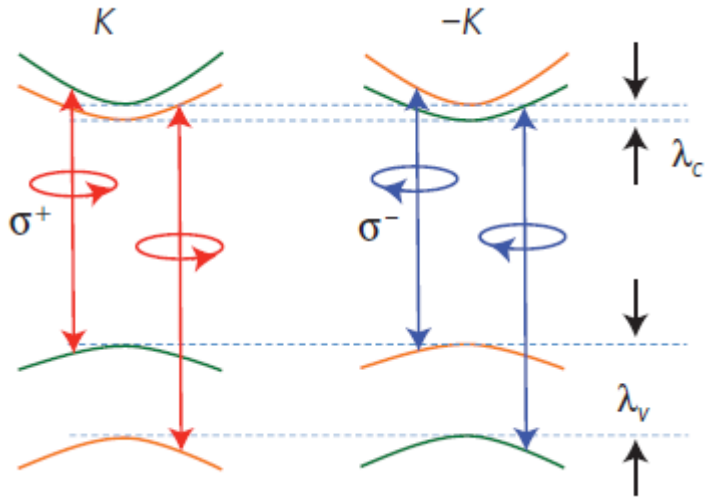

Figure 1.6: The valley optical selection rules that determine the polarization of absorbed and emitted photons under optical pumping of a WSe_2 monolayer. λ_c and λ_v are the spin splittings in conduction and valence bands, respectively. Figure from Ref. [65].

above sources of localized states suggests the durability of confined excitons, which is reported to be the case in experiments [57, 58].

One of the potential benefits of localized emitters in 2D structures such as TMD monolayers and bilayers is a high extraction efficiency of photons compared to traditional photon sources, where emitters are embedded in bulk solid state materials with a high index of refraction. Furthermore, the local environment surrounding an emitter embedded in a host material leads to dephasing as a result of interaction with phonons and spectral fluctuations due to charge noise [62]. An additional benefit of localized emission from monolayers and bilayer TMDs is that due to the emitters being located at the surface of the 2D material, the emission is strongly affected by external perturbations, making fine control using externally applied fields possible. For example, the band gap of a WSe_2 bilayer can be widely tuned with a stain field [43].

The sharp PL lines from excitons trapped on defects in the WSe_2 monolayer crystal lattice are of particular interest. Such spatially localized excitons emit photons at a lower energy ($E_{0D-X} < 1.72$ eV) [45] and can demonstrate a significantly brighter PL signal [56] than the delocalized excitons. PL intensity increases with a decrease of temperature, indicating that photon emission occurs from the lowest

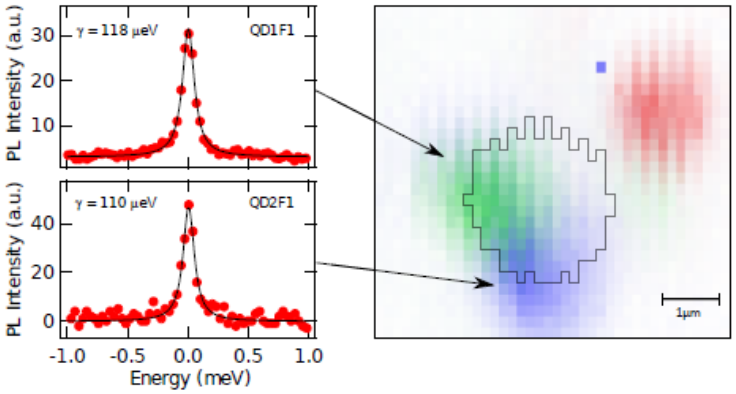

Figure 1.7: Sharp PL peak emission (left panels) from defect-bound excitons in a WSe_2 monolayer is demonstrated to be spatially localized on a position-dependent PL map (right panel). Figure from Ref. [59].

energy excited state [56]. Similar to atom-like two-level systems such as QDs, emission from the defect-bound state demonstrates saturation behavior with power [56]. In Ref. [59] the authors report that PL intensity reaches saturation and does not degrade at HeNe laser excitation powers of hundreds of microwatts.

Many PL lines from the defect-bound states are cross-linearly polarized doublets signifying that the emission likely originates from a neutral exciton state [56]. Emission line degeneracy is lifted by electron-hole exchange interaction [63]. The FSS is generally about 700 μeV, indicating that the electron-hole exchange interaction is quite strong [56–59].

The linewidth of the PL signal from these emitters is reported to be about 100 μeV, about two orders of magnitude smaller than that of the 2D free exciton [56–59], and is shown to increase with temperature due to scattering on acoustic phonons [64]. The narrow linewidth indicates that the emission is localized, which is confirmed with position-dependent PL maps (see Fig. 1.7) [56, 59, 60]. Excitons localized on defects were found to be quite long-lived with lifetimes of a couple nanoseconds [56–60].

Fluctuations in electrical charge of the emitter surroundings leads to spectral wandering [56,58,59], which can be seen on PL spectra as random shifts in emission energy, sometimes referred to as jitter. A time-averaged linewidth becomes broadened as a consequence [57, 59]. Over a millisecond timescale, the time-jitter is on the order of a linewidth, but larger jumps occur at timescales of several seconds [57]. Jitter is found to increase in intensity at higher excitation powers [57].

The light emitted from the defect-bound states is antibunched ($g^{(2)}(0) < 0.5$), confirming its predominantly single-photon nature [56, 57, 59, 60, 64]. In Ref. [56] second-order correlation functions of $g^{(2)}(0) = 0.14 \pm 0.04$ under continuous wave excitation and $g^{(2)}(0) = 0.21 \pm 0.06$ under pulsed excitation were reported.

In a magnetic field applied in the Faraday geometry PL lines split into two due to the lifting of the degeneracy of the K_+ and K_- valleys in the Brillouin zone [56–60, 65]. The Zeeman effect is particularly strong with g-factors reaching about 10 [56–60], several times larger than the g-factors of delocalized excitons in WSe_2 monolayers [66]. Upon applying a magnetic field in the Voigt configuration, no Zeeman splitting of emission lines has been reported [58, 59], likely due to the reduced dimensionality of the monolayer.

Strain gradients caused by a patterned substrate or wrinkles in the 2D sample can be used to spatially localize quantum emitters in WSe_2 monolayers and bilayers [60] and $MoSe_2$ monolayers [67], as shown by sharp emitter PL linewidths , which replace ensemble emitter PL seen in unstrained high-density samples. Redshifts of the transition energy of up to 170 meV in WSe_2 monolayers [60] (10 meV in $MoSe_2$ monolayers [67]) as a consequence of localized strain variation were reported.

1.6 Discussion

From a fundamental angle, the bigger size of the telecom wavelength DWELLs compared to the more commonly studied QDs emitting at $\lambda \approx 950$ nm offers an opportunity to study the effect of QD structure on single and multi-particle physics. To examine the morphology of the telecom wavelength DWELLs the Coulomb blockade model is applied and their response to magnetic and electric fields is reported in this thesis.

Despite many recent developments in the study of 2D excitons in TMD monolayers, the study of isolated quantum emitters in these monolayers is incomplete. In this project an attempt was made to characterize the quantum nature and polarization of highly isolated localized emitters in a WSe_2 monolayer.

RF provides access to both coherent and incoherent portions of the emitted photons. It makes it possible to examine the dynamics of an emitter, such as electron and nuclear spins. Photons generated resonantly are generally more coherent than those excited non-resonantly, which improves their indistinguishability. Finally, RF

photons make it possible to develop a spin-photon interface necessary for quantum communication. The main challenge in observing RF is isolating the signal from the emitter from the scattered resonant laser light. For experiments described in this project suppression of laser light was achieved using a cross-polarization technique, discussed in more detail in Chapter 2. Here RF of self-assembled telecom wavelength QDs and excitons localized at lattice defects in WSe_2 monolayers is reported for the first time.

1.7 References

[1] Marian O. Scully and M. Suhail Zubairy, *Quantum optics*, Cambridge University Press, (1997).

[2] Rodney Loudon, *The quantum theory of light*, Oxford University Press, (2000).

[3] A. N. Vamivakas, C. Matthiesen, Y Zhao, C.-Y. Lu, and M. Atatüre, Resonance fluorescence from a single quantum dot, In: Alexander Tartakovskii (ed.), *Quantum dots: optics, electron transport and future applications*, 86-102, Cambridge University Press, (2010).

[4] E. B. Flagg, A. Muller, J. W. Robertson, S. Founta, D. G. Deppe, M. Xiao, W. Ma, G. J. Salamo, and C. K. Shih, Resonantly driven coherent oscillations in a solid-state quantum emitter, *Nature Physics*, **5**, 203 (2009).

[5] A. Zrenner, A close look on single quantum dots, *Journal of Chemical Physics*, **112**, 7790 (2000).

[6] A. N. Vamivakas and M. Atatüre, Photons and (artificial) atoms: an overview of optical spectroscopy techniques on quantum dots, *Contemporary Physics*, **51**, 17 (2010).

[7] C. Schneider, S. Höfling, and A. Forchel, Growth of III-V semiconductor quantum dots, In: Alexander Tartakovskii (ed.), *Quantum dots: optics, electron transport and future applications*, 3-20, Cambridge University Press, (2010).

[8] R. J. Warburton, Self-assembled semiconductor quantum dots, *Contemporary Physics*, **43**, 351 (2002).

[9] Fei Long, S. P. A. Gill, and A. C. F. Cocks, Effect of surface-energy anisotropy on the kinetics of quantum dot formation, *Physical Review B*, **64**, 121307(R) (2001).

[10] K. Konthasinghe, J. Walker, M. Peiris, C. K. Shih, Y. Yu, M. F. Li, J. F. He, L. J. Wang, H. Q. Ni, Z. C. Niu, and A. Muller, Coherent versus incoherent light scattering from a quantum dot, *Physical Review B*, **85**, 235315 (2012)).

[11] Andreas V. Kuhlmann, Julien Houel, Arne Ludwig, Lukas Greuter, Dirk Reuter, Andreas D. Wieck, Martino Poggio, and Richard J. Warburton,

Charge noise and spin noise in a semiconductor quantum device, *Nature Physics*, **9**, 570 (2013).

[12] Yu-Ming He, Yu He, Yu-Jia Wei, Dian Wu, Mete Atatüre, Christian Schneider, Sven Höfling, Martin Kamp, Chao-Yang Lu, and Jian-Wei Pan, On-demand semiconductor single-photon source with near-unity indistinguishability, *Nature Nanotechnology*, **8**, 213 (2013).

[13] Sebastian Unsleber, Yu-Ming He, Sebastian Maier, Stefan Gerhardt, Chao-Yang Lu, Jian-Wei Pan, Martin Kamp, Christian Schneider, and Sven Höfling, Highly indistinguishable on-demand resonance fluorescence photons from a deterministic quantum dot micropillar device with 75% extraction efficiency, *ArXiv e-prints*, 1512.07453 (2015).

[14] A. N. Vamivakas, C.-Y. Lu, C. Matthiesen, Y. Zhao, S. Fält, A. Badolato, and M. Atatüre, Observation of spin-dependent quantum jumps via quantum dot resonance fluorescence, *Nature*, **467**, 297 (2010).

[15] M. Müller, S. Bounouar, K. D. Jöns, M. Glässl, and P. Michler, On-demand generation of indistinguishable polarization-entangled photon pairs, *Nature Photonics*, **8**, 224 (2014).

[16] E. Knill, R. Laflamme, and G. J. Milburn, A scheme for efficient quantum computation with linear optics, *Nature*, **409**, 46 (2000).

[17] F. Schuda, C. R. Stroud Jr., and M. Hercher, Observation of the resonant Stark effect at optical frequencies, *Journal of Physics B*, **7**, L198 (1974).

[18] F. Y. Wu, R. E. Grove, and S. Ezekiel, Investigation of the spectrum of resonance fluorescence induced by a monochromatic field, *Physical Review Letters*, **35**, 1426 (1975).

[19] A. Muller, E. B. Flagg, P. Bianucci, X. Y. Wang, D. G. Deppe, W. Ma, J. Zhang, G. J. Salamo, M. Xiao, and C. K. Shih, Resonance fluorescence from a coherently driven semiconductor quantum dot in a cavity, *Physical Review Letters*, **99**, 187402 (2007).

[20] R. Melet, V. Voliotis, A. Enderlin, D. Roditchev, X. L. Wang, T. Guillet, and R. Grousson, Resonant excitonic emission of a single quantum dot in the Rabi regime, *Physical Review B*, **78**, 073301 (2008).

[21] A. Nick Vamivakas, Yong Zhao, Chao-Yang Lu, and Mete Atatüre, Spin-resolved quantum-dot resonance fluorescence, *Nature Physics*, **5**, 198 (2009).

[22] C.-Y. Lu, Y. Zhao, A. N. Vamivakas, C. Matthiesen, S. Fält, A. Badolato, and M. Atatüre, Direct measurement of spin dynamics in InAs/GaAs quantum dots using time-resolved resonance fluorescence, *Physical Review B*, **81**, 035332 (2010).

[23] Jan Dreiser, Mete Atatüre, Christophe Galland, Tina Müller, Antonio Badolato, and Atac Imamoğlu, Optical investigations of quantum dot spin dynamics as a function of external electric and magnetic fields, *Physical Review B*, **77**, 075317 (2008).

[24] Léonard Monniello, Antoine Reigue, Richard Hostein, Aristide Lemaitre, Anthony Martinez, Roger Grousson, and Valia Voliotis, Indistinguishable single photons generated by a quantum dot under resonant excitation observable without postselection, *Physical Review B*, **90**, 041303(R) (2014).

[25] Clemens Matthiesen, Martin Geller, Carsten H. H. Schulte, Claire Le Gall, Jack Hansom, Zhengyong Li, Maxime Hugues, Edmund Clarke, and Mete Atatüre, Phase-locked indistinguishable photons with synthesized waveforms from a solid-state source, *Nature Communications*, **4**, 1600 (2013).

[26] Charles Santori, David Fattal, Jelena Vuckovic, Glenn S Solomon, and Yoshihisa Yamamoto, Single-photon generation with InAs quantum dots, *New Journal of Physics*, **6**, 89 (2004).

[27] S. Ates, S. M. Ulrich, S. Reitzenstein, A. Löffler, A. Forchel, and P. Michler, Post-selected indistinguishable photons from the resonance fluorescence of a single quantum dot in a microcavity, *Physical Review Letters*, **103**, 167402 (2009).

[28] C. K. Hong, Z. Y. Ou, and L. Mandel, Measurement of subpicosecond time intervals between two photons by interference, *Physical Review Letters*, **59**, 2044 (1987).

[29] R. N. E. Malein, T. S. Santana, J. M. Zajac, A. C. Dada, E. M. Gauger, P. M. Petroff, J. Y. Lim, J. D. Song, and B. D. Gerardot, Screening nuclear field fluctuations in quantum dots for indistinguishable photon generation, *ArXiv e-prints*, 1509.01057 (2015).

[30] K. Srinivasan, O. Painter, A. Stintz, and S. Krishna, Single quantum dot spectroscopy using a fiber taper waveguide near-field optic, *Applied Physics Letters*, **91**, 091102 (2007).

[31] Je-Hyung Kim, Tao Cai, Christopher J. K. Richardson, Richard P. Leavitt, and Edo Waks, A bright on-demand source of indistinguishable single photons at telecom wavelengths, *ArXiv e-prints*, 1511.05617 (2015).

[32] M. B. Ward, M. C. Dean, R. M. Stevenson, A. J. Bennett, D. J. P. Ellis, K. Cooper, I. Farrer, C. A. Nicoll, D. A. Ritchie, and A. J. Shields, Coherent dynamics of a telecom-wavelength entangled photon source, *Nature Communications*, **5**, 3316 (2014).

[33] K. S. Novoselov, A. K. Geim, S. V. Morozov, D. Jiang, Y. Zhang, S. V. Dubonos, I. V. Grigorieva, and A. A. Firsov, Electric field effect in atomically thin carbon films, *Science*, **306**, 666 (2004).

[34] Branimir Radisavljevic and Andras Kis, Mobility engineering and a metalnsulator transition in monolayer MoS_2, *Nature Materials*, **12**, 815 (2013).

[35] Jason S. Ross, Philip Klement, Aaron M. Jones, Nirmal J. Ghimire, Jiaqiang Yan, D. G. Mandrus, Takashi Taniguchi, Kenji Watanabe, Kenji Kitamura, Wang Yao, David H. Cobden, and Xiaodong Xu, Electrically tunable excitonic light-emitting diodes based on monolayer WSe_2 $p-n$ junctions, *Nature Nanotechnology*, **9**, 268 (2014).

[36] Britton W. H. Baugher, Hugh O. H. Churchill, Yafang Yang, and Pablo Jarillo-Herrero, Optoelectronic devices based on electrically tunable $p-n$ diodes in a monolayer dichalcogenide, *Nature Nanotechnology*, **9**, 262 (2014).

[37] Andreas Pospischil, Marco M. Furchi, and Thomas Mueller, Solar-energy conversion and light emission in an atomic monolayer $p-n$ diode, *Nature Nanotechnology*, **9**, 257 (2014).

[38] Oriol Lopez-Sanchez, Dominik Lembke, Metin Kayci, Aleksandra Radenovic, and Andras Kis, Ultrasensitive photodetectors based on monolayer MoS_2, *Nature Nanotechnology*, **8**, 497 (2013).

[39] Sanfeng Wu, Sonia Buckley, John R. Schaibley, Liefeng Feng, Jiaqiang Yan, David G. Mandrus, Fariba Hatami, Wang Yao, Jelena Vu**c**ković, Arka Majumdar, and Xiaodong Xu, Monolayer semiconductor nanocavity lasers with ultralow thresholds, *Nature*, **520**, 69 (2015).

[40] Keliang He, Nardeep Kumar, Liang Zhao, Zefang Wang, Kin Fai Mak, Hui Zhao, and Jie Shan, Tightly bound excitons in monolayer WSe_2, *Physical Review B*, **113**, 026803 (2014).

[41] Kin Fai Mak, Keliang He, Changgu Lee, Gwan Hyoung Lee, James Hone, Tony F. Heinz, and Jie Shan, Tightly bound trions in monolayer MoS_2, *Nature Materials*, **12**, 207 (2013).

[42] Andres Castellanos-Gomez, Michele Buscema, Rianda Molenaar, Vibhor Singh, Laurens Janssen, Herre S J van der Zant, and Gary A Steele, Deterministic transfer of two-dimensional materials by all-dry viscoelastic stamping, *2D Materials*, **1**, 011002 (2014).

[43] Sujay B. Desai, Gyungseon Seol, Jeong Seuk Kang, Hui Fang, Corsin Battaglia, Rehan Kapadia, Joel W. Ager, Jing Guo, and Ali Javey, Strain-induced indirect to direct bandgap transition in multilayer WSe_2, *Nano Letters*, **14**, 4592 (2014).

[44] Weijie Zhao, Zohreh Ghorannevis, Leiqiang Chu, Minglin Toh, Christian Kloc, Ping-Heng Tan, and Goki Eda, Evolution of electronic structure in atomically thin sheets of WS_2 and WSe_2, *ACS Nano*, **7**, 791 (2013).

[45] Aaron M. Jones, Hongyi Yu, Nirmal J. Ghimire, Sanfeng Wu, Grant Aivazian, Jason S. Ross, Bo Zhao, Jiaqiang Yan, David G. Mandrus, Di Xiao, Wang Yao, and Xiaodong Xu, Optical generation of excitonic valley coherence in monolayer WSe_2, *Nature Nanotechnology*, **8**, 634 (2013).

[46] G. Wang, L. Bouet, D. Lagarde, M. Vidal, A. Balocchi, T. Amand, X. Marie, and B. Urbaszek, Valley dynamics probed through charged and neutral exciton emission in monolayer WSe_2, *Physical Review B*, **90**, 075413 (2014).

[47] Z. Y. Zhu, Y. C. Cheng, and U. Schwingenschlögl, Giant spin-orbit-induced spin splitting in two-dimensional transition-metal dichalcogenide semiconductors, *Physical Review B*, **84**, 153402 (2011).

[48] Yumeng You, Xiao-Xiao Zhang, Timothy C. Berkelbach, Mark S. Hybertsen, David R. Reichman, and Tony F. Heinz, Observation of biexcitons in monolayer WSe_2, *Nature Physics*, **11**, 477 (2015).

[49] D. K. Zhang, D. W. Kidd, and K. Varga, The biexciton puzzle, *ArXiv e-prints*, 1507.07858 (2015).

[50] Xiao-Xiao Zhang, Yumeng You, Shu Yang Frank Zhao, and Tony F. Heinz, Experimental evidence for dark excitons in monolayer WSe_2, *Physical Review Letters*, **115,**, 257403 (2015).

[51] Gang Wang, Cedric Robert, Aslihan Suslu, Bin Chen, Sijie Yang, Sarah Alamdari, Iann C. Gerber, Thierry Amand, Xavier Marie, Sefaattin Tongay, and Bernhard Urbaszek, Spin-orbit engineering in transition metal dichalcogenide alloy monolayers, *Nature Communications*, **6**, 10110 (2015).

[52] Kyle L. Seyler, John R. Schaibley, Pu Gong, Pasqual Rivera, Aaron M. Jones, Sanfeng Wu, Jiaqiang Yan, David G. Mandrus, Wang Yao, and Xiaodong Xu, Electrical control of second-harmonic generation in a WSe_2 monolayer transistor, *Nature Nanotechnology*, **10**, 407 (2015).

[53] Hualing Zeng, Junfeng Dai, Wang Yao, Di Xiao, and Xiaodong Cui, Valley polarization in MoS_2 monolayers by optical pumping, *Nature Nanotechnology*, **7**, 490 (2012).

[54] Kin Fai Mak, Keliang He, Jie Shan, and Tony F. Heinz, Control of valley polarization in monolayer MoS_2 by optical helicity, *Nature Nanotechnology*, **7**, 494 (2012).

[55] Ting Cao, Gang Wang, Wenpeng Han, Huiqi Ye, Chuanrui Zhu, Junren Shi, Qian Niu, Pingheng Tan, Enge Wang, Baoli Liu, and Ji Feng, Valley-selective circular dichroism of monolayer molybdenum disulphide, *Nature Communications*, **3**, 887 (2012).

[56] Yu-Ming He, Genevieve Clark, John R. Schaibley, Yu He, Ming-Cheng Chen, Yu-Jia Wei, Xing Ding, Qiang Zhang, Wang Yao, Xiaodong Xu, Chao-Yang Lu, and Jian-Wei Pan, Single quantum emitters in monolayer semiconductors, *Nature Nanotechnology*, **10**, 497 (2015).

[57] M. Koperski, K. Nogajewski, A. Arora, V. Cherkez, P. Mallet, J.-Y. Veuillen, J. Marcus, P. Kossacki, and M. Potemski, Single photon emitters in exfoliated WSe2 structures, *Nature Nanotechnology*, **10**, 503 (2015).

[58] Chitraleema Chakraborty, Laura Kinnischtzke, Kenneth M. Goodfellow, Ryan Beams, and A. Nick Vamivakas, Voltage-controlled quantum light from an atomically thin semiconductor, *Nature Nanotechnology*, **10**, 507 (2015).

[59] Ajit Srivastava, Meinrad Sidler, Adrien V. Allain, Dominik S. Lembke, Andras Kis, and A. Imamoğlu, Optically active quantum dots in monolayer WSe_2, *Nature Nanotechnology*, **10**, 491 (2015).

[60] S. Kumar, A. Kaczmarczyk, and B. D. Gerardot, Strain-induced spatial and spectral isolation of quantum emitters in mono- and bilayer WSe_2, *Nano Letters*, **15**, 7567 (2015).

[61] Jiani Huang, Thang B. Hoang, and Maiken H. Mikkelsen, Probing the origin of excitonic states in monolayer WSe_2, *Scientific Reports*, **6**, 22414 (2016).

[62] Richard J. Warburton, Single spins in self-assembled quantum dots, *Nature Materials*, **12**, 483 (2013).

[63] D. Gammon, E. S. Snow, B. V. Shanabrook, D. S. Katzer, and D. Park, Fine structure splitting in the optical spectra of single GaAs quantum dots, *Physical Review Letters*, **76**, 3005 (1996).

[64] V. Perebeinos, Metal dichalcogenides: Two dimensions and one photon, *Nature Nanotechnology*, **10**, 485 (2015).

[65] Xiaodong Xu, Wang Yao, Di Xiao, and Tony F. Heinz, Spin and pseudospins in layered transition metal dichalcogenides, *Nature Physics*, **10**, 343 (2014).

[66] G. Aivazian, Zhirui Gong, Aaron M. Jones, Rui-Lin Chu, J. Yan, D. G. Mandrus, Chuanwei Zhang, David Cobden, Wang Yao, and X. Xu, Magnetic control of valley pseudospin in monolayer WSe_2, *Nature Physics*, **11**, 148 (2015).

[67] Artur Branny, Gang Wang, Santosh Kumar, Cedric Robert, Benjamin Lassagne, Xavier Marie, Brian D. Gerardot, and Bernhard Urbaszek, Discrete quantum dot like emitters in monolayer $MoSe_2$: Spatial mapping, Magneto-optics and Charge tuning, *ArXiv e-prints*, 1602.07947 (2016).

[68] Gui-Bin Liu, Di Xiao, Yugui Yao, Xiaodong Xude, and Wang Yao , Electronic structures and theoretical modelling of two-dimensional group-VIB transition metal dichalcogenides, *Chemical Society Reviews*, **44**, 2643 (2015).

Chapter 2

Samples and experimental set-up

In this thesis, the emission from two types of quantum structures under coherent and incoherent excitation was studied. This chapter discusses the characteristics and preparation procedures of the samples under study: telecommunication wavelength quantum dots (QDs) and WSe_2 monolayers. These samples act as sources of single photons emitting around $\sim$ 1300 nm and $\sim$ 760 nm, respectively. In the second half of this chapter, a confocal microscope set-up providing submicron resolution is described. The configurations of four microscope heads and their alignment procedure that allowed high-efficiency measurements under non-resonant and resonant excitation at $\sim$ 1300 nm and $\sim$ 760 nm will be discussed.

2.1 Sample structure

In this section, the photon sources used in this work are described. First, the main characteristics and preparation procedure of the telecommunications wavelength QD samples used for magneto-optical and time-resolved measurements (charge-tunable QD sample), as well as resonance fluorescence (RF) experiments (charge-tunable and *p-i-n* diode QD samples) are described. At the end of the section the WSe_2 monolayer sample is discussed.

2.1.1 Charge-tunable telecommunications wavelength QD samples

Measurements were performed on a series of single self-assembled InAs QDs grown in an $In_{0.18}Ga_{0.82}As$ quantum well (dot-in-a-well or DWELL structures). Such QDs

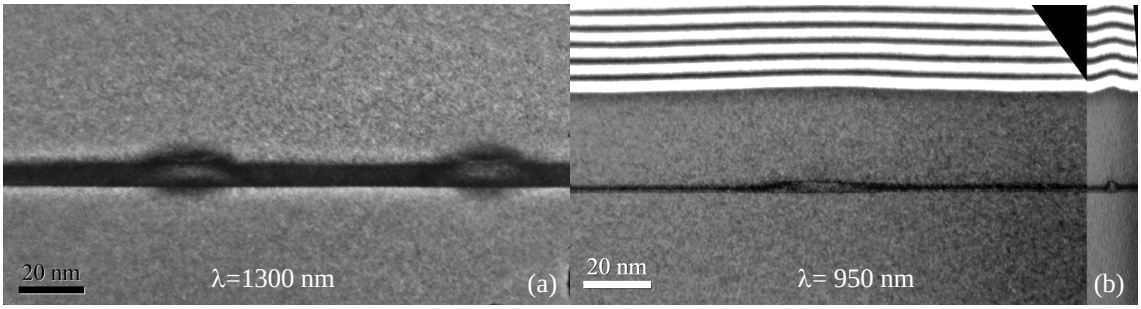

Figure 2.1: (a) TEM image of a telecom wavelength QD from a metal-insulator-semiconductor field-effect transistor (MISFET). These QDs appear taller than the QDs emitting at around $\lambda = 950$ nm from a sample with a similar structure that were previously studied in our lab (b), which should affect their confinement in the vertical direction (see Chapter 3). The images were taken by Dr Richard Beanland of the University of Warwick.

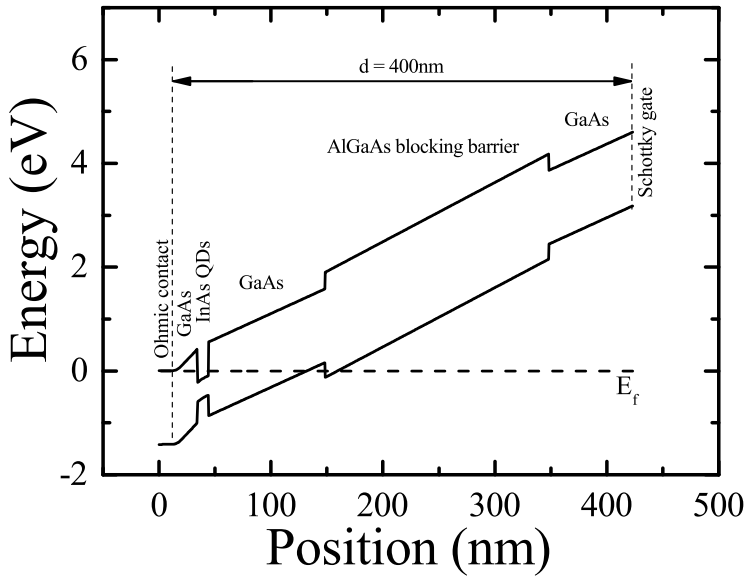

Figure 2.2: Band diagram of the charge tunable device VN2209A under study under an applied bias of -4V. The InAs telecom wavelength QD layer is grown in a quantum well. The highly doped back contact (n^+ GaAs layer) is grounded, and bias is applied to the NiCr top gate. The electric field between the top contact and the back gate is dependent on the difference in potential between the Schottky barrier height and the applied bias. E_f is the Fermi energy level. The tunneling barrier is the GaAs layer between the back contact and the QD layer. The lever arm coefficient is equal to $\lambda = d/t$, where d is the distance between the top and the back gates, and t is the thickness of the tunnel barrier.

can reach larger sizes vertically, which redshifts their emission wavelength relative to typical self-assembled QDs. Transmission electron microscopy (TEM) images show that these telecom wavelength QDs (see Fig. 2.1(a)) are about the same size laterally ($\sim$ 20 nm) as the QDs with an emission wavelength of 950 nm previously studied in our lab (see Fig. 2.1(b)), but are significantly taller ($\sim$ 10 nm). The QDs were grown by self-assembly by solid source molecular beam epitaxy (MBE) in the Stranski-Krastanov growth method. A gradient in the density of QD can be achieved through a stop of the substrate rotation during QD layer growth.

The wafer growth took place on a semi-insulating GaAs wafer with a two inch diameter (see Table 2.1, Table 2.2). A 200 nm GaAs buffer layer and a 2 nm$\times$2 nm 40 period AlAs/GaAs superlattice was used to smooth the surface following oxide deposition, followed by an 80 nm layer of GaAs. An n-type GaAs back gate with a doping level of 2×10^{18} cm^{-3} was grown next, followed by a GaAs tunnel barrier (14 nm for sample VN2209A and 28 nm for sample VN2476E). The InAs dots embedded in an $In_{0.18}Ga_{0.82}As$ quantum well followed. The quantum dots were grown with a rotation stop, though a QD density gradient was apparent only for wafer VN2476E. The capping layer for the dots was GaAs (4 nm thick for wafer VN2209A and 12 nm for wafer VN2476E), followed by a 100 nm layer of GaAs for sample VN2209A. The blocking barrier was a 3 nm$\times$2 nm AlAs/GaAs superlattice with 40 (VN2209A) or 22 (VN2476E) periods, used to prevent leakage of charge carriers through the device and carrier ionization from the QDs, and capped by a GaAs layer to prevent surface oxidation. A band diagram of the structure is shown in Fig. 2.2. The wafers were grown by Dr Edmund Clarke at the EPSRC National Center for III-V Technologies at the University of Sheffield.

It is important to note that in a charge-tunable device with the described structure, holes excited by a non-resonant laser can become trapped at the interface between the capping layer and the blocking barrier, which results in a built-up of positive charge, slightly countering the net electric field applied to the dots [1, 2], and possibly causing spectral fluctuations due to charge noise.

2.1.2 Wafer density mapping

As a preliminary step in the search for a bright QD, density mapping was carried out to characterize a total of five wafers with charge-tunable telecom QDs. Non-

Table 2.1: Layer composition of wafer VN2209A containing charge-tunable telecom wavelength InAs quantum dots in an $In_{0.18}Ga_{0.82}As$ quantum well.

Layer size and content	Notes
GaAs 75 nm	
AlAs/GaAs 3 nm/2 nm ×40	Blocking barrier
GaAs 100 nm	
GaAs 4 nm	Capping layer
$In_{0.18}Ga_{0.82}As$ 6 nm	Quantum well
InAs	QDs, grown without rotation
$In_{0.18}Ga_{0.82}As$ 1 nm	Quantum well
GaAs 14 nm	Tunnel barrier
n^+ GaAs 20 nm	Back gate (doping level 2×10^{18} cm^{-3})
GaAs 80 nm	
AlAs/GaAs 2 nm/2 nm ×40	Smoothing superlattice
GaAs 200 nm	
GaAs substrate 2”	

Table 2.2: Layer composition of wafer VN2476E containing charge-tunable telecom wavelength InAs quantum dots in an $In_{0.18}Ga_{0.82}As$ quantum well.

Layer size and content	Notes
GaAs 60 nm	
AlAs/GaAs 3 nm/2 nm ×22	Blocking barrier
GaAs 12 nm	Capping layer
$In_{0.18}Ga_{0.82}As$ 4 nm	Quantum well
InAs	QDs, grown without rotation
$In_{0.18}Ga_{0.82}As$ 1 nm	Quantum well
GaAs 28 nm	Tunnel barrier
n^+ GaAs 20 nm	Back gate (doping level 2×10^{18} cm^{-3})
GaAs 80 nm	
AlAs/GaAs 2 nm/2 nm ×40	Smoothing superlattice
GaAs 200 nm	
GaAs substrate 2”	

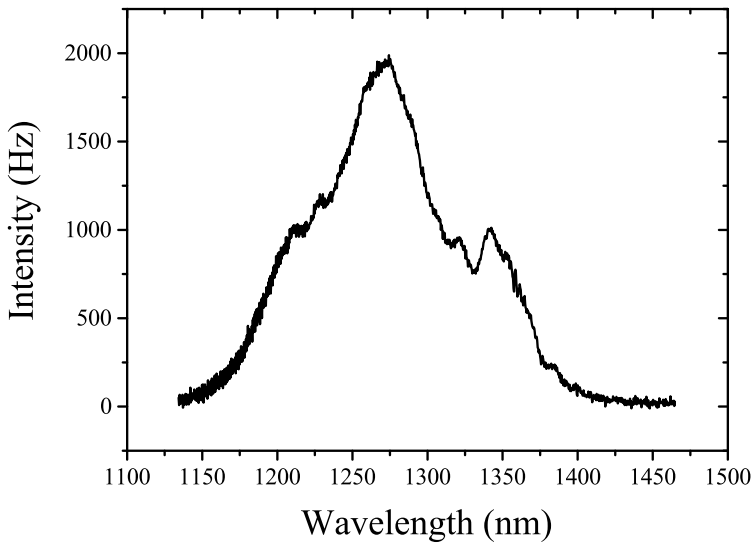

Figure 2.3: (a) An example PL spectra collected from wafer VN2476 at room temperature under cw above-band excitation with an acquisition time of 1 s.

resonant excitation was achieved by a continuous wave (cw) 830 nm diode laser. The measurements were taken at room temperature. For each wafer, the ensemble photoluminescence (PL) signal from sixty points located 5 mm apart from each other was recorded using the 1200 groove/mm grating on the spectrometer with 1 s acquisition time. An example PL spectra for one such point from wafer VN2476 is shown in Fig. 2.3. For this project, emission around 1300 nm at T=4 K was of particular interest. Fig. 2.4 shows spatial maps of the integrated intensity of the long wavelength tail of the PL spectra for each wafer.

Telecom wavelength sample VN2209A processed by Dr Luca Sapienza using the steps described in Section 2.1.3 originated from a wafer with no QD density gradient, which made the process of finding isolated quantum dots somewhat difficult due to high dot density throughout the wafer. According to Fig. 2.4 the new wafers should offer an opportunity to work with samples with a density gradient. Later, measurements at 4 K confirmed this.

2.1.3 Charge-tunable sample preparation

Once the wafer was mapped, the parts of it that were of interest were cleaved into 4×6 mm^2 samples and contacted. Deterministic control of the charge state of the QD was enabled by embedding the samples with the DWELL structures in a GaAs/AlAs device called a metal-insulator-semiconductor field-effect transistor (MISFET) by

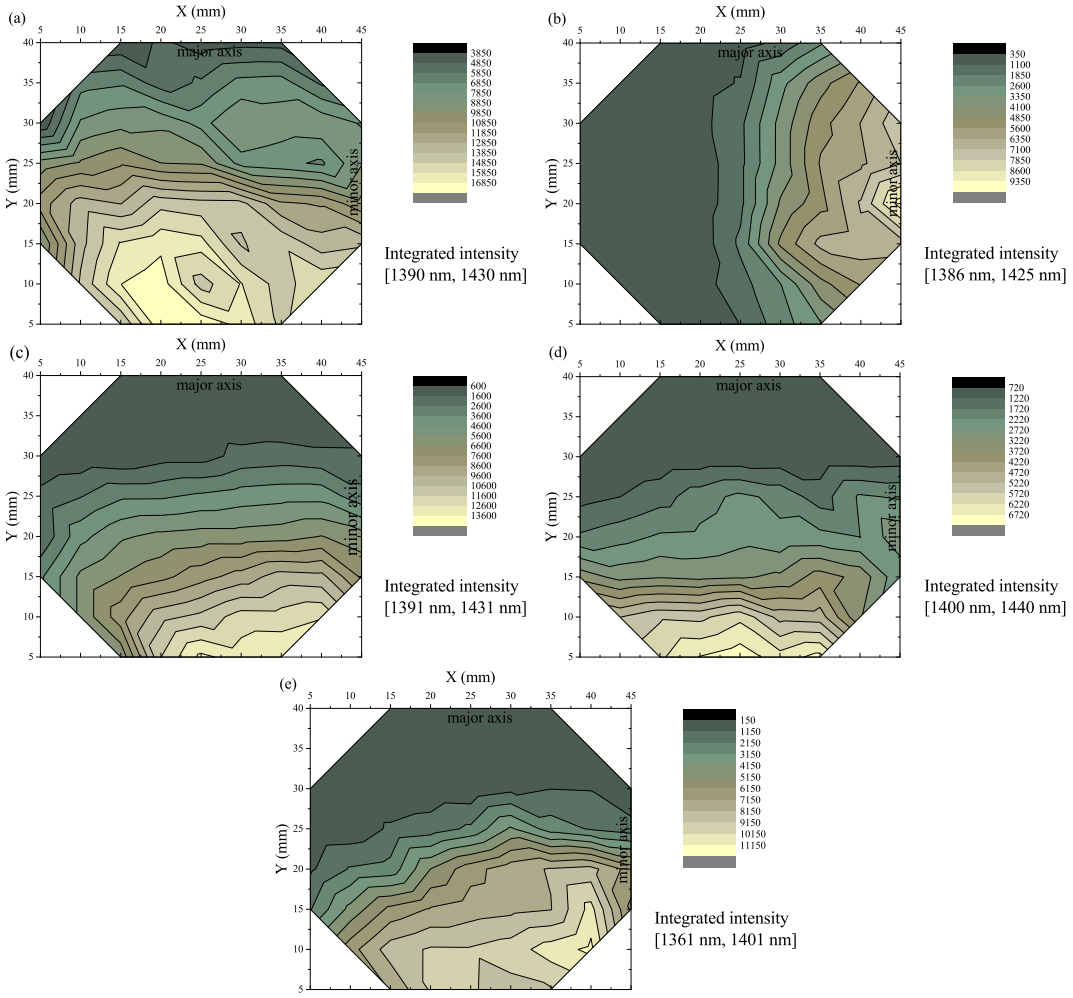

Figure 2.4: Diagrams showing the integrated intensity of the long wavelength tail (specific range of wavelengths for each wafer listed in square brackets) of the PL spectra for wafers VN2465 (a), VN2476 (b), VN2477 (c), VN2479 (d), and VN2481 (e) under cw above-band excitation at room temperature. The orientation of the wafer can be determined using the major and minor axes.

post-growth processing carried out in our lab. Before further processing, the samples were cleaned in a beaker with acetone, which was placed into an ultrasound bath for 5 minutes. The procedure was repeated with a beaker of isopropanol and, finally, ultrapure water. Following this, the samples were dried with nitrogen gas. In order to eliminate stray particles from the sample it was then placed in oxygen plasma for 1 minute (100 W).

In order to contact the doped layer within the structure, a piece of indium, with its topmost oxidized layer preliminarily cleaved off, was placed on top of the sample and then annealed at 350°C for 40 minutes to diffuse the indium to the n^+-doped layer. Alternatively, a back contact could made by evaporating via electron beam 25 nm of Ni and 100 nm of AuGe on a small area of the sample, followed by annealing for 5 minutes. In both cases, the resistance between two back contacts on the wafer that were completely diffused to the n-doped layer should be less than 1 kΩ.

Chromium was chosen as one of the metals used for the creating of the Schottky contact due to its transparency to radiation. Since chromium is also easily oxidized, nickel is added to the alloy in order to passivate the dangling bonds. Accordingly, a thin 5 nm thick NiCr top gate was evaporated on top of the sample. The Schottky barrier height for the NiCr/GaAs interface is $V_0 = 0.6$ eV. To prevent short circuiting, the top gate and the back contact should never be in direct contact. After processing, charging was implemented by varying the bias applied to the top gate (Schottky contact) of the sample. The voltage was applied by a Signal Recovery Model 7265 lock-in amplifier.

2.1.4 Coulomb blockade

In effect, the MISFET structure is a capacitor, making it possible to inject single electrons into the QD in a controlled manner utilizing the Coulomb blockade effect [3] by varying the bias applied to the structure. Under high reverse bias, QD energy levels are above the Fermi level, and no charging occurs. With decreasing reverse bias, the QD energy levels in the conduction band can be equal to or below the Fermi level, and electrons can tunnel from the back gate into the QD. Under non-resonant excitation, holes can populate the QD, and, when an electron tunnels into the dot, it is bound by Coulomb attraction to the hole, forming an exciton.

For pronounced Coulomb blockade, an additional electron can only tunnel into a

QD already containing an electron only if it overcomes the Coulomb repulsion with the first one [4], leading to the formation of a charged exciton [5] consisting of two electrons and a hole. The second electron has to have a spin opposite to the first electron in order to satisfy the Pauli exclusion principle. The neutral exciton and the charged exciton have different emission energies due to Coulombic forces, which leads to energy jumps on a PL map.

The bias V_g applied to the top gate of the MISFET is not the same as the potential V at the QD plane [6]:

$$\frac{V_g - V_0}{V} = \lambda. \tag{1}$$

Here λ is the lever arm coefficient, and $\lambda = d/t$, where d is the distance between the top and the back gates, and t is the thickness of the tunnel barrier.

2.1.5 Improving the collection efficiency

The collection efficiency of light from a sample with an objective lens with a numerical aperture NA can be estimated using the following formula [7]:

$$\eta = \frac{1}{2}\left\{1 - \left[1 - \left(\frac{NA\ n_2}{n_1}\right)^2\right]^{1/2}\right\}. \tag{2}$$

Here $n_{1,2}$ is the refractive index of the host material and the medium directly in contact with the host material, respectively. For QDs in a GaAs host material in contact with air, the value of Eq. 2 is less than $\eta = 1\%$ even with high numerical aperture optics [7].

There are a number of ways to enhance the extraction of emitter photons from the host material, and they can be broadly divided into two categories: cavities, which enhance emission into one desired mode, and solid/liquid immersion lenses, which enhance collection for a wide set of modes using refraction [8]. While the former offers higher collection efficiencies, the latter is cheaper and easier to implement.

To improve photon collection efficiency from the MISFET samples a solid immersion lens (SIL) was used. It offers an improved spatial resolution and collection efficiency of light as a result of an increased numerical aperture for far-field investigation of QD samples [9, 10]. The spatial resolution of the confocal optical microscope is defined by the numerical aperture $NA{=}n \sin\theta$, where n is the refractive index of the medium between the sample and the objective and θ is half of the angular

aperture of the objective, and the wavelength λ:

$$\Gamma = \frac{0.51\ \lambda}{n\ NA}. \tag{3}$$

Accordingly, QD samples with glass SILs with $n_{SIL} \approx 2$ offer higher spatial resolution than those without (n_{air}=1).

An important parameter when determining the collection efficiency of light is the critical angle. From Snell's law we have:

$$\frac{\sin\ \theta_1}{\sin\ \theta_2} = \frac{n_2}{n_1}. \tag{4}$$

Here index 1 refers to the sample medium and index 2 corresponds to the medium above the sample. When the sample is in contact with air, the following relation can be written for the angle of total internal reflection (sin θ_2=1):

$$\theta_1^{crit} = \sin^{-1}\left(\frac{n_2}{n_1}\right) = \sin^{-1}\left(\frac{1}{3.48}\right) = 16.7°. \tag{5}$$

Only light rays propagating at angles of incidence below 16.7° can be collected by the objective. The use of a SIL on the sample surface increases the NA, and through it, the critical angle:

$$\theta_1^{crit} = \sin^{-1}\left(\frac{n_2}{n_1}\right) = \sin^{-1}\left(\frac{2}{3.48}\right) = 35.1°. \tag{6}$$

The theory developed by Born and Wolf [11] states that there are two points in a sphere where light can be focused without aberrations. One such point is located at the center of the sphere, and this concept was realized in the design of a hemispherical SIL. In this configuration the light rays coming from QDs located directly below the center of the hemisphere are of interest, because they approach the SIL surface at a 90° angle, and consequently are not refracted by it [11]. With the use of an h-SIL the spatial resolution of the system increases by $1/n_{SIL}$, and its collection efficiency becomes about 4% [7].

The second point is located $z = R\ (n_{air}/n_{SIL})$ away from the center of the sphere, and this idea is used for the creation of super SILs [11]. A s-SIL offers a resolution gain by $1/n_{SIL}^2$, and a theoretically calculated collection efficiency of 20% [7].

Among the other methods to improve photon extraction from the host material are optical microcavities and waveguides [12].

One type of cavity is a 'bullseye' (see Fig. 2.5), consisting of a circular grating that is anisotropically etched. These structures, found to enhance the photon extraction efficiency further than a SIL, were described in Refs [13, 14]. The devices

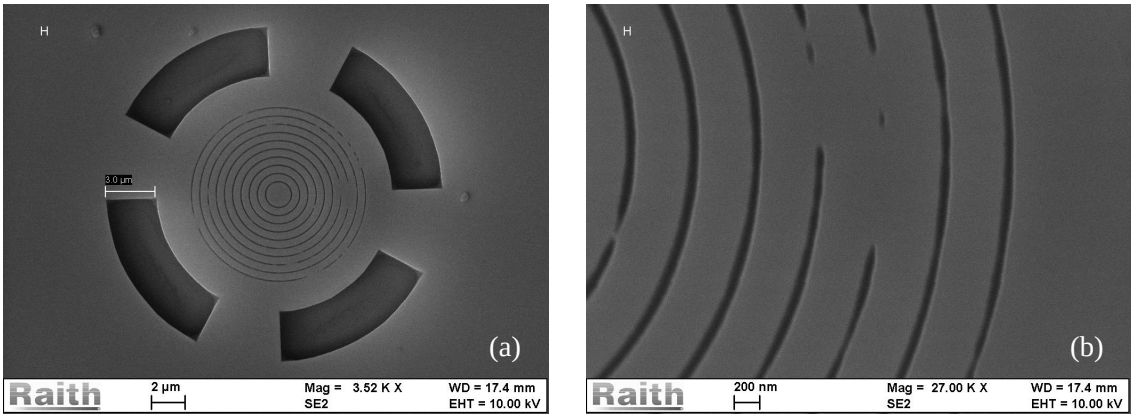

Figure 2.5: (a) Scanning electron microscope image of a circular grating structure designed to enhance photon extraction efficiency around $\lambda = 1300$ nm. (b) A zoomed-in image of the bullseye, showing that issues in the fabrication process resulted in incomplete etching of the trenches.

were composed of a GaAs membrane (diameter D ≈ 10 µm) with a series of partially etched circular trenches with a specific period and depth. The InAs QD layer was located in the center (diameter d ≈ 1 µm) of the membrane. The period of the grating was chosen to satisfy the second-order Bragg condition to facilitate efficient vertical light extraction. Most of the photons from the QD were internally reflected on the GaAs/air interface, and the circular grating created a photon interference pattern, guiding the photons out of the material towards the objective. The diameter of the central part of the membrane and the period of the trenches was chosen to enhance photon extraction for a spectral bandwidth of about 5 nm at a specific central wavelength. Collection improves mainly for photons from QDs located in the center of the membrane (see Fig. 2.6(a)). The depth of the trenches was chosen so that the extraction was primarily one-directional (upwards) (see Fig. 2.6(b)), with the extracted light forming a nearly Gaussian far-field pattern. Theoretical calculations predict 53% (80%) extraction for objectives with $NA = 0.42$ ($NA = 0.7$), Purcell radiative rate enhancements of $10 - 12$ and radiative lifetime reduction of a factor of 4 due to the effect of the cavity [14]. Collection efficiencies measured experimentally from such structures reached 10% for QDs emitting around $\lambda = 950$ nm [13, 14]. Analogous structures were designed and fabricated by Dr Luca Sapienza and Dr Kartik Srinivasan at National Institute of Standards and Technology for enhanced collection around 1300 nm (see Fig. 2.5(a)), but upon testing them experimentally it was discovered that collection was significantly lower than expected, most likely

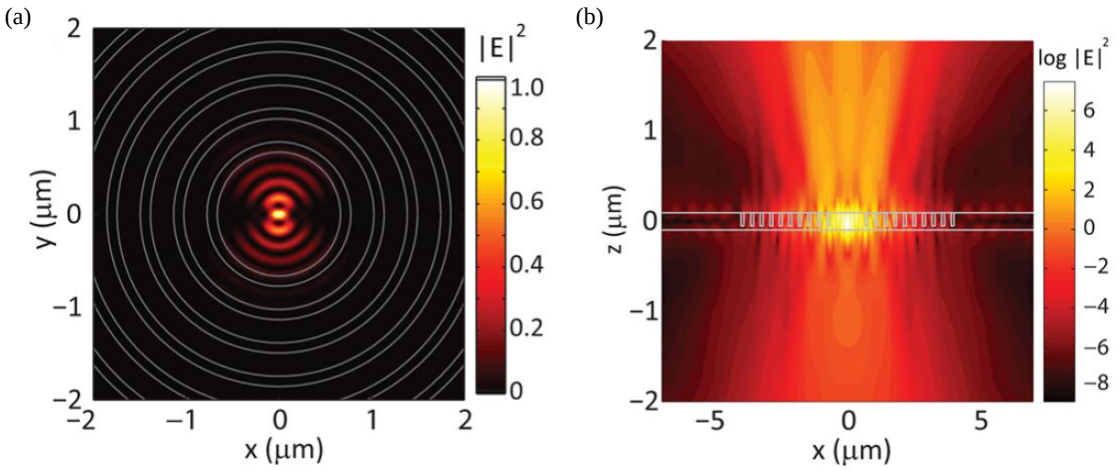

Figure 2.6: Leaky cavity resonances of a 'bullseye' in the (a) xy and (b) xz planes, showing that collection is one-directional and is improved mainly for QDs located in the center of the structure. Figure from Ref. [14].

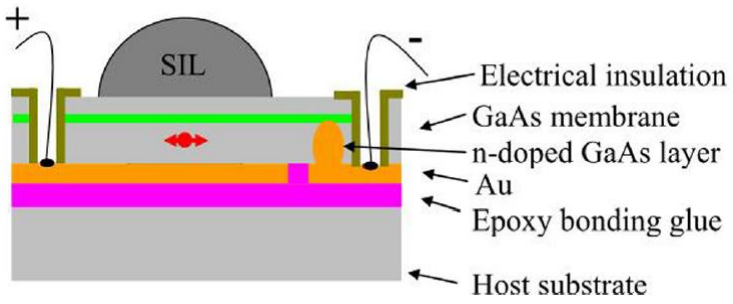

Figure 2.7: Processed GaAs membrane structure that allows charge-tuning of the QD state. Figure from Ref. [15].

due to fabrication complications resulting in incomplete etching of the underlying layer (see Fig. 2.5(b)).

Another device to enhance collection from telecommunication wavelength QDs that was considered is analogous to the planar microcavities reported in Ref. [15]. These structures can be used in conjunction with a SIL, and consist of a GaAs membrane with asymmetrical top and bottom mirrors. The bottom mirror is a gold layer, and the top mirror is a distributed Bragg reflector (DBR). Ref. [15] reports that for QDs centered at λ =950 nm with a spectral bandwidth of 110 nm the optimal structure is a second order cavity with the QD layer located in the anti-node. These structures with a TiO_2/SiO_2 DBR show 41% (50%) collection efficiencies with a $NA = 0.68$ ($NA = 1.0$) objective lens and Purcell radiative rate enhancements of

Table 2.3: Layer composition of the wafer to be processed into a planer microcavity for improving photon collection efficiency at $\lambda = 1290$ nm.

Layer size and content	Notes
GaAs 146 nm	
AlAs/GaAs 3 nm/2 nm ×20	Blocking barrier
GaAs 30 nm	Capping layer
$In_{0.18}Ga_{0.82}As$ 4 nm	Quantum well
InAs	QDs
$In_{0.18}Ga_{0.82}As$ 1 nm	Quantum well
GaAs 12 nm	Tunnel barrier
n^+ GaAs 20 nm	Back gate
GaAs 177 nm	
AlAs/GaAs 112.4 nm/95.8 nm unit thickness	Smoothing superlattice
GaAs substrate 2”	

20%.

The proposed membrane structure designed by Dr Yong Ma for QDs emitting around $\lambda = 1290$ nm (see Table 2.3) is a third order cavity with a AlAs/GaAs DBR, and a calculated photon collection efficiency of 46%. The main benefit of a membrane structure such as this over the ‘bullseye’ structure is the ease of implementing charge-tuning of the embedded QDs (see Fig. 2.7).

2.1.6 *p-i-n* diode telecom wavelength QD sample

A QD sample emitting at telecom wavelengths was provided by Toshiba Research Europe, Cambridge Research Laboratory (see Fig. 2.8(a)). Similar to the MISFET wafers, it was grown by molecular beam epitaxy on a GaAs substrate. Emission at longer wavelengths was achieved by the addition of a $In_{0.23}Ga_{0.77}As$ strain relaxation layer (5 nm) found above the QD layer, which was located in a quantum well. Two $Al_{0.75}Ga_{0.25}As$ superlattices located 5 nm below the QD layer and 10 nm above the strain relaxation layer acting as distributed Bragg reflectors helped increase the collection efficiency of the sample. The structure was embedded within the intrinsic region of a *p-i-n* diode which allowed emission energy tuning by varying the electric field applied to the diode [16]. Finally, in order to spatially isolate single QDs the surface of the sample was covered with a 100 nm thick layer of Al with apertures measuring 3 μm in diameter (see Fig. 2.8(b)). The density of QDs on the sample was such that approximately one QD was found in each aperture, making it easier

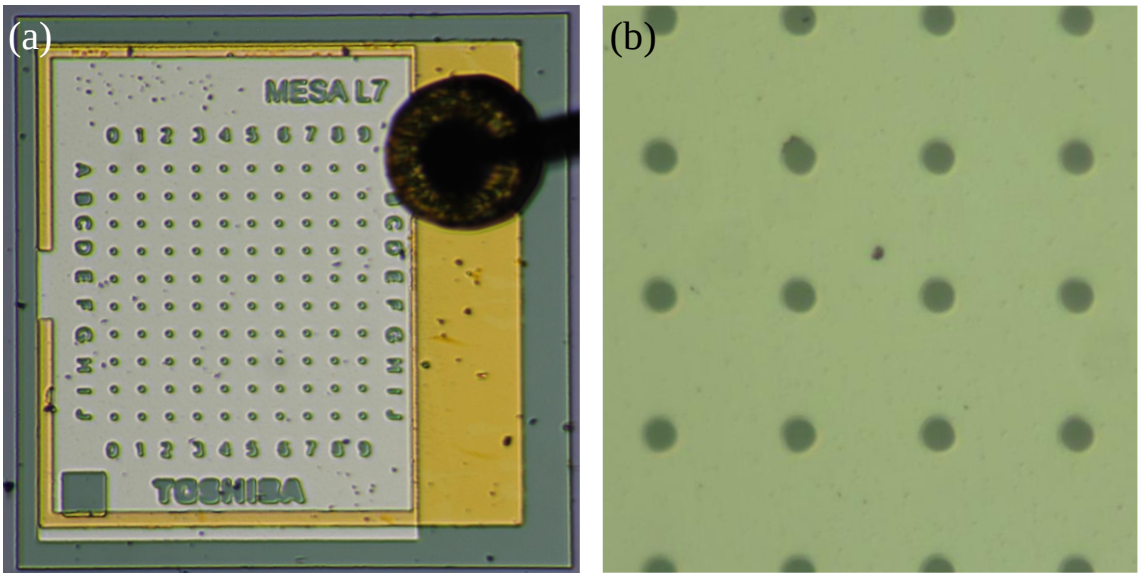

Figure 2.8: (a) Image of the one of the mesas of the *p-i-n* diode structure with embedded QDs used in the second resonance fluorescence experiment. (b) A zoomed-in image showing the roughness of the Al surface. Image provided by Toshiba Research Laboratory, Cambridge.

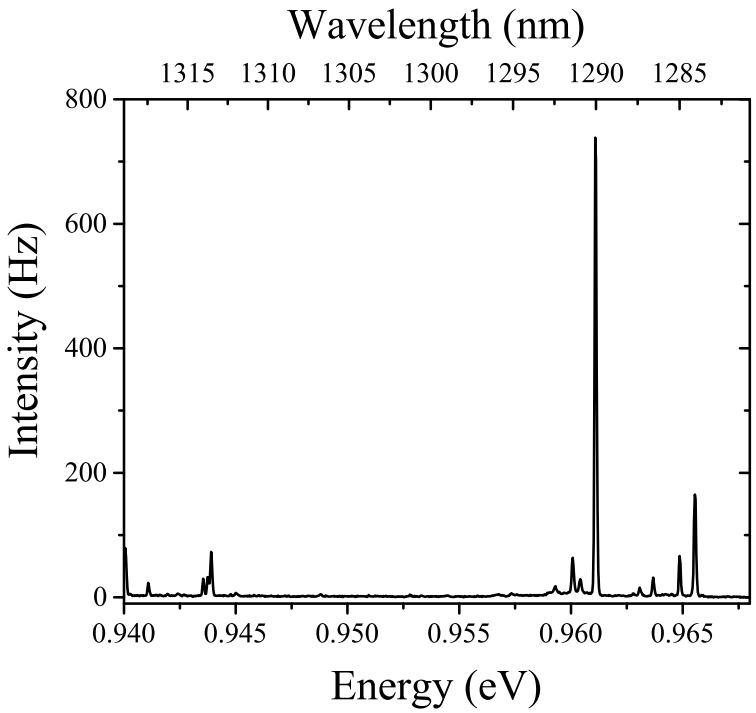

Figure 2.9: Example PL spectra collected from one of the apertures of the *p-i-n* diode structure at 4 K. Excitation was provided by a 1064 nm cw laser.

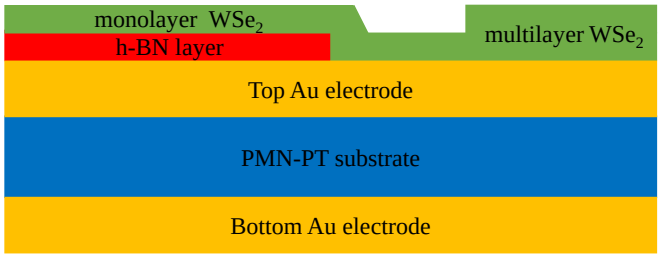

Figure 2.10: A schematic diagram showing the structure of the 'Cairntoul' WSe_2 monolayer sample. The PMN-PT substrate is sandwiched between two gold electrodes. The WSe_2 material, consisting of both monolayer and multilayer structures, is positioned atop the Au layer. Part of the WSe_2 monolayer covers a boron nitride layer that is located on top of the Au electrode.

to identify the quantum dot state. The QD emission wavelength was in the region of $1250 - 1340$ nm (see Fig. 2.9). By changing the bias applied to the device the QD wavelength could be tuned by approximately 30 nm. The voltage was applied to the *p-i-n* diode by a Signal Recovery Model 7265 lock-in amplifier.

2.1.7 WSe_2 monolayer sample

To prepare a WSe_2 monolayer sample the viscoelastic stamping method presented in [17] was used. Its main benefit is the absence of any wet chemicals that have been known to destroy monolayers by capillary forces. The bulk WSe_2 material is mechanically exfoliated onto the viscoelastic layer by stamping. The thinner flakes on the stamp are then visually identified. Final transfer onto the sample wafer is accomplished by pressing the stamp onto the prepared substrate and slowing peeling it off. The flakes detach from the stamp and stick to the substrate wafer.

For the experiments described in this work the 'Cairntoul' WSe_2 monolayer sample (see Fig. 2.10) on a $[Pb(Mg_{1/3}Nb_{2/3})O_3]_{0.72}$-$[PbTiO_3]_{0.28}$ (PMN-PT) substrate with a 100 nm gold surface layer was used. The sample was prepared by Artur Branny. It consisted of several WSe_2 monolayer flakes (see Fig. 2.11), partially located directly on the gold layer, and partially on a boron nitride layer that was deposited above the gold layer. The boron nitride was thought to decease the effects of surface plasmons on emitter photoluminescence. Quantum emitter wavelength tuning was accomplished by varying the bias voltage applied to the PMN-PT

Figure 2.11: Optical micrograph image of the 'Cairntoul' WSe_2 monolayer sample. The gold layer is visible along the bottom of the image and in the top right corner. The blue area represents a WSe_2 multi-layer structure. The large white area in the center of the image is the boron nitride layer. The monolayer flakes (circled in black) are located partially on the gold layer and partially on the boron nitride layer. Image was taken by Artur Branny.

substrate.

2.2 Experimental set-up

The general set-up described in this section was used for all of the experiments conducted. The chosen sample was cooled to 4 K and probed with a high NA confocal microscope, which offered submicron resolution, enabling us to examine a single emitter out of many present in a relatively high density sample. Excitation of PL was provided by a cw or pulsed laser. The PL was detected and spectrally resolved by a spectrometer and a liquid nitrogen-cooled CCD camera system. In the resonance fluorescence (RF) experiments, resonant excitation at $\lambda \approx 1300$ nm and $\lambda \approx 780$ nm was provided by a corresponding tunable cw laser diode from Toptica. Time correlated single photon counting (TCSPS) for time-resolved spectroscopy and RF was performed using single photon detectors and a Picoharp 300 for timing electronics.

2.2.1 Sample set-up within the cryostat

The samples were cooled to temperatures of 4 K by an attoDRY1000 cryogenic system described in Ref. [18]. Its main advantages are ease of use and long-term stability. The temperature of the cryostat was monitored using two calibrated Cernox temperature sensors, one located directly underneath the sample and the other in the cryostat outside the sample tube. A Lakeshore Model 335 Temperature Controller with two sensor inputs was used to read the temperature of the system.

The cryostat system was designed to minimize vibrations by removing contact of the microscope stick with the sample attached and the cold plate by freely suspending the stick within the sample tube. Furthermore, the cryostat was placed on a wooden anti-vibrational platform reducing sample drift and making long-term measurements on a single emitter possible.

The sample was attached by vacuum grease to a set of x-y-z-positioners which was secured on a cage plate. The cage plate with the positioners, the temperature sensor, and the sample were attached to the bottom of a microscope stick designed for the attoDRY1000 with cage rods. A high NA objective lens (Thorlabs C330TME-C with $NA = 0.68$ for experiments on the telecom wavelength QDs and an attocube lens with $NA = 0.82$ for experiments on emitters in WSe_2 monolayers) was placed above the sample and secured to the cage rods. The distance between the sample and the objective was chosen to be slightly larger than the working distance of the lens to avoid damage to both the lens and the sample during the cooling down process. The microscope stick was placed into a attoDRY1000 sample tube, the top of the tube was covered with an 1 in diameter anti-reflective window (Thorlabs parts WG11050-C for experiments on the telecom wavelength QDs and WG11050 for experiments on emitters in WSe_2 monolayers) located inside a cage plate, finally, the stick was secured to the sample tube with a clamp. The cage plate on top of the microscope stick held the microscope head using the cage rods (Thorlabs ER series assembly rods) at the bottom part of the head. Before being inserted into the cryostat the sample tube was pumped down with a turbo pump to at least 10^{-4} mbar, 10-20 mbar of helium exchange gas was added to the tube to facilitate cooling of the sample. Once the tube was loaded into the attoDRY1000, it took about 2 hours to reach temperatures of around 4 K. For experiments requiring the use of a piezoelectric material, the helium pressure had to be significantly lower to

avoid damage to it through short circuiting. In such cases the lowest temperatures reached were about 8 K.

External magnetic fields up to 9 T could be applied to the sample using a superconducting magnet built into the cryostat. The orientation of the magnetic field relative to the sample could be changed by using a different sample mount. The most commonly used way of orienting the sample was in the horizontal position, which corresponded to the the magnetic field being applied in the Faraday configuration. If a magnetic field oriented in the Voigt configuration was needed, the sample had to be positioned vertically on a attocube Voigt geometry mount, and a special objective lens (attocube part IWDO) used. For measurements that required the application of a magnetic field, particular care had to be taken to position the sample exactly 767.3 cm from the top of the microscope stick, which corresponded to the center of the magnetic field once the sample was placed inside the cryostat. Additionally, the use of magnetic metals, such as nickel, within a 1 m radius from the cryostat had to be avoided, since they caused distortions in the magnetic field. A Cryomagnetics 4G Superconducting Magnet Power Supply was used for powering the magnet and reading and controlling the magnetic field value.

Preliminary alignment of the microscope head was carried out before the microscope stick was placed into the sample tube. After the placing the sample into the tube the alignment procedure was repeated, since tightening the clamp holding the stick and the tube together often resulted in small shifts in the propagation direction of light. This is particularly important for samples with telecom wavelength QDs with SILs, since for optimal collection the incident laser light had to pass directly through the top of the SIL. The preliminary alignment procedure made it easier to align on the sample after cool down, facilitating troubleshooting if problems with alignment occurred.

2.2.2 Pulse tube system

As described in Ref. [18]. The attoDRY1000 cryogenic unit is a pulse tube system (see Fig. 2.12). A free-standing compressor is linked to a heat exchanger, which is in contact with the regenerator with high heat capacity. The other end of the regenerator is connected to another heat exchanger called the cold plate. Next to the cold plate is the pulse tube, its other end connected to another heat exchanger,

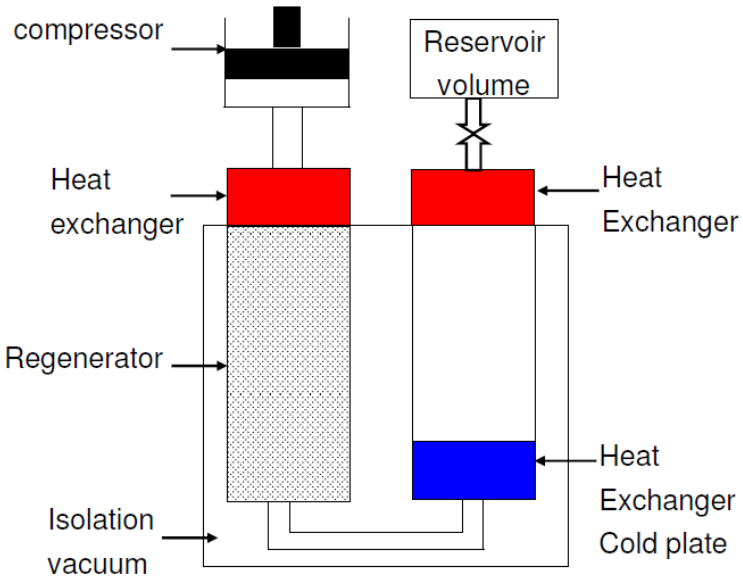

Figure 2.12: Pulse tube system used in the attoDRY1000 cryogenic unit. Figure from Ref. [18].

which is linked to a reservoir volume through the orifice. The reservoir volume is large enough to compensate for compression and expansion of gas caused by the piston in the compressor. The regenerator, cold plate and pulse tube are located within the isolation vacuum. The working gas in attoDRY1000 is helium because of its low condensation temperature, allowing the system to be cooled to 4 K. The periodic movement of the piston displaces the working gas within the system. In the first half of the cycle the gas is compressed, consequently its temperature rises. The extra heat is transferred to the cooling water by the heat exchanger near the orifice. In the second half of the cycle expansion occurs, which results in further cooling of the exchange gas. The regenerator stores heat from the gas flowing through it during compression and releases it during expansion. The heat is then passed to a heat exchanger and from there to the cooling water.

Since this is a closed circuit system, additional helium is required only when the sample tube is being taken out or put into the cryostat in order to prevent condensation. When setting the system up, the isolation vacuum and the outer sample tube need to be pumped down to at least 10^{-4} mbar, which usually takes a few hours for the outer sample tube and overnight for the isolation vacuum. Cooling of the system to 4 K takes about 10 hours.

2.2.3 Electronics

Pin cables built into the microscope stick made it possible to control the *x*-*y*-*z*-positioners, the sample temperature sensor, and the bias applied to the piezoelectric material or to the telecom wavelength QD charge-tunable sample after the stick was placed into the sample tube and sealed. An attocube ACC50 carrier with push-pull connector input and BNC connector output served as a connector unit between various controllers and the pin cables built into the microscope stick. For instance the Cernox temperature sensor located near the sample was connected to a pin socket in the microscope stick, the wires were then connected to a push-pull connector in the top of the microscope stick and linked to the ACC50 carrier unit. The ACC50 accepted the cable from the microscope stick and its output was connected to the Lakeshore Model 335 Temperature Controller that displayed the temperature.

2.2.4 Nanopositioners and scanners

To allow fine alignment on a specific QD or emitter in a WSe_2 monolayer, a way to achieve high precision movement of the sample in relation to the objective lens was necessary. For these experiments a set of attocube linear nanopositioners designed for applications at 4 K, in high vacuum, and in high magnetic fields was used. A motor stack set used in the experiments was normally made of a total of three nanopositioners. Two ANPx101 positioners oriented so that their travel directions were orthogonal to each other allowed complete control of the sample position in the horizontal plane. An ANPz101 positioner allowed sample movement in the vertical direction and was used to bring the sample into focus.

The working principle of the nanopositioners is described in Ref. [19]. The frame of the nanopositioner is made of titanium, a non-magnetic metal, so the positioner did not cause distortions in magnetic fields. The ANPx101 and ANPz101 positioners operate using the same principle. The movement of the positioner is accomplished by a piezo actuator. When the voltage applied to the piezo actuator is slowly swept from $V_{start} = 0$ V to $V_{end} = V_0$, the piezo expands, but the positioner stage stays in place due to static friction. When the voltage sharply drops to zero, the piezo quickly contracts and the induced force overcomes the static friction, resulting in the movement of the positioner stage. This movement corresponds to one step of the nanopositioner. The total travel range of the positioners is about 5 mm, and

the minimum step size is 50 nm (10 nm) at 300 K (4 K). The triangular electrical pulses needed to expand and contract the piezo were provided by an attocube Piezo Step Controller ANC150. The amplitude of the applied voltage should be in the range of 0-150 V at 4 K, and the frequency of the pulses should not exceed 1000 Hz. A working positioner has a capacitance of approximately 1 μF (200 nF) at 300 K (4 K). Spacial care had to be taken when cooling down or warming up the motor stack, since in such conditions piezo actuators may change dimensions leading to an accumulation of charge, which may damage the piezo. This is prevented by grounding the nanopositioner.

One of the main problems encountered when using these nanopositioners is drift in an orthogonal direction which often accompanies movement. In particular, movement of the sample in the vertical direction often results in drift in the horizontal plane. However, this effect was found to decrease significantly when positioners were moved with single steps.

For even finer position control an ANSxy100 series piezo scanner was used in addition to the motor stack described above. The scanner allowed subnanometer fine positioning resolution in the horizontal plane. It operated using the same principle as the nanopositioners. The scan range was 40×40 μm^2 (9×9 μm^2) at 300 K (4 K). In this work, the scanner was primarily used for taking high-resolution spatial maps of the monolayer WSe_2 flakes. Notably, the scanner has minimal hysteresis.

2.2.5 Voltage adder/divider unit

Following a first unsuccessful attempt to find RF from a telecom wavelength charge-tunable structure, a potential problem with the set-up was identified. The expected linewidth of the RF signal from the telecom wavelength charge-tunable QD sample was about 1 μeV, which corresponded to a minimum voltage step of 0.25 mV (the Stark shift for the sample used was about 0.004 eV/V). However, the auxiliary DAC outputs of Signal Recovery Model 7265 lock-in amplifier used for charging the QDs had a resolution of 0.001 V [20], which may have resulted to the RF signal being 'stepped over' in a voltage sweep. To prevent this a voltage adder/divider unit was designed to decrease the smallest step size to 0.05 mV. The inputs of the unit are the auxiliary DAC outputs of the lock-in (V_1 and V_2). The unit accomplished the following functions: dividing (V_0=V_1/200) and adding (V_{out}=0.91(V_0+V_2)).

Assuming a 1 μeV linewidth of the RF signal, an increase in signal should be seen over 4-5 steps during a voltage sweep when using the adder/divider unit.

Ultimately, the unit was not used, since the real linewidth of the RF signal from the telecom wavelength QDs was found to be close to 100 μeV, and the difficulty in finding a signal was actually due to its low intensity (see Chapter 4).

2.2.6 Strain tuning

In the WSe_2 RF experiment emitter wavelength tuning was initially planned to be accomplished though strain tuning using a PMN-PT stack. The material was contacted, with the top electrode grounded and bias applied to bottom one using a high voltage supply unit. At room temperature the piezoelectric material could be tuned from 30 V to 300 V. Before cooling down, the domains were aligned in one direction. At 4 K the material could be tuned from -300 V to 2000 V, corresponding to emission wavelength tuning of about 10 meV.

2.2.7 Confocal microscope heads

Four slightly different configurations of confocal microscope heads were built for experiments described in this work. The main differences between their design was determined by whether they were meant to be used for RF or PL.

In general, all four experimental set-ups consisted of the same main parts (see Fig. 2.13). The excitation arm of the microscope head was fiber-coupled to the excitation laser. The fiber output of the collection arm could be switched between a spectrometer and a single photon detector, as needed. The two arms were fixed onto a metal frame made of two cubes, with each cube containing a beamsplitter. A portion of the laser beam coming from the fiber coupled to the excitation arm was reflected from the first beamsplitter and propagated downward towards the sample. The portion of the laser beam that passed through the first beamsplitter was detected by the mounted photodiode fixed on the side of the bottommost cube, making it possible to monitor the laser power at the sample with some simple calculations. Most of the light reflected and emitted from the sample passed through both beamsplitters and was collected into the fiber of the collection arm, from where it was sent to the relevant detector. A portion of the upward propagating light was reflected from the second beamsplitter and directed to the imaging camera located

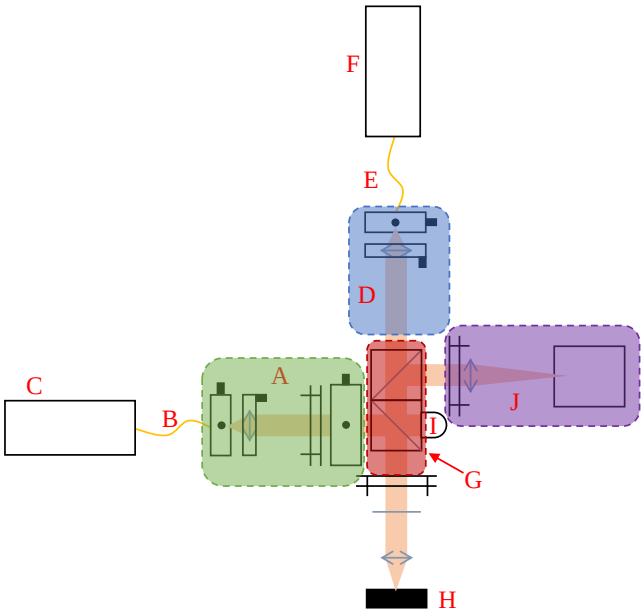

Figure 2.13: A schematic of the basic experimental set-up used for experiments in this work: the excitation arm A fiber-coupled (B) to the excitation laser C, the collection arm D fiber-coupled (E) to a detector F, the metal two-cube frame G, the sample H, the photodiode I, and the imaging camera arm J.

opposite the top cube. The image on the camera was used to align the system.

2.2.8 Alignment procedure of a confocal microscope head

The initial alignment procedure of the microscope head is described below (see Fig. 2.14). The design of the microscope allows for easy removal of the excitation and collection arms from the rest of the head. First, both arms are removed from the head and connected to the appropriate fiber. The purpose of the first step of alignment is to position the fiber opposite the center of the Thorlabs mounted aspheric lens *1*. Collimation of laser light is accomplished using Thorlabs z-axis translation mount *2* over two lengths of the optical table ($\sim$ 8 m in total). Next, using the xy translating lens mount *3* the beam is centered by being made to pass though a set of irises. The collimation and alignment steps are normally repeated several times in turn. After these steps are accomplished, the fibers should preferably not be removed from the arms, because replacing them will cause small shifts in the

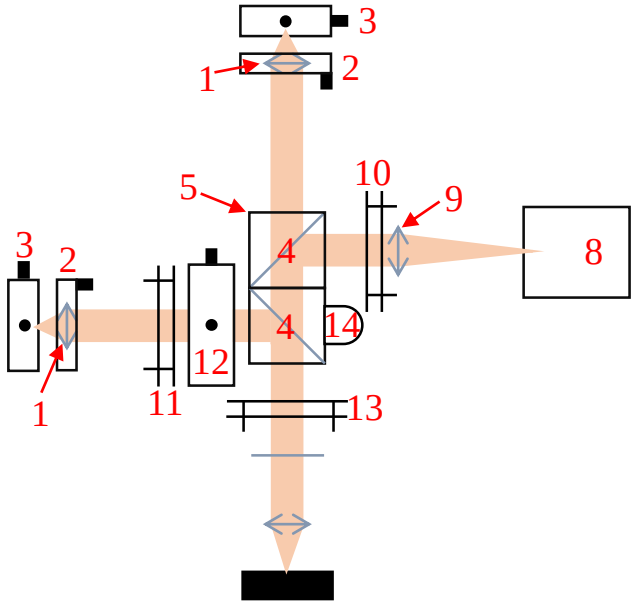

Figure 2.14: The components of a typical confocal microscope head used for experiments in this work: aspheric lenses *1* mounted on z-axis translation stages *2*, xy translating lens mount *3*, beamsplitters *4* located within the two-cube metal frame *5* held by optic mounts *6* (not shown) on fixed cage cube platforms *7* (not shown), imaging camera *8*, achromatic doublet *9*, reinforced tilt stages *10*, *11*, and *13*, a xy translation stage *12*, and a photodiode *14*.

fiber position, causing misalignment. Additionally, the z-axis translation mount and the xy translating lens mount are not to be adjusted any further, since that will cause the fiber to move away from the position at the center of the aspheric lens.

Next the beamsplitters *4* within the two-cube metal frame *5* are aligned. Optic mounts *6* on fixed cage cube platform *7* are used to hold the beamsplitters and secure them within the cubes. The excitation arm is replaced on the head, and system is positioned sideways on the optical table using posts, post holders, and cage plates as needed. The position of the beamsplitter opposite the excitation arm is chosen so that laser light reflected from it makes a right angle with the incident beam, propagating in the direction where the sample will be placed. Irises are used to make sure the reflected light is centered. Next, the collection arm is positioned on the metal frame. The first beamsplitter walks the laser beam propagating from the collection

arm in the direction of the sample, shifting it slightly away from the center axis. The purpose of the second beamsplitter is to compensate for this shift. Choosing the correct position of the second beamsplitter is particularly important because it determines the degree to which the light emitted from the sample is collected into the fiber. Most of the collected light passes through the second beamsplitter, but a small portion is reflected in the direction of the imaging camera *8*. An achromatic doublet *9* with a focal length of 150 mm is used to focus the image on the camera. The correct distance between the doublet and the camera is chosen by sending a collimated and centered beam though the doublet to the camera and finding the position of the lens that gives the smallest spot size on the camera. A tilt stage *10* reinforced with extra springs is used to adjust the angle of the beam propagating toward the camera as needed.

The above steps should ideally be accomplished without the use of the additional reinforced tilt stage and the *xy* translation stage on the excitation arm. Parts *11* and *12* are added to the excitation arm after the beamsplitters are secured to perform fine adjustment of the arm, if necessary. Reinforced tilt stage *13* is positioned at the bottom of the head to adjust the orientation of the entire head in order to align on the sample. If the system is aligned correctly, the beam from the excitation arm should fit completely on the photodiode *14*. The microscope heads were compatible with Thorlabs 30 mm cage systems, and various cage rods and cages were used as needed. Once these steps are completed, the initial alignment of the microscope head is complete.

For further alignment for a specific experiment the head is positioned vertically on a microscope stick with the sample placed at the bottom of the stick on a motor stack. First, the laser beam propagating downward from the collection arm is centered using reinforced tilt stage *13*. The camera image of the beam reflected from the sample should not travel in-plane when the sample moves in the vertical direction. Next, the alignment of the excitation arm is adjusted using the reinforced tilt stage *11* and *xy* translation stage *12*. The laser beam from the excitation arm should overlap with the beam from the collection arm, which can be easily monitored either on the imaging camera or on a detector card.

By following the above steps it is possible to align the microscope head on a flat sample such as a WSe_2 monolayer without difficulty. However, when the sample contains a SIL, the alignment is complicated by the fact that for optimal collection

the laser beam should pass directly through the top of the SIL. The degree to which this is accomplished can be monitored by moving the sample along the vertical axis. If the spot on the camera becomes elliptical, the laser beam is not well centered on the SIL.

The anti-reflection coating of the optics in the head was always chosen with the design wavelength in mind. For the telecom wavelength experiments optics with a C coating were used (spectral range 1050-1620 nm), and, for the experiments on emitters localized on defects in WSe_2 monolayers, optics with a B coating (spectral range 600-1050 nm) were used.

Finally, it should be noted that the wavelength of the lasers used for aligning the excitation arm of the microscope head in the above procedure should correspond to the wavelength of the excitation laser used in the experiment. The collection arm should be aligned using a laser with a wavelength resonant with the sample emission.

A good way to check how well the microscope head is aligned on the sample is by calculating the efficiency of the system, more specifically, how effectively the laser light from the excitation arm is collected by the fiber of the collection arm after its reflection from the sample.

$$\eta_{eff} = \frac{P_{coll}}{P_{exc}}. \tag{7}$$

Here P_{coll} is the power of the laser light reflected from the sample and collected into the fiber in the collection arm, and P_{exc} is the power measured on the photodiode opposite the excitation arm. Taking into account the transmission and reflectance of all optical elements in the system, an efficiency of 2.3% is expected in the case of perfect alignment. Good alignment corresponds to efficiencies of better than 1%.

2.2.9 Modifications of a confocal microscope head

In total four microscope heads were built for non-resonant and resonant excitation of telecom wavelength QDs ($\lambda = 1300$ nm) and emitters localized on defects in WSe_2 monolayers ($\lambda = 760$ nm) (see Table 2.4).

The microscope head shown in Fig. 2.14 and described above can be used for PL experiments on telecom wavelength QDs and, with the addition of a 532 nm notch filter to the collection arm to filter out the scattered excitation laser photons, emitters in WSe_2 monolayers. For RF experiments the following modifications to

Table 2.4: Parts of the four confocal microscope heads used for experiments in this work. All parts were bought from Thorlabs, unless otherwise stated. The part numbers in italic correspond to those in Fig. 2.14 and Fig. 2.15.

Part	**λ =1300 nm PL head**	**λ =1300 nm RF head**	**λ =780 nm PL head**	**λ =780 nm RF head**
1	C280TME-C		C280TME-B	
2	SM1Z			
3	CXY1			
4	WG11050		Semrock FF562-Di03-25×36	WG11050
5	Metal frame made of two cubes C4W			
6	B5C		FFM1	B5C
7	B3C/M			B4CRP/M
8	Starlight Xpress Lodestar X2 Camera		Hamamatsu InGaAs Camera C10633	
9	AC254-150-C-ML		AC254-150-B-ML	
10	reinforced KC1-T/M			
11	reinforced KC1-T/M			
12	ST1XY-D/M			
13	reinforced KC1-T/M			
14	SM1PD1A	SM1PD5A	SM1PD1A	
15	-	CODIXX IR 075 BC8	-	CODIXX VIS 074 BC8
16	-	CRM1P/M	-	CRM1P/M
17	-	AQWP05M-1600	-	Edmund Optics 1/4W610-850NM
18	-	CODIXX IR 075 BC8	-	CODIXX VIS 074 BC8
19	-	attocube ANR240	-	attocube ECR4040
20	-	C4W		
21	-	Glass sample slide		
22	-	B3C/M with slot		
23	-	M1300L3	While light source	

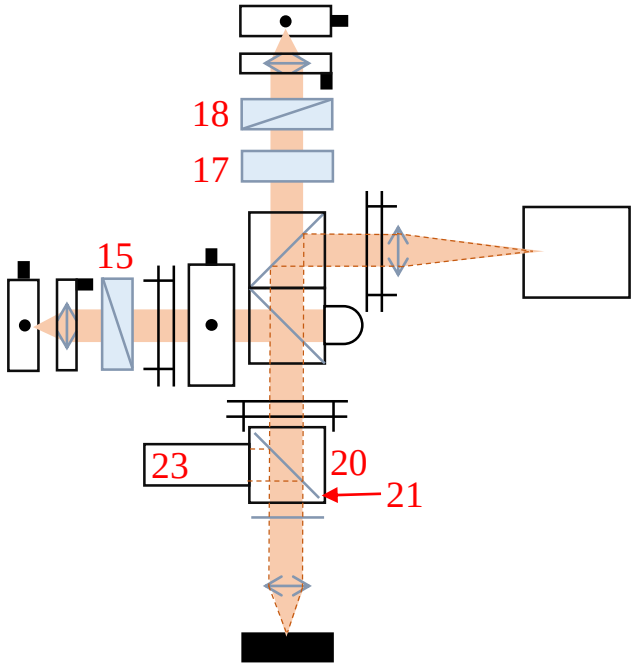

Figure 2.15: The components of possible modifications of a typical confocal microscope head used for experiments in this work. RF head modification: CODIXX polarizers *15* on a precision cage rotation mount *16* (not shown) and *18* on an attocube rotator *19* (not shown), and an achromatic quarter-wave plate *17* on an attocube rotator *19* (not shown). Sample imaging modification: a metal cube *20* with a glass slide *21* held by a fixed cage cube platform *22* (not shown), and a light source *23*. The dashed lined indicate the propagation direction of the light used for imaging.

the head have to be made (see Fig. 2.15). A high quality CODIXX polarizer *15* on a Thorlabs precision cage rotation mount *16* is placed on the excitation arm. A mounted achromatic quarter-wave plate *17* and a CODIXX polarizer *18* on attocube rotators *19* are placed in the collection arm. The purpose of this modification is to achieve cancellation of the scattered excitation laser light, while letting 50% of the signal from the sample through. The rotators operate using the same principle as the attocube nanopositioners and scanners (see Section 2.2.4).

Any one of the four microscope heads can be modified to allow imaging of the sample surface (see Fig. 2.15). To do that, an additional cube *20* is inserted below the reinforced tilt stage *13*. A glass slide *21* forming a 45° angle with the beam from

the excitation arm is inserted inside the cube. The glass plate is held in place by a fixed cage cube platform with a slot drilled in it *22*. A light source *23* is positioned so that its reflected rays propagate towards the sample. For the experiment with telecom wavelength QDs embedded in a *p-i-n* diode a 1300 nm LED was used as the light source, and white light was used for imaging WSe_2 monolayers. The image of the sample surface is then seen on the imaging camera. The main advantage of this set-up is the ease with which the glass slide can be taken out of the cube and later replaced requiring minimal re-alignment.

The resolution of the microscope heads calculated using Eq. 3 is $\Gamma = 975$ nm for the telecom wavelength experiments (half of that for sample with a h-SIL), and $\Gamma = 485$ nm for the experiments on emitters in WSe_2 monolayers.

2.2.10 Polarizer calibration

The collection arm could be modified to analyze the polarization of the collected light. To do that a Meadowlark Optics liquid crystal variable retarder, a quarter-wave plate, and a linear polarizer are added to the collection arm in the above order (see Fig. 2.16), with the retarder located closer to the sample. The fast axis of the liquid crystal retarder was oriented at a 45° angle relative to the fast axes of the other two optical elements. The retarder acts as a half-wave plate, and is made of two fused silica windows, with the cavity between them filled by a nematic liquid crystals material, its birefringence dependent on the applied AC voltage. When no voltage is applied the liquid crystals are aligned parallel to the windows, and the retardance is maximum. As the applied voltage is increased, the molecules align closer to the direction perpendicular to the windows, reducing retardance. A Meadowlark Optics liquid crystal digital controller D3050 is used to apply voltage to the retarder. Before use the retarder had to be calibrated by assigning angle values to the applied voltage.

2.2.11 Photoluminescence set-up

Excitation of PL for the experiments on emitters in a WSe_2 monolayer was provided by a $\lambda = 532$ nm cw laser, while for the experiments on telecom wavelength QDs a $\lambda = 830$ nm (cw or pulsed) or a $\lambda = 1064$ nm (cw) laser was used.

Two Acton Research Corporation SpectraPro-500i spectrometers with triple

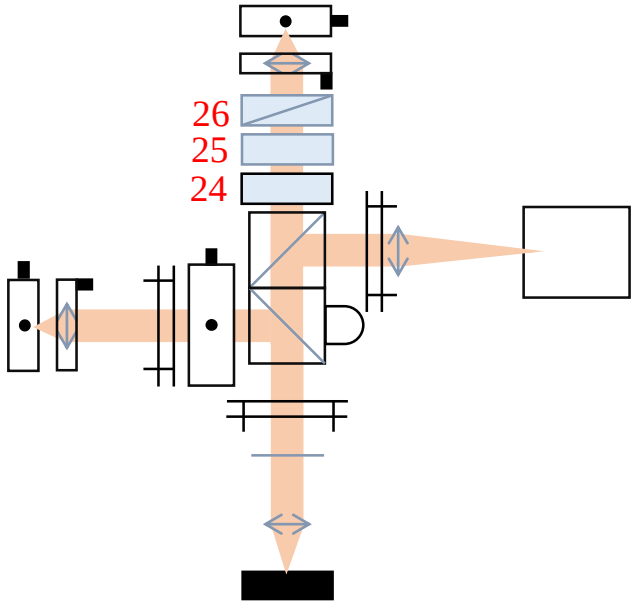

Figure 2.16: A modifications of a typical confocal microscope head used for analyzing the polarization of the light collected from the sample: *24* is a liquid crystal variable retarder (designed for $\lambda \approx 1300$ nm or $\lambda \approx 780$ nm) mounted on a modified Thorlabs cage plate CP02T/M, *25* is an achromatic quarter-wave plate (Thorlabs AQWP05M-1600 or Edmund Optics 1/4W610-850NM), and *26* is a linear polarizer (CODIXX IR 075 BC8 or CODIXX VIS 074 BC8). The fast axes of the polarizer and the wave plate were aligned and formed a 45° angle with the fast axis of the retarder.

grating turrets and focal lengths of 0.5 m were used to detect and spectrally resolve the PL. For the telecom wavelength experiments the gratings were a 150 grooves/mm grating blazed at 1.2 μm, a 830 grooves/mm grating blazed at 1.2 μm, and a 1200 grooves/mm grating blazed at 750 nm. The spectrometer was equipped with a back illuminated liquid nitrogen cooled InGaAs CCD camera system. The InGaAs detector contained a 1×1024 linear array of pixels (500 μm × 25 μm). About 70 electrons were needed to register a count on the detector, which made this detector far less sensitive than the Si detectors used at $\lambda = 950$ nm, for which this value is 2. The resolution of the spectrometer was 1 meV, 130 μeV, and 70 μeV for the 150, 830, and 1200 grooves/mm gratings, respectively. The fiber from the collection arm

of the microscope was coupled to the spectrometer, a C220TME-C lens was used for collimating the input beam and a AC127-019-C for focusing. The performance of the spectrometer was dependent on the polarization of the incoming light, so a linear polarizer LPNIR050-MP2 was placed between the two lenses. The low-resolution grating was used primarily for alignment purposes, since PL from single QDs could not be distinguished on it. For most experiments, the aim was to work with the 1200 grooves/mm grating at all times, since it offers the best resolution. The typical spectral linewidth of the charge-tunable QDs (about 0.08 nm at $\lambda = 1300$ nm) was limited by the spectrometer resolution. In the experiment where the magnetic field was applied to the sample in the Voigt geometry, the counts decreased significantly due to the QD PL line splitting into four at high magnetic fields, and most measurements were performed on the 830 grooves/mm grating.

For the experiments on emitters localized on defects in WSe_2 monolayers the gratings were a 300 grooves/mm grating blazed at 500 nm, a 1200 grooves/mm grating blazed at 750 nm, and a 1800 grooves/mm grating blazed at 500 nm. The resolution of the spectrometer was 400 μeV, 90 μeV, and 30 μeV for the 300, 1200, and 1800 grooves/mm gratings, respectively. The camera was a back illuminated liquid nitrogen cooled Si CCD camera. The detector array was 1340×100 with pixel size of 20 μm $\times$ 20 μm. The input of the spectrometer was collimated by a AC254-075-B-ML lens and focused by a C280TME-B lens. A CODIXX VIS 074 BC8 linear polarizer was placed between the lenses.

2.2.12 Single photon detection

Time-resolved PL, second-order correlation function measurements, and RF required counting individual photons. To achieve that the photon detection events first have to be converted to electrical signals. For time-resolved PL measurements this was accomplished by a single photon detector (channel 1) in combination with the sync signal of the pulsed excitation laser (channel 0). Two single photon detectors (one on each channel) were used for measurements of the second-order correlation function. The electrical signals were each sent to a Time to Amplitude Converter (TAC), which generated voltage that was linearly proportional to the time between the start (channel 0) and the stop (channel 1) pulses. The generated voltage was then sent to a Analog to Digital Converter (ADC). The number of detection counts in

each time bin was stored in PC memory. In more advanced units the TAC and the ADC are combined into a single unit called a Time to Digital Converter (TDC), which allowed for a much shorter electronic dead time. For experiments described in this work a PicoQuant Picoharp 300 was used, which utilized two independent TDC, one each for the start and the stop signal [21].

Picoharp 300 used Time-Correlated Single Photon Counting (TCSPC) to record temporal data, in which the data were collected over many cycles, and a histogram of the timing of photon registration was extracted. An experiment utilizing TCSPC should be set-up so that the probability of registering two stop photons for each start photon is negligible. Otherwise, due to the dead time of the detector, only the first photon would be registered, and the resultant histogram would not be an accurate representation of reality.

Fiber-coupled PerkinElmer Optoelectronics Si single-photon avalanche diodes SPCM-AQRH (SPADs) [22] were used for single photon counting in experiments on WSe_2 monolayers. In the inactive state the device was biased above the breakdown voltage (Geiger mode), with a high electric field in the depletion region of a semiconductor *p-n* junction, but with no free carriers present [23]. When light is absorbed in the depletion region carriers are photo-generated. The electric field in the device acts to accelerate the electrons and holes, which upon impact generate additional electron-hole pairs, creating an avalanche multiplication process [23]. Therefore, a single photon can create a macroscopic avalanche current, which is quenched by lowering the applied bias after the photon has been detected [23]. The typical efficiency of the detector used is about 50% at $\lambda = 780$ nm, the dead time is set at 35 ns. When the unit is covered in blackout material, the dark counts are typically less than 100 Hz.

For single photon detection in experiments on QDs emitting at telecom wavelengths a Superconducting Nanowire Single Photon Detector (SNSPD) at 2.8 K was used. These infrared detectors have been shown to have low dark counts, short dead times and low jitter [24]. The device consisted of a NbTiN meander wire 100 nm wide and 6 nm thick covering a 10×10 μm^2 area located on a layer of SiO_2 atop a Si substrate [25]. The thickness of the SiO_2 layer was chosen so that it formed a half cavity for the desired wavelength of the absorbed photons (in our case 225 nm for $\lambda = 1310$ nm). An input fiber was aligned to the detection region [24]. The NbTiN wire is in the superconducting state at temperatures below 8 K, and in the absence

of absorbed photons acts as a closed switch for the bias current applied to it. When a photon is absorbed by the wire, a resistive region within it is formed, opening the switch and generating a voltage pulse [25]. The efficiency of the detectors increases with bias current, but is also accompanied by an increase in dark counts [24]. The detection efficiency of the system was about 3% at 1.3 μm, and the jitter was measured to be 220 ps, higher than the 50 ps reported in literature [24–26]. The detector was provided and set-up by Dr Michael Tanner and Prof Robert Hadfield of the University of Glasgow.

As an alternative to the SNSPDs, an ID Quantique id220-FR-SMF fiber-coupled SPAD [27] cooled to 90 K was used. The InGaAs/InP avalanche photodiode operated at 193 K. This detector was designed to prevent afterpulsing, which normally lead to high dark count rates. The efficiency of the SPAD was 20% with a 25 μs dead time. It was found to be slightly more effective than the SNSPDs.

2.2.13 Lasers and laser control for RF

Two Toptica Photonics Grating Stabilized Diode Laser Heads designed for DLC pro were used for the RF experiments at $\lambda \approx 1300$ nm and $\lambda \approx 780$ nm. The lasers had a coherence length of more than 100 m. The emission was collimated and had an elliptical beam waist. The emission of the $\lambda \approx 1300$ nm laser was analyzed with a Fabry-Pérot interferometer (FPI) and the fringes were found to be equidistant and had the same amplitude, proving that the emission was single mode. Likewise, the $\lambda \approx 780$ nm laser was tuned over a large interval of wavelengths without experiencing modehopping, indicating that the emission was single mode. The ranges of wavelengths for the laser was 1248 nm to 1358 nm and 753 nm to 816 nm, and the output power 50 mW and 130 mW, respectively.

These external-cavity diode lasers have a Littrow configuration [28]. The light emitted from the laser diode passes though a short focal length lens, and the resultant collimated beam is incident on a reflection grating. The angle of incidence and the diffraction angle are identical, resulting in the first order diffraction of beam incident on the grating being back-reflected towards the collimation lens and focused in the laser diode resonator. Since the reflectivity of the grating is higher than that of the front panel of the internal resonator, an external resonator between the grating and the back panel of the internal laser diode resonator was formed.

The external resonator is much longer (a few cm) compared to the internal one (100 μm), further decreasing the emission linewidth. Emission wavelength tuning is accomplished by adjusting the angle of the reflection grating. Coarse wavelength tuning is accomplished by manually adjusting the grating angle with a 2.5 mm Allen key.

The lasers were secured directly on metal breadboards to improve acoustic and thermal stability. The use of optical isolators was necessary to reduce reflection of the laser beam off optical elements in front of the laser back to the laser diode, which can cause noise, amplitude fluctuations, multimode emission and even permanent damage to the diode. An optical isolator was installed inside the $\lambda \approx 780$ nm laser. For the $\lambda \approx 1300$ nm laser a Thorlabs optical isolator IO-4-1310-VLP was used. The isolator was made of two linear polarizers with a Faraday rotator located between them. In the forward mode the linearly polarized light that passed through the first polarizer was rotated by 45° by the Faraday rotator and passed though the second linear polarizer, which was rotated by a 45° angle relative to the first one. In the reverse mode the light transmitted by the second polarizer was rotated by 45° relative to the first one, and upon passing the Faraday rotator was rotated a further 45°, becoming blocked by the first linear polarizer.

The output of the lasers was coupled into one of the ends of a 90/10 fiber coupler, with 10% of the collected light being sent to the wavelength meter. 90% of light coupled out of the laser was sent through a Fiberstore Variable Fiber Optic Attenuator ATA-FCA-FS and then through a system of manual fiber polarization controllers FPC030 to optimize the signal, and finally, to the excitation arm of the microscope head.

A Toptica Photonics Digital Laser Controller was used to provide current and temperature control and stabilization of the lasers. Additionally the controller could drive a piezoelectric element located within the laser to make small adjustments to the angle of the reflection grating, fine-tuning the wavelength [29].

As an alternative to the Toptica Photonics laser, a Sacher Lasertechnik Group Lion External Cavity Laser was used for resonant excitation at $\lambda \approx 1300$ nm [30]. The laser set-up was similar to the one described above for the Toptica Photonics lasers, but the performance of this laser was not as good. Modehopping occurred over shorter wavelength ranges.

2.2.14 Wavelength meter

A HighFinesse Ångstrom WS/7 IR Wavelength Meter with a Multichannel Switch was used for monitoring and controlling the wavelength of the laser output. The unit could work in the $800 - 1750$ nm wavelength range and control up to two lasers at a time. About 10% of the light emitted by the laser was coupled via fiber to the multichannel switch, and through it to the Wavelength Meter. In the Wavelength Meter after the beam was collimated by a mirror, it traveled to a configuration made of two sets of Fizeau interferometers. The generated interference pattern was registered onto a CCD photodiode array, from where the data was sent to a PC [31]. The Wavelength Meter software fitted the data and estimated the wavelength using calibration files. The calibration was done using a HeNe laser. The laser software enabled the use of a proportional-integral-derivative (PID) controller to lock the laser wavelength to a specific value [31]. Wavelength regulation did not slow down the wavelength measurement time.

2.2.15 Cancellation of scattered laser light

In the RF experiments, suppression of excitation laser light scattered off the surface of the sample was achieved by a combination of orthogonally oriented linear polarizers in the excitation and collection arms with a quarter-wave plate in the collection arm and a single-mode fiber coupled to the collection arm. The mode transmitted by the linear polarizers was orthogonal to the input mode of the single mode fiber, which further suppressed the excitation laser light. The highest measured extinction ratio in this configuration was 10^6 (10^5) for the experiment on telecom wavelength QDs (quantum emitters in WSe_2 monolayers).

2.2.16 Fabry-Pérot interferometer characterization

For high resolution RF measurements at telecom wavelengths a Micron Optics FFP-SI Fiber Fabry-Pérot Scanning Interferometer designed for $\lambda \approx 1310$ nm was used. The free spectral range was measured to be ~ 5.611 GHz, and the resolution was 0.0249 GHz. The cavity, located in fiber, is formed by two mirrors deposited on the input and output fibers, making alignment unnecessary. A piezoelectric actuator was used to scan the length of the cavity by straining the fiber located inside it. The electrical signals of a set frequency used to scan the cavity were provided by

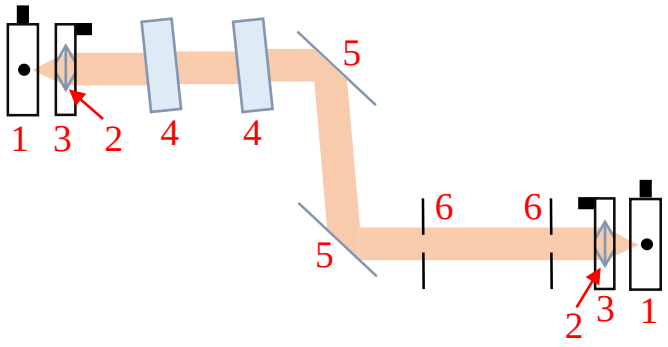

Figure 2.17: Schematic of the filter set-up used in the experiments on emitters in WSe_2 monolayers. *1* corresponds to the xy translating lens mounts for the input and output fibers, *2* are the aspheric lens on a z-axis translation stages *3*. *4* are the two tunable bandpass filters on gimbal mounts, a system of two silver mirrors *5* on a right-angle kinematic mirror mount and two iris diaphragms *6* is used to compensate the slight misalignement caused by adjusting the angle of the tunable bandpass filters.

a function generator. Changing ambient conditions resulted in some drift within the unit, so a reference laser signal was used to track spectral drift of the laser wavelength during experiments. Using the FPI single mode emission of both the Toptica and Sacher telecom wavelength lasers was demonstrated.

2.2.17 Tunable angle-dependent edge filters

A system of tunable angle-dependent edge filters was used to isolate a single peak the PL spectra collected from emitters localized on defects in WSe_2 monolayers. Such a system was necessary for measurements of the second order correlation function under non-resonant excitation, as well as for isolating the signal from the scattered laser light in photoluminescence excitation (PLE) spectroscopy. The resolution of the system was about 1.5 nm (3 meV). The system was fiber-coupled both in the input and the output. An xy translating lens mount CXY1 *1* (see Fig. 2.17) was used to align the input and output fibers to the center of the aspheric lenses C280TME-B *2* fixed on a z-axis translation stages SM1Z *3*. Two Semrock tunable bandpass

filters TBP01-796/12-25.4-D *4* mounted on a Thorlabs gimbal mounts KC45D were located on the input arm about 10 cm apart from each other. The input beam was then reflected off two Thorlabs silver mirrors PF10-03-P01 *5* in a Thorlabs right-angle kinematic mirror mount KCB1/M. Finally, the beam passed through two iris diaphragms SM1D12D *6* and was coupled into the output fiber.

Adjusting the angle of the tunable bandpass filters caused misalignment of the system, and the mirrors and the irises were used to compensate for it. Initial alignment of the system was done for a wavelength of 700 nm, which corresponded to the plane of the tunable bandpass filters forming a 60° angle with the incident beam. Once a small signal was registered (either visually on a piece of white paper or on the low-resolution grating of the spectrometer), it was improved by the adjustment of the first mirror position in conjunction with the gradual closing of the first iris. Next the first iris was opened and the process was repeated for the second mirror and the second iris. These two steps were repeated until the transmission of the filter reached at least 30%. Once the initial alignment was done, the laser input could be exchanged for a white light source, and the filters could be slowly tuned to the desired wavelength.

2.3 Conclusion

In summary, several samples were prepared for investigation in this work: a charge-tunable telecom wavelength QDs device, a *p-i-n* diode with embedded telecom wavelength QDs, and a WSe_2 monolayer. A confocal microscope set-up described in this chapter made possible the study of single photon emission from these samples. Four modifications of microscope heads were built allowing to perform PL and RF measurements at $\lambda \approx 1300$ nm and $\lambda \approx 760$ nm.

2.4 References

[1] P. A. Dalgarno, J. McFarlane, D. Brunner, R. W. Lambert, B. D. Gerardot, R. J. Warburton, K. Karrai, A. Badolato, and P. M. Petroff, Hole recapture limited single photon generation from a single n-type charge-tunable quantum dot, *Applied Physics Letters*, **92**, 193103 (2008).

[2] S. Seidl, M. Kroner, P. A. Dalgarno, A. Högele, J. M. Smith, M. Ediger, B. D. Gerardot, J. M. Garcia, P. M. Petroff, K. Karrai, and R. J. Warburton, Absorption and photoluminescence spectroscopy on a single self-assembled charge-tunable quantum dot, *Physical Review B*, **72**, 195339 (2005).

[3] H. Drexler, D. Leonard, W. Hansen, J. P. Kotthaus, and P. M. Petroff, Spectroscopy of quantum levels in charge-tunable InGaAs quantum dots, *Physical Review Letters*, **73**, 2252 (1994).

[4] Thomas Ihn, *Semiconductor nanostructures: quantum states and electronic transport*, Oxford University Press, (2010).

[5] C. Schneider, S. Höfling, and A. Forchel, Growth of III-V semiconductor quantum dots, In: Alexander Tartakovskii (ed.), *Quantum dots: optics, electron transport and future applications*, 3-20, Cambridge University Press, (2010).

[6] G. Medeiros-Ribeiro, F. G. Pikus, P. M. Petroff, and A. L. Efros, Single-electron charging and Coulomb interaction in InAs self-assembled quantum dot arrays, *Physical Review B*, **55**, 1568 (1997).

[7] Keith A. Serrels, Euan Ramsay, Paul A. Dalgarno, Brian D. Gerardot, John A. O'Connor, Robert H. Hadfield, Richard J. Warburton, and Derryck T. Reid, Solid immersion lens applications for nanophotonic devices, *Journal of Nanophotonics*, **2**, 021854 (2008).

[8] W. L. Barnes, G. Björk, J. M. Gérard, P. Jonsson, J. A. E. Wasey, P. T. Worthing, and V. Zwiller, Solid-state single photon sources: light collection strategies, *The European Physical Journal D*, **18**, 197 (2002).

[9] Valéry Zwiller, and Gunnar Björk, Improved light extraction from emitters in high refractive index materials using solid immersion lenses, *Journal of Applied Physics*, **92**, 660 (2002).

[10] A. N. Vamivakas, M. Atatüre, J. Dreiser, S. T. Yilmaz, A. Badolato, A. K. Swan, B. B. Goldberg, A. Imamoğlu, and M. S. Ünlü, Strong extinction of a far-field laser beam by a single quantum dot, *Nano Letters*, **7**, 2892 (2007).

[11] M. Born and E. Wolf, *Principles of Optics*, Cambridge University Press, (2002).

[12] Kerry J. Vahala, Optical microcavities, *Nature*, **424**, 839 (2003).

[13] Serkan Ateş, Luca Sapienza, Marcelo Davanço, Antonio Badolato, and Kartik Srinivasan, Bright single-photon emission from a quantum dot in a circular Bragg grating microcavity, *IEEE Journal of Selected Topics in Quantum Electronics*, **18**, 1711 (2012).

[14] M. Davanço, M. T. Rakher, D. Schuh, A. Badolato, and K. Srinivasan, A circular dielectric grating for vertical extraction of single quantum dot emission, *Applied Physics Letters*, **99**, 041102 (2011).

[15] Yong Ma, Peter E. Kremer, and Brian D. Gerardot, Efficient photon extraction from a quantum dot in a broad-band planar cavity antenna, *Journal of Applied Physics*, **115**, 023106 (2014).

[16] M. B. Ward, M. C. Dean, R. M. Stevenson, A. J. Bennett, D. J. P. Ellis, K. Cooper, I. Farrer, C. A. Nicoll, D. A. Ritchie, and A. J. Shields, Coherent dynamics of a telecom-wavelength entangled photon source, *Nature Communications*, **5**, 3316 (2014).

[17] Andres Castellanos-Gomez, Michele Buscema, Rianda Molenaar, Vibhor Singh, Laurens Janssen, Herre S J van der Zant, and Gary A Steele, Deterministic transfer of two-dimensional materials by all-dry viscoelastic stamping, *2D Materials*, **1**, 011002 (2014).

[18] User's manual *Toploading pulse tube system with 9 T magnet attoDRY 1000*, attocube systems AG, München Germany, (2013).

[19] User's manual *attocube systems' Nanopositioners*, attocube systems AG, München Germany, (2013).

[20] User's manual *Model 7265 DSP lock-in amplifier*, Ametek advanced measurement technology, Berwyn, PA, (2014).

[21] User's manual *Time-correlated single photon counting system and picosecond event timer with USB interface*, PicoQuant, Berlin, Germany, (2013).

[22] User's manual *Single photon counting module*, PerkinElmer Optoelectronics, Wiesbaden, Germany, (2007).

[23] S. Cova, M. Ghioni, A. Lotito, I. Rech, and F. Zappa, Evolution and prospects for single-photon avalanche diodes and quenching circuits, *Journal of Modern Optics,*, **51**, 1267 (2004).

[24] M. G. Tanner, C. M. Natarajan, V. K. Pottapenjara, J. A. O'Connor, R. J. Warburton, R. H. Hadfield, B. Baek, S. Nam, S. N. Dorenbos, E. Bermúdez Ureña, T. Zijlstra, T. M. Klapwijk, and V. Zwiller, Enhanced telecom wavelength single-photon detection with NbTiN superconducting nanowires on oxidized silicon, *Applied Physics Letters*, **96**, 221109 (2010).

[25] S. N. Dorenbos, E. M. Reiger, U. Perinetti, V. Zwiller, T. Zijlstra, and T. M. Klapwijk, Low noise superconducting single photon detectors on silicon, *Applied Physics Letters*, **93**, 131101 (2008).

[26] Patrick J. Clarke, Robert J. Collins, Philip A. Hiskett, María-José García-Martínez, Nils J. Krichel, Aongus McCarthy, Michael G. Tanner, John A. O'Connor, Chandra M. Natarajan, Shigehito Miki, Masahide Sasaki, Zhen Wang, Mikio Fujiwara, Ivan Rech, Massimo Ghioni, Angelo Gulinatti, Robert H. Hadfield, Paul D. Townsend, and Gerald S. Buller, Analysis of detector performance in a gigahertz clock rate quantum key distribution system, *New Journal of Physics*, **13**, 075008 (2011).

[27] User's manual *id220*, ID Quantique, Carouge-Genève, Switzerland, (2004).

[28] User's manual *Grating stabilized diode laser head designed for DLC pro*, Toptica Photonics, Munich, Germany, (2014).

[29] User's manual *Digital laser controller*, Toptica Photonics, Munich, Germany, (2014).

[30] User's manual *Tunable Littman/Metcalf external cavity diode laser*, Sacher Lasertechnik Group, Marburg, Germany, (2014).

[31] User's manual *Wavelength meter Ångstrom WS/7 IR*, HighFinesse, Tübingen, Germany, (2014).

Chapter 3

Characterization of telecommunication wavelength quantum dots in applied fields

The objective of this chapter is to characterize a group of quantum dots (QDs) that emit photons at telecom wavelengths in preparation for an attempt at obtaining resonance fluorescence from such QDs. Written partially based on Ref. [1], the chapter describes experiments on InAs/GaAs QDs emitting near the telecom O-band, including single dot spectroscopy in the presence of external electric and magnetic fields in both Faraday and Voigt geometries and time-resolved spectroscopy. We measure permanent dipole moments, polarizabilities, diamagnetic shifts, g-factors, as well as primary and secondary lifetimes of neutral excitons and lifetimes of the charged excitons. Using a perturbative Coulomb blockade model, the confinement energies, inter-particle Coulomb interaction energies and wavefunction extents of carriers are determined. The different morphology of telecom wavelength QDs is found to result in large single electron confinement energies, small electron-electron and electron-hole interaction energies, confirming that carriers are in the strong confinement regime. Due to the strong confinement, a relatively large tuning of the QD emission energy (5 to 7 meV) with an applied vertical electric field is observed.

The QD samples were placed into a cryostat at 4 K and probed by a continuous wave (cw) or pulsed laser at 830 nm. The microphotoluminescence (μ-PL) was analyzed either by a liquid nitrogen cooled grating spectrometer with a InGaAs linear array or a Superconducting Nanowire Single Photon Detector (SNSPD) at

2.8 K.

Two metal-insulator-semiconductor field-effect transistor (MISFET) QD samples were used for experiments described in this chapter. Sample VN2209A with a ZrO_3 super solid immersion lens (s-SIL) was used in the Faraday geometry experiment and for time-resolved measurements. It had a lever arm (see Section 2.1.4) coefficient of 27 (see Table 2.1, Chapter 2), the dots started to charge at approximately -7.5 V, and 20 counts/s on the 1200 grooves/mm grating of the spectrometer were normally registered from a single QD. For the Voigt geometry experiment sample VN2476E (see Table 2.2, Chapter 2) with a 1 mm diameter ZrO_3 hemispherical solid immersion lens (h-SIL) was used, the lever arm coefficient was 7, charging began at about -0.3 V, and 10 counts/s were normally registered on the 1200 grooves/mm grating of the spectrometer. Both structures emitted photons near $\lambda = 1300$ nm at T = 4 K, the spectral linewidth (about 0.08 nm at $\lambda = 1300$ nm) was limited by the spectrometer resolution. Coulomb blockade was observed for both MISFETs, enabling deterministic control of the charge state by varying the bias applied to the sample.

The main problem encountered when working with these samples was low emission intensity from individual QDs. This has two probable causes. First of all, efficiency of detection of photons at telecom wavelength is quite low compared to photons with wavelengths around 950 nm. The second possible cause is the collection efficiency of the sample. Some of the methods of improving collecting efficiency for further experiments are discussed in Section 2.1.5.

3.1 Photoluminescence maps and line assignment

The PL map in Fig. 3.1(a) is an example of PL spectra acquired as a function of voltage applied to the top gate of a MISFET device (see Fig. 2.2). The lines visible in the scan correspond to emission as a result of recombination from different states: neutral (X^0) and negatively charged (X^{1-} and X^{2-}) excitons. The Coulomb blockade effect is revealed in the change of the emission energy under varying voltage, which corresponds to the addition of extra electrons to the QD [2]. In the ideal case, the edges of exciton plateaus are sharply defined, and the voltage at which the X^0 plateau ends is the same as the voltage where X^{1-} plateau begins. In our samples, the Coulomb blockade effect is less pronounced (see Fig. 3.1(a)), and the plateaus

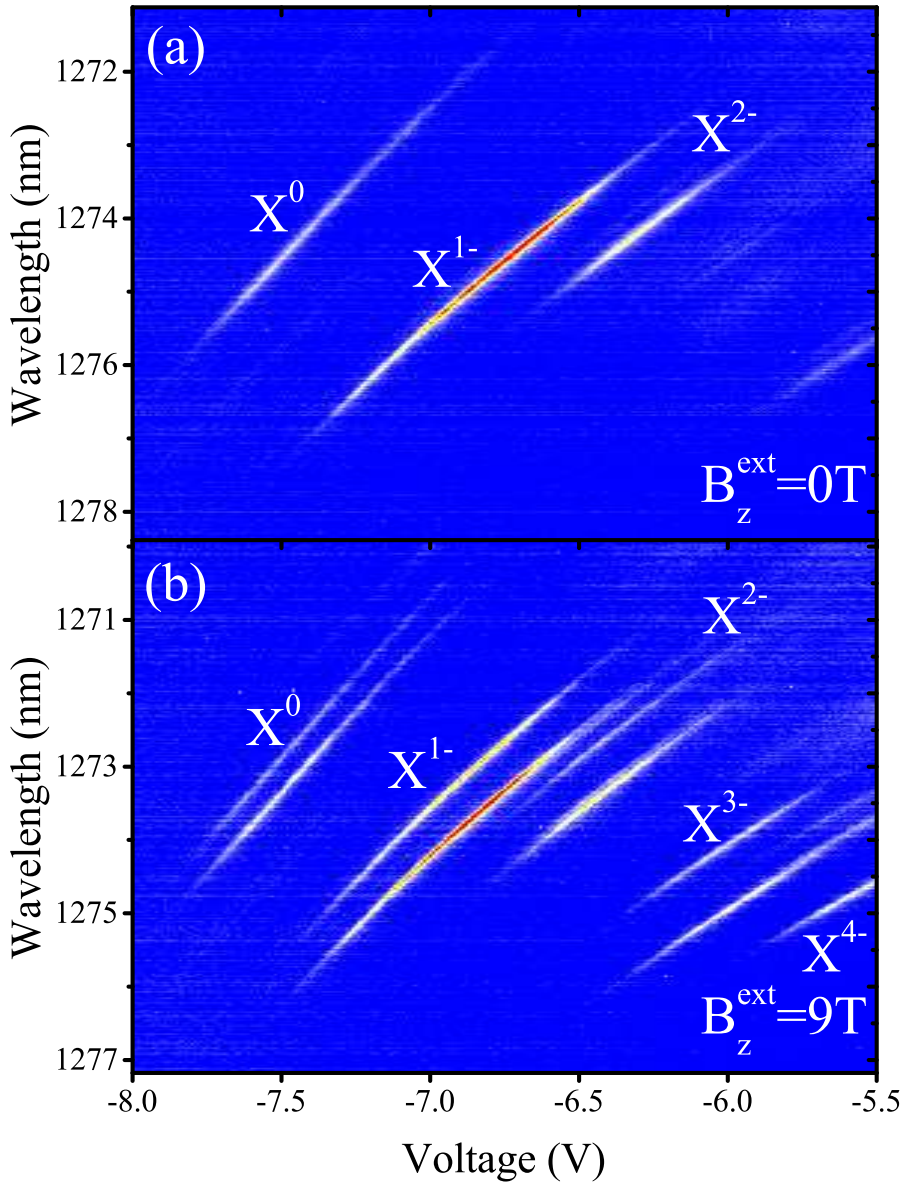

Figure 3.1: PL spectra from a single telecom wavelength QD, collected as a function of the applied gate voltage under cw excitation at a temperature T= 4 K. The external magnetic field B is applied along the quantum dot growth direction (Faraday configuration), and is 0 T in (a) and 9 T in (b). The lines corresponding to emission from different states of a single quantum dot are labeled accordingly.

representing emission from different exciton states of the same QD overlap. This is a result of the increasing tunneling time of electrons into the QD from the Fermi sea due to increased height of the tunneling barrier compared to that of similar structures emitting at $\lambda \approx 950$ nm [3]. In our samples the tunneling time becomes comparable to the exciton recombination time. In other words, the extra electron does not always manage to tunnel into the dot before decay occurs. As a result, at the edges of the plateau two charge states are simultaneously observed: with an additional electron and without it [4].

The neutral exciton line can be recognized by a distinctive fine structure splitting (FSS) visible on high resolution PL maps. The X^{1-} plateau is usually characterized by a large voltage extent, since an additional electron has to go to the p-state and needs to overcome not only the electron-electron Coulomb repulsion, but also the s-p-shell quantization energy. The X^{1-} plateau is also generally brighter than the other lines on the PL map. The biexciton can sometimes be seen on PL maps as a faint line at shorter wavelengths than the neutral exciton. Lines appearing at less negative biases on the PL map are assumed to be higher negatively charged states (X^{2-} and X^{3-}). Normally, the addition of an electron to a dot causes the PL signal to move to longer wavelengths.

3.2 Coulomb blockade model

A perturbation theory that explains the Coulomb interactions of carriers is formulated in Ref. [5]. Previously, the model has been successfully applied to single charge-tunable QD emitting around $\lambda = 950$ nm in Ref. [3] to explain the Coulomb interactions of carriers within. The model is based on the following assumptions [5]: firstly, the Coulomb interactions within the QD are considered perturbations, i.e. their energies are smaller than the confinement energies and the quantization energies of the electrons and holes; secondly, the QDs are seen as approximately two-dimensional structures to simplify calculations because their lateral extent is several times larger than their vertical extent and, therefore, vertical confinement of charge carriers is larger than the lateral confinement; thirdly, the confinement potentials are considered parabolic; finally, interactions between separate QDs are considered negligible because the distance between two dots (several hundreds of nanometers) is much larger than the distance between a given QD and the back contact (typ-

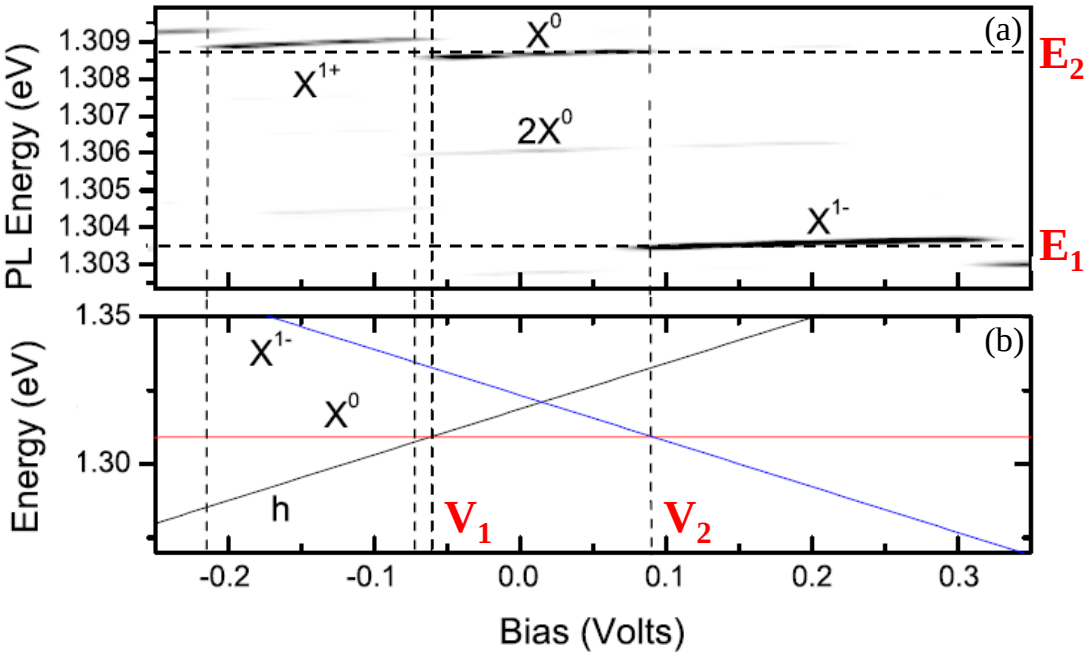

Figure 3.2: (a) PL spectra as a function of applied bias collected from a QD from a charge-tunable sample. The neutral exciton (X^0), the negatively charged exciton (X^{1-}), the positively charged exciton (X^{1+}), and the biexciton ($2X^0$) states are labeled. (b) The Coulomb blockade model applied to the quantum dot in (a). At biases more negative than -0.06 V a hole-only state has the minimum possible energy and is energetically favorable; at -0.06 V the neutral exciton state becomes energetically favorable, and at bias 0.09 V the singly charged exciton state is energetically favorable. Figure is adapted from Ref. [3].

ical tunnel barrier thickness $t \approx 10 - 20$ nm). To apply the Coulomb blockade model, it is necessary to write an asymmetric wave function for electrons or holes. The Coulomb interactions are written as first order perturbations, which are then calculated analytically.

Applying the model to a particular configuration involves the following steps [6]. First, the difference in PL energy between the neutral exciton line (E_2) and the singly charged exciton line (E_1), as well as the voltage extent of the neutral exciton plateau are determined from a PL map (see Fig. 3.2):

$$\Delta E = E_2 - E_1; \tag{1}$$

$$\Delta V = V_2 - V_1. \tag{2}$$

In order for an electron to tunnel into a QD from the back contact, it has to overcome the potential of the tunnel barrier and lose the confinement energy, so the energy of a single electron in the s-shell of a QD is a function of the applied bias V_g and can be written as

$$E(e) = (V_0 - V_g)\lambda^{-1} - E_c - E_i; \tag{3}$$

where V_0 is the the Schottky barrier (see Section 2.1.3) height ($V_0 = 0.6$ V is typical), λ is the lever arm of device given by the relation of the distance between the Schottky contact and the back gate to the tunnel barrier thickness, and E_i is the interaction energy of the electron with the image charge in the back contact given by the following relation:

$$E_i = \frac{q^2}{16\pi\epsilon_0\epsilon_r t}; \tag{4}$$

where $\epsilon_0 = 8.85\times10^{-12}$ F/m is the vacuum permittivity, ϵ_r is the relative permittivity of the semiconductor material, and t is the distance between the dot layer and the back contact (tunnel barrier thickness).

In a similar manner the energy of the two electrons in the s-shell in a QD can be calculated. The terms in Eq. 3 are doubled since two electrons are present, the interaction with the image charge increases to $4E_i$, and finally the term E_{ee}^{ss} is added to take into account the interaction energy of the two electrons in the s-shell:

$$\begin{aligned} E(2e) &= 2E(e) + E_{ee}^{ss} + 2E_i - 4E_i \Rightarrow \\ E(2e) &= 2(V_0 - V_g)\lambda^{-1} - 2E_c + E_{ee}^{ss} - 4E_i. \end{aligned} \tag{5}$$

The energy of a neutral exciton in a QD is given by the following:

$$E(X^0) = E_0 - E_{eh}^{ss}; \tag{6}$$

where E_0 is the energy separation between the empty electron s-shell and empty hole s-shell.

The energy of the singly-charged exciton can be found by adding the energy of an extra electron to the energy of a neutral exciton and taking into account all the additional carrier interactions that result:

$$\begin{aligned} &E(X^{1-}) = E(X^0) + E(e) + E_{ee}^{ss} - E_{eh}^{ss} \Rightarrow \\ &E(X^{1-}) = E_0 + (V_0 - V_g)\lambda^{-1} - E_c + E_{ee}^{ss} - 2E_{eh}^{ss} - E_i. \end{aligned} \tag{7}$$

Likewise, the energy of a single hole in the s-shell of the QD can be found by subtracting the energy of an electron from the energy of the neutral exciton and is given by:

$$\begin{aligned} &E(h) = E(X^0) - E(e) + E_{eh}^{ss} \Rightarrow \\ &E(h) = E_0 - (V_0 - V_g)\lambda^{-1} + E_c - E_i. \end{aligned} \tag{8}$$

In addition, the following relations are useful: at V_2 (see Fig. 3.2(b)) $E(X^0) = E(X^{1-})$:

$$(V_0 - V_2)\lambda^{-1} = E_c - E_{ee}^{ss} + E_{eh}^{ss} + E_i; \tag{9}$$

and at V_1 (see Fig. 3.2(b)) $E(h) = E(X^0)$:

$$(V_0 - V_1)\lambda^{-1} = E_c + E_{eh}^{ss} - E_i. \tag{10}$$

From Eqs 9, 10 the following relation can be extracted:

$$(V_2 - V_1)\lambda^{-1} = E_{ee}^{ss} - 2E_i. \tag{11}$$

In addition considering the initial and final states of the charged and neutral excitons, the following can be obtained:

$$E_1 = E_{initial}^{X^{1-}} - E_{final}^{X^{1-}} = E(X^{1-}) - E(e) = E_0 + E_{ee}^{ss} - 2E_{eh}^{ss}; \tag{12}$$

$$E_2 = E_{initial}^{X^0} - E_{final}^{X^0} = E(X^0) - 0 = E(X^0). \tag{13}$$

From Eqs 12, 13 the following relation can be written:

$$\Delta E = E_2 - E_1 = E_{ee}^{ss} - E_{eh}^{ss}. \tag{14}$$

Using the above equations E_{ee}^{ss}, E_{eh}^{ss}, and E_c can be easily calculated for a given QD. First E_{ee}^{ss} is calculated from Eq. 11. Then E_{eh}^{ss} is calculated from Eq. 14. Finally, E_0 is calculated from Eq. 6, and by substituting it into Eq. 10, E_c can be extracted. Other parameters such as E_v can be extracted in a similar manner.

The extent of the electron and hole wavefunctions (l_e and l_h, respectively) can be calculated using the direct Coulomb energies given by the model [6]:

$$E_{ee}^{ss} = \frac{e^2}{4\pi\epsilon_0\epsilon_r}\frac{\sqrt{\pi/2}}{l_e}; \tag{15}$$

$$E_{eh}^{ss} = \frac{e^2\sqrt{\pi}}{4\pi\epsilon_0\epsilon_r}\frac{1}{(l_e^2+l_h^2)^{1/2}}. \tag{16}$$

In this work the Coulomb blockade model was used to calculate the electron-electron (electron-hole) interaction and the electron (hole) confinement energies, as well as the effective lengths of the electron (hole) wavefunction (see Fig. 3.3) for several QDs emitting in the telecom wavelength region. As the observed interaction energies are much smaller than the confinement energies, they can be considered perturbations, and the trapped carriers can be said to be in the strong confinement regime. This is further supported by transmission electron microscopy (TEM) images of telecom wavelength QDs (see Fig. 2.1(a)). In comparison with QDs emitting around the $\lambda = 950$ nm region (see Fig. 2.1(b)), these dots appear taller, and, assuming identical composition, their confinement in the vertical direction can be expected to be deeper. Strong confinement leads to larger effective lengths of the electron and hole wavefunctions compared to QDs emitting around 950 nm.

The effective lengths of the wavefunction and confinement energies were found to be about a factor of two larger and carrier-carrier interaction energies about a factor of two smaller compared to QD emitting around 950 nm [3, 7], which is expected of QDs with a larger physical size.

3.3 Electric field dependence

While the transition energy of QDs emitting near $\lambda = 950$ nm can be tuned by just 1 meV [7], the telecom wavelength dots studied in this work are tunable by about 5 to 7 meV. This is believed to be a consequence of larger electron and hole confinement energies found in these dots. Carriers in telecom QDs can withstand larger electric fields before tunneling out due to the strong confinement, despite their

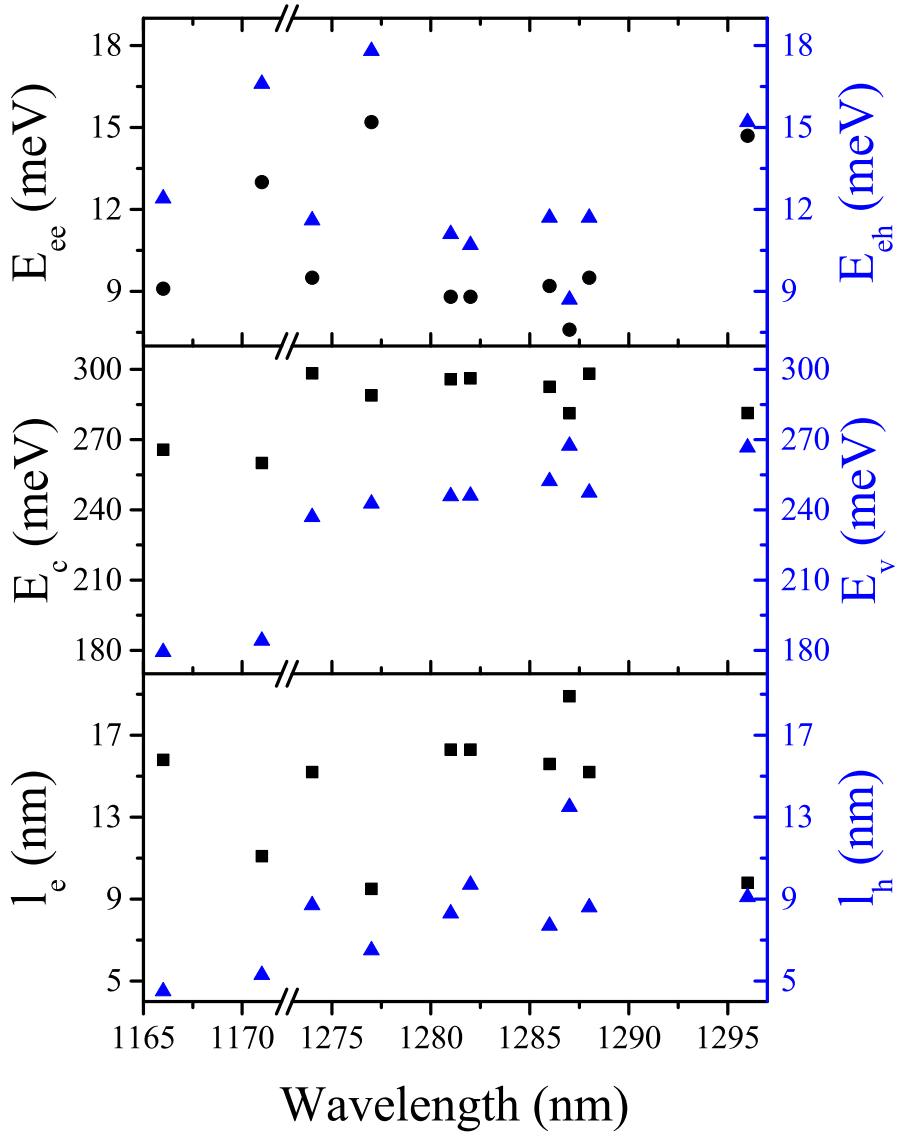

Figure 3.3: Application of the Coulomb blockade model to a series of QD emitting at telecom wavelengths to extract electron-electron and electron-hole interaction energies (E_{ee} and E_{eh}, respectively), the electron and hole confinement energies (E_c and E_v, respectively), and the electron and hole wavefunction extent (l_e and l_h, respectively). The x-axis shows the wavelength of the middle of the neutral exciton plateau as seen on the PL map.

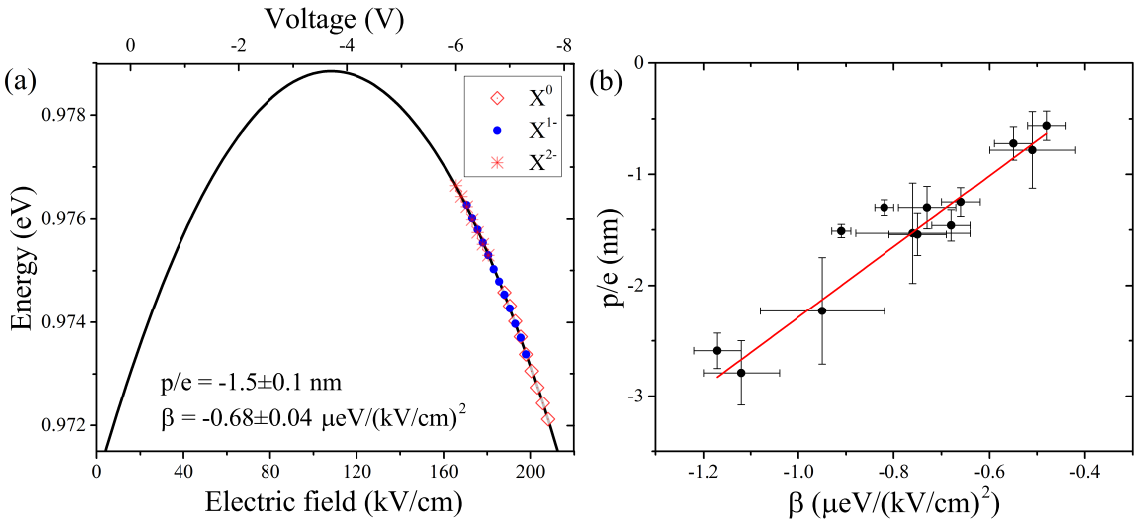

Figure 3.4: (a) Emission energy of different states of a single telecom wavelength QD as a function of applied electric field, the solid line is a quadratic fit to the data. The QD emission can be tuned by about 5 meV by changing the bias applied to the top gate. (b) The permanent dipole moment p/e against the polarizability β for a series of QDs emitting in the telecom O-band. The solid red line is a linear fit with slope 3.2 ± 0.2 nm/(μeV/(kV/cm)^2), and the error bars are obtained from errors in the parabolic fits in (a).

permanent dipole moments and polarizabilities being not significantly different from those of shorter wavelength quantum dots. This effect is particularly important for tuning the fine structure splitting of neutral excitons to zero by applying an external electric field in order to create sources of entangled photon pairs [8].

Exciton transition energies experience a Stark shift with applied bias V_g [7]:

$$E_{PL} = E_0 - pF + \beta F^2; \tag{17}$$

where the electric field F is a function of the Schottky barrier height (V_0) and the distance between the back gate and sample surface (d) (see Fig. 2.2):

$$F = -(V_g - V_0)/d. \tag{18}$$

For our MISFET device $V_0 = 0.6$ V and $d = 400$ nm. Exciton lines are fit with quadratic functions given in Eq. 17 and the permanent dipole moment (p/e, where e is the elementary charge), and the polarizability (β) are extracted from the fits (see Fig. 3.4(a)).

Large permanent dipole moments are observed, with p/e values ranging from -0.5 to -3.0 nm, similar to that of analogous QDs emitting around $\lambda = 950$ nm (0 to -3.0 nm) [7]. This indicates that laterally, the electron and hole wavefunctions are centered within the QD. The negative sign of the electron-hole separation value indicates that the hole is confined near the base of the dot, and the electron wavefunction, given its lighter effective mass, is delocalized over the dot [7, 9]. Positive dipole moments for QDs have been reported, and are related to an increase of the concentration of In atoms going from the bottom to the apex of the QD [9]. The polarizability and the permanent dipole moment are linearly related due to a constant built-in electric field of the device (see Fig. 3.4(b)), similar to what was reported for $\lambda = 950$ nm [7]. The observed polarizabilities (-0.5 to -1.2 μeV/(kV/cm)^2) are slightly smaller than reported in Ref. [7] for QDs emitting around $\lambda = 950$ nm (0 to -3 μeV/(kV/cm)^2), which can be explained by stronger confinement of carriers of telecom wavelength dots resulting in electrons and holes being more resistant to external fields.

3.4 Magneto-optics of telecom wavelength QDs

An external magnetic field B applied to a QD affects its exciton transition energies in two ways: first of all, the emission lines split due to the Zeeman effect; and second, the average of the emission energy from all the transitions shifts with increasing magnetic field, which is referred to as the diamagnetic shift. Two configurations of applying a magnetic field to a QD sample are possible: in the Faraday configuration the magnetic field is applied parallel to the growth direction of the sample wafer and in the Voigt configuration the magnetic field is applied orthogonal to the growth direction.

To gain further insight into the wavefunctions of telecom wavelength QDs magnetic fields up to 9 T were applied to the samples in both the Faraday and Voigt configurations. The diamagnetic shift of excition transition energies is related to the confinement of carriers within a QD, which is expected to be significantly different in the lateral and vertical directions due to the unique morphology of the telecom wavelength QDs.

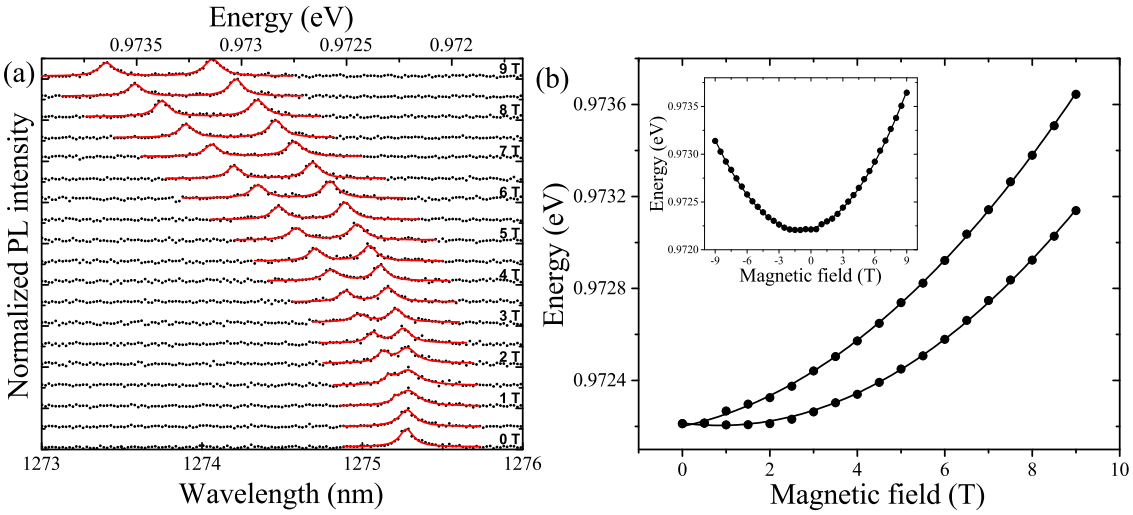

Figure 3.5: (a) Normalized PL spectra (shifted for clarity) of a negatively charged exciton state under non-resonant (830 nm) excitation for magnetic fields ranging from 0 T to 9 T (with 0.5 T increments) applied in the Faraday configuration. Solid lines are Lorentzian fits to the data. (b) Position of the Lorentzian fit peaks from (a), plotted as a function of the applied magnetic field. The solid lines are parabolic fits to the data. The insert shows the data with the lower energy branch reflected over the $B = 0$ T axis with a quadratic fit, allowing the extraction of the diamagnetic coefficient value.

3.4.1 Diamagnetic shift

First the diamagnetic shift of exciton lines under the effect of a magnetic field applied in the growth direction of the QD sample (Faraday configuration) are considered. Fig. 3.5(a) shows a typical example of PL spectra collected from a negatively charged exciton at different magnetic fields. In the presence of an external magnetic field the energy of the emission lines experiences a diamagnetic shift α, described by the expression $E = \alpha B^2$. The PL spectra for each state was fit with one or, where possible (at higher magnetic fields), two Lorentzian functions, and the position of the Lorentzian fit peaks at different magnetic fields was plotted on one graph (see Fig. 3.5(b)). The diamagnetic shift was calculated by reflecting the low energy branch in Fig. 3.5(b) over the $B = 0$ T axis and fitting the resultant data points with a parabola (see insert in Fig. 3.5(b)). Table 3.1 gives the values of the diamagnetic shifts obtained from individual quantum dots.

The values of the diamagnetic shifts reveal information about the exciton binding

Table 3.1: Diamagnetic shifts (α), exciton g-factors ($|g|$), and electron (g_h) and hole (g_e) g-factors of several telecom wavelength QDs measured in external magnetic fields applied in Faraday and Voigt configurations. λ_{X^0} corresponds to the emission wavelength of the neutral exciton line in the middle of the emission tuning range.

Faraday configuration				
λ_{X^0} (nm)	Excitonic state	$\|g\|$		α (μeV/T^2)
1274	X^0	0.73 ± 0.02		13.48 ± 0.09
	X^{1-}	0.63 ± 0.01		14.83 ± 0.07
1281	X^0	0.77 ± 0.01		17.01 ± 0.20
	X^{1-}	0.89 ± 0.01		18.20 ± 0.31
1282	X^0	0.36 ± 0.02		14.25 ± 0.09
	X^{1-}	0.98 ± 0.01		14.72 ± 0.04
Voigt configuration				
λ_{X^0} (nm)	Excitonic state	g_h	g_e	α (μeV/T^2)
1290	X^0	-0.17 ± 0.01	-0.77 ± 0.01	2.15 ± 0.12
	X^{1-}	-0.49 ± 0.06	-0.91 ± 0.07	5.30 ± 0.47
1292	X^{1-}	-0.24 ± 0.01	-1.04 ± 0.01	2.50 ± 0.05
1300	X^0	-0.21 ± 0.02	-0.87 ± 0.04	0.93 ± 0.30
	X^{1-}	-0.36 ± 0.02	-0.80 ± 0.03	1.83 ± 0.26
1310	X^{1-}	-0.26 ± 0.04	-0.89 ± 0.04	1.82 ± 0.19
1317	X^{1-}	-0.19 ± 0.05	-0.72 ± 0.03	0.63 ± 0.14

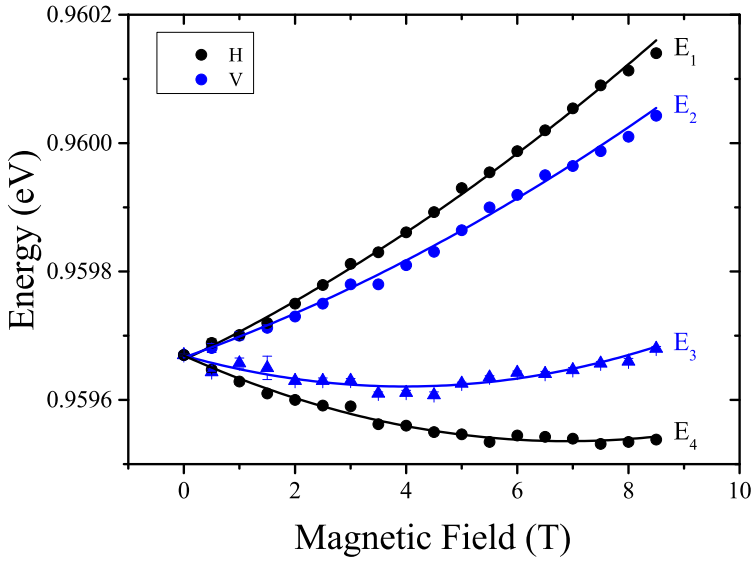

Figure 3.6: Peak position of the Lorentzian fits to the spectra of a negatively charged exciton state under non-resonant (830 nm) excitation for magnetic fields ranging from 0 T to 8.5 T (with 0.5 T increments) applied in the Voigt configuration, plotted as a function of the applied magnetic field. The solid lines are parabolic fits to the data. Black (blue) dots and curves represent horizontally (vertically) polarized emission.

and confinement energies. The telecom wavelength QDs under study show a small (about 10%) increase of the value of α upon the addition of an extra electron to a neutral exciton. From literature it is known that the value of α is expected to reduce by a factor of 2 between the neutral exciton and the charged exciton in the case of weak confinement [10] due to more consistent electron-electron interaction. The fact that an increase rather than a decrease in the value of the diamagnetic shift is observed further supports the conclusion that the QDs under study are strongly confined.

In Ref. [11], the diamagnetic shifts for the exciton, bi-exciton and positively charged exciton of small InAs quantum dots are studied. The diamagnetic shifts were found to be different for the states under study when the confined electron and hole wave functions exhibited a large difference in their lateral extents. It was proposed that the above is only the case for smaller quantum dots. However, in the larger InAs quantum dots under study we also observe rather large differences between the electron and the hole wavefunction (see Fig. 3.3). We attribute this to the carriers being in the strong confinement regime, despite the larger size of the

quantum dots and their different morphology.

Next, let us consider the diamagnetic shift of exciton lines upon applying the external magnetic field orthogonal to the quantum dot sample wafer growth direction (Voigt configuration). Applying an external field in the Voigt configuration results in the breaking of the rotational symmetry of the wavefunctions, and the mixing of what were originally bright and dark exciton states, with all the states becoming visible in the PL spectra [12, 13].

Fig. 3.6 shows the peak position of the Lorentzian fits to the spectra of a negatively charged exciton under non-resonant excitation for magnetic fields ranging from 0 T to 8.5 T applied in the Voigt configuration, plotted as a function of the applied magnetic field. The solid lines are parabolic fits to the data. Different colors of the data points and fits represent different polarizations of the collected light. The diamagnetic shifts are calculated by reflecting the two low energy branches over the $B = 0$ T axis and fitting the data points having the same polarization with a quadratic function.

According to Ref. [14], for QDs emitting around 950 nm upon switching the magnetic field from the Faraday to the Voigt configuration the diamagnetic coefficient values change by up to a factor of 3. It was found that for telecom wavelength QDs in the Voigt configuration the value of the diamagnetic shift is one order of magnitude smaller compared to the same value obtained in the Faraday configuration (see Table 3.1). This is most likely due to a larger height-to-diameter ratio in telecom wavelength quantum dots, which indicates that the vertical z confinement in the quantum dot determines the binding energies of the carriers.

3.4.2 Excitons in a magnetic field

To determine the evolution of exciton emission energy upon the application of a magnetic field to a QD, the authors in Ref. [13] consider the spin Hamiltonian of the system H^{tot}. The total system Hamiltonian consists of two parts: the exchange Hamiltonian H_{ex} and the Hamiltonian that describes the interaction of the excitons with a magnetic field H_F or H_V for fields applied in the Faraday and Voigt configurations, respectively.

A neutral exciton contains an electron and a hole, which can have possible spin values $S_e = \pm 1/2$ and $S_h = \pm 3/2$, respectively. In sum, four exciton configurations

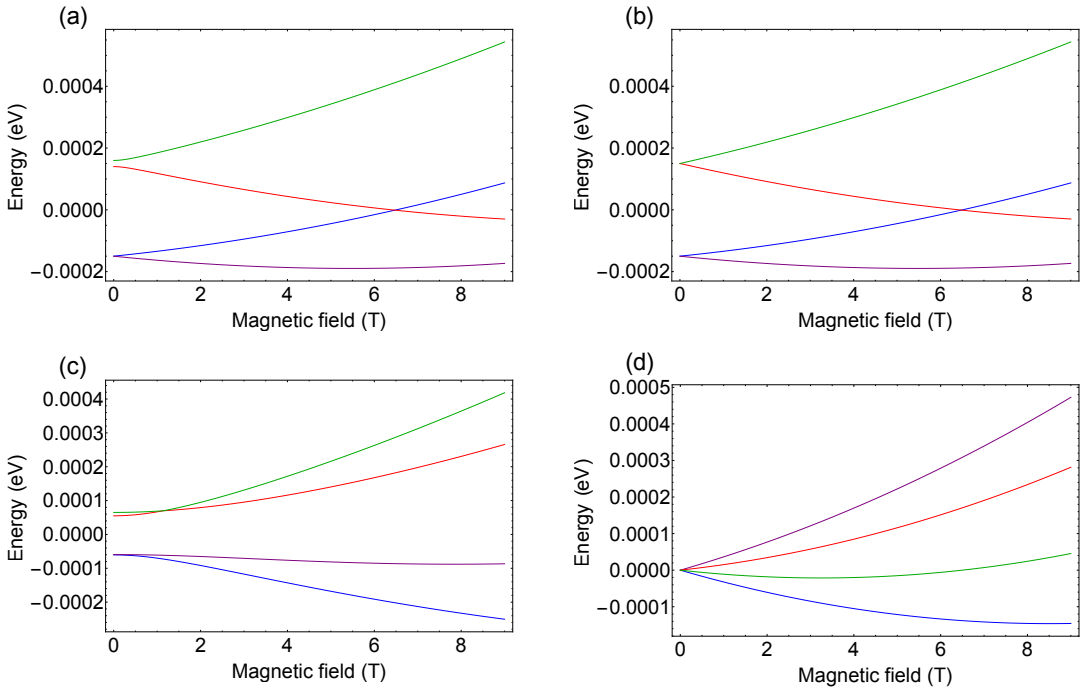

Figure 3.7: The relative transition energies plotted against the magnetic field of excitons calculated using the spin Hamiltonian from Ref. [13], taking into account the diamagnetic shift, and using the typical parameters (δ_0 = 100 μeV, δ_1 = 10 μeV, δ_2 = 1 μeV) of QDs under study which emit at λ = 1300 nm. The figure shows (a) neutral and (b) negatively charged excitons in the Faraday geometry, and (c) neutral and (d) negatively charged excitons in the Voigt configuration.

can be formed, two bright states with orbital angular momentum $L_z = \pm 1$ that are radiative and two dark states with orbital angular momentum $L_z = \pm 2$ that do not couple to the light field [7].

The exchange Hamiltonian accounts for the electron-hole exchange interaction and for neutral excitons is given by the following:

$$H_{ex} = \begin{bmatrix} \delta_0 & \delta_1 & 0 & 0 \\ \delta_1 & \delta_0 & 0 & 0 \\ 0 & 0 & -\delta_0 & \delta_2 \\ 0 & 0 & \delta_2 & -\delta_0 \end{bmatrix}. \tag{19}$$

Here δ_0 is the electron-hole exchange interaction, δ_1 is the fine-structure splitting (FSS) of the bright exciton, and δ_2 is the energy splitting between the two dark states, where $\delta_1, \delta_2 << \delta_0$. The matrix has a block diagonal form, which means that the dark and bright states do not mix (hybridize) with each other, and emission

from the dark state is not possible. However, the two dark states are always mixed together, and breaking of rotational symmetry leads to $\delta_1 \neq 0$ and the mixing of the bright states.

The second part of the spin Hamiltonian is determined by the interaction of the electron and hole spins with the magnetic field. In the Faraday configuration, where the magnetic field B is applied parallel to the QD growth direction, it is given by the following expression:

$$H_F = \frac{\mu_B B}{2} \begin{bmatrix} g_e + g_h & 0 & 0 & 0 \\ 0 & -g_e - g_h & 0 & 0 \\ 0 & 0 & -g_e + g_h & 0 \\ 0 & 0 & 0 & g_e - g_h \end{bmatrix}; \tag{20}$$

where $\mu_B = 5.7 \times 10^{-5}$ eV/T is the Bohr magneton, and g_e and g_h are the electron and hole g-factors, respectively. The diagonal form of the matrix is a consequence of rotational symmetry of the Hamiltonian around the QD growth direction. No hybridization between the dark and the bright states occurs.

For a neutral exciton in a QD with a magnetic field applied orthogonal to the growth direction (Voigt configuration) the second part of the spin Hamiltonian is given by the following:

$$H_V = \frac{\mu_B B}{2} \begin{bmatrix} 0 & 0 & g_e & g_h \\ 0 & 0 & g_h & g_e \\ g_e & g_h & 0 & 0 \\ g_h & g_e & 0 & 0 \end{bmatrix}. \tag{21}$$

The presence of off-diagonal elements implies the loss of rotational symmetry and the mixing of the bright and dark states, which results in the dark states becoming visible.

A charged exciton contains two electrons with opposite spins, which form a singlet state, and a hole, resulting in no exchange interaction. The Hamiltonians for the charged exciton are similar to the above, with the FSS value $\delta_1 = 0$.

The eigenvalues of the total Hamiltonian $H_F^{tot}(b) = H_{ex} + H_F(B)$ (Faraday geometry) and $H_V^{tot}(b) = H_{ex} + H_V(B)$ (Voigt geometry) characterize the energy levels of the system in a magnetic field B. The dependencies of transitions energies on magnetic field are shown in Fig. 3.7.

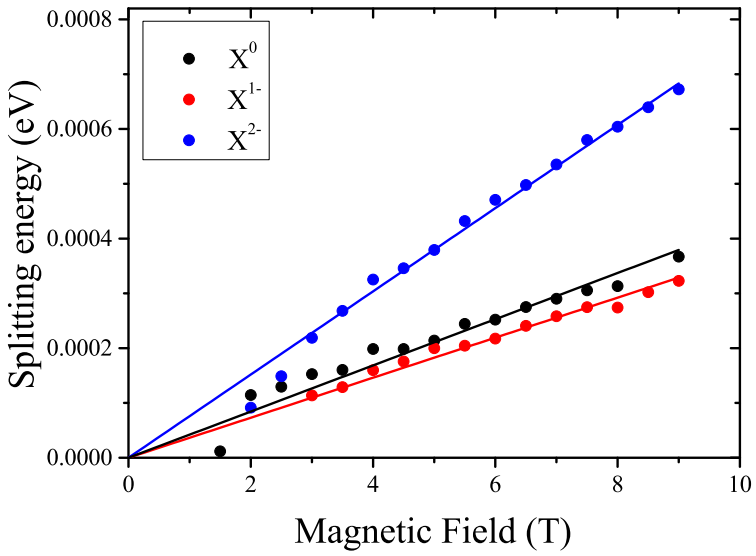

Figure 3.8: Zeeman splitting of the neutral exciton (black dots) and the negatively charged excitons (red and blue dots) of a telecom-wavelength QD in external magnetic fields from 0 T to 9 T applied in the Faraday geometry. The solid lines are linear fits.

3.4.3 Zeeman splitting and g-factors

Fig. 3.1 shows a typical example of PL spectra collected at a field of 0 T and 9 T as a function of voltage applied to the telecom QD MISFET in the Faraday configuration, making the splitting at applied magnetic fields clearly apparent.

The magnitude of the splitting is approximated by $\Delta E = g\mu_B B$, where μ_B is the Bohr magneton and g is the Landé factor. The measured Zeeman splittings are between about 10 and 40 μeV/T. These values are considerably smaller compared to those of QDs emitting around 950 nm, which were measured to be around 120 ± 30 eV/T [10]. This can be explained by theoretical calculations which show that an increase in the quantum dot size corresponds to a reduction of the g-factor [15]. The splitting was found to be a linear function of the magnetic field (see Fig. 3.8).

In the Voigt configuration the rotational symmetry of the wavefunctions is broken, and the emission from dark excitons becomes visible (diagonal transitions in Fig. 3.9(a)). The single quantum dot exciton lines split into 4 separate contributions labeled E_1, E_2, E_3, E_4 in Fig. 3.9(a). The s-shell electron and hole g-factors ($g_{e,h}$) can be determined from the energies of the excitons. From Fig. 3.9(a) we have:

$$E_z^e = g_e \mu_B B = E_1 - E_3 = E_2 - E_4; \tag{22}$$

$$E_z^h = g_h \mu_B B = E_1 - E_2 = E_3 - E_4; \tag{23}$$

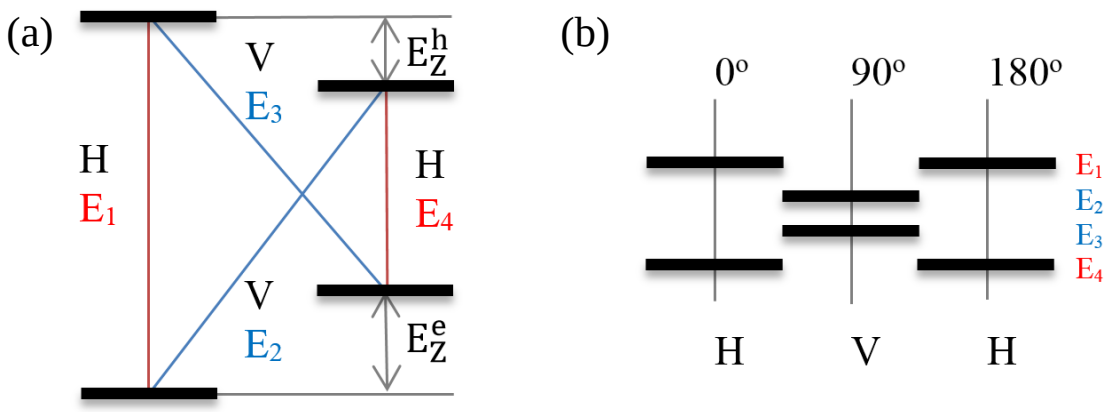

Figure 3.9: (a) A schematic showing the energy levels of a negatively charged exciton (X^{1-}) in an external magnetic field oriented in the Voigt geometry. In the Faraday geometry only the vertical transitions are bright (E_1 and E_4). Due to symmetry breaking in the Voigt configuration, four transitions can be observed (E_1, E_2, E_3, and E_4). The emission is linearly polarized and labeled H and V. (b) A schematic of the expected evolution of the signal from a QD in an external magnetic field in the Voigt geometry when rotating a half-wave plate in the collection arm of the microscope head. The angles correspond to the rotation angle of the half-wave plate.

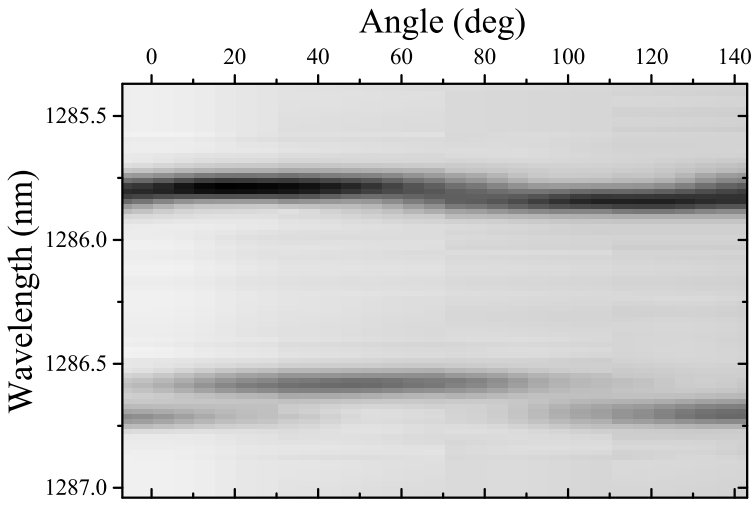

Figure 3.10: Spectra collected from a QD under non-resonant excitation (830 nm) at an external magnetic field (9 T) applied in the Voigt geometry plotted as a function of the half-wave plate angle in the collection arm of the microscope head.

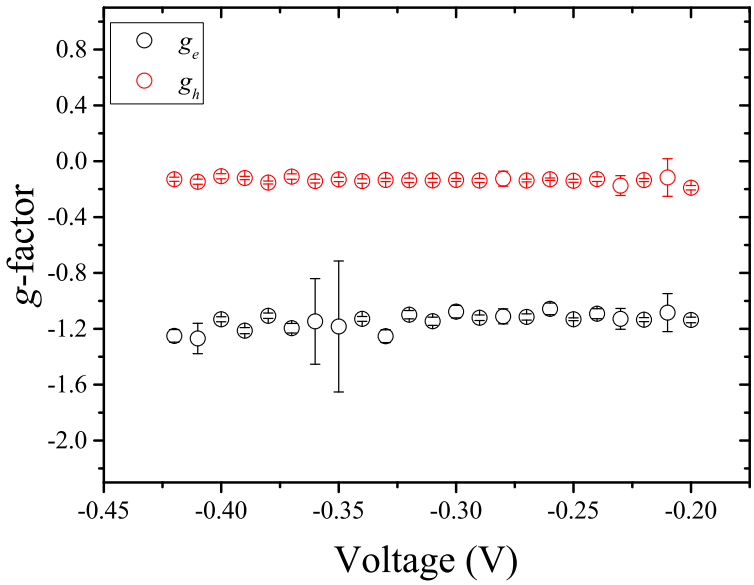

Figure 3.11: The electron (black circles) and hole (red circles) g-factors of a telecom wavelength QD versus gate bias under non-resonant excitation (830 nm) measured in a magnetic field (9 T) applied in the Voigt geometry.

where μ_B is the Bohr magneton [13]. The extracted values are given in Table I. An increase of the g-factor value going from a neutral exciton to a negatively charged exciton is observed, in agreement with Ref. [13]. The hole g-factors were found to be two to four times smaller than the electron g-factors. The slight fluctuations in the g-factor values measured for different quantum dots is attributed to the dependence of the g-factor on the quantum dot shape [16], which cannot be strictly controlled in the QD growth process.

The four transitions in Fig. 3.6 are linearly polarized with one pair being orthogonal to the other. Fig. 3.10 shows the spectra collected from a QD at 9 T as a function of the angle of a Meadowlark Optics liquid crystal variable retarder (see Section 2.2.10), acting as a half-wave plate, in the collection arm of the microscope head. As expected (see Fig. 3.9(b)), two of the four lines disappear when rotating the half-wave plate by 90°.

Finally, unlike what was reported in Ref. [17,18], a noticeable dependence of hole g-factors on applied bias was not observed (see Fig. 3.11). We expected the electron g-factor to have a weak dependence on the electric field due to the abundance of bound hole states that compensate the orbital angular momentum quenching that is induced by the electric field, while no such compensation occurs for the hole g-factor

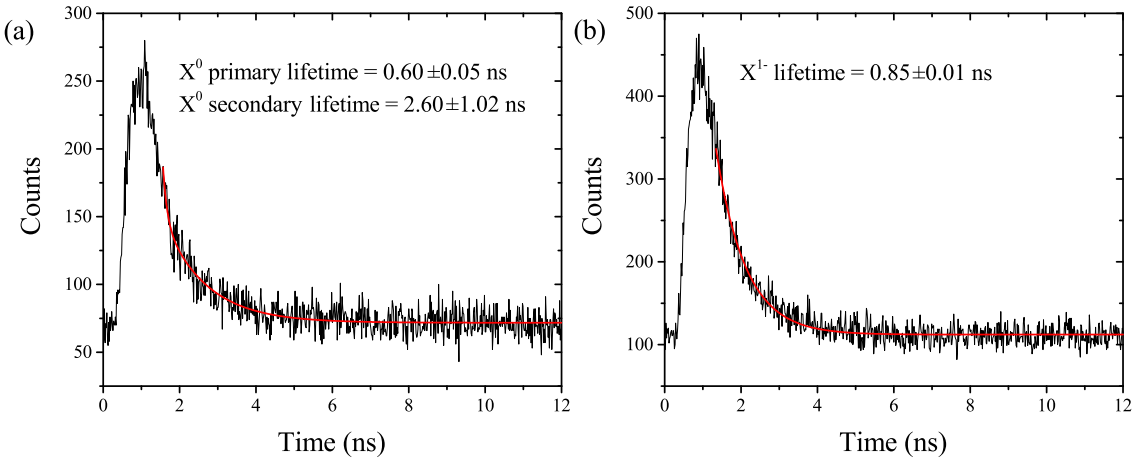

Figure 3.12: Photoluminescence decay curves of the neutral exciton (a) with a bi-exponential curve fit and a negatively charged exciton (b) with a single exponent fit measured under non-resonant excitation (830 nm).

due to the shortage of bound electron states [18]. For now the reason for this is not understood.

3.5 Lifetimes

A neutral exciton unaffected by a magnetic field has a total of possible four states: two states with an orbital angular momentum $L_z = \pm 1$ that is coupled to the light field (bright excitons) and two states with an orbital angular momentum $L_z = \pm 2$ that cannot directly couple to the light field (dark excitons) [19]. However, an electron spin-flip process that enables controlled conversion of dark excitons into bright ones for QDs emitting in the λ =900 nm range is reported in Ref. [20]. The authors introduce two independent processes that may be responsible for the spin flips. In the first case, the spin flip occurs as a result of an electron tunneling out of the dot containing a dark exciton and an electron with the opposite spin replacing it, creating a bright exciton (process A). In the second case, an additional electron with spin-up (-down) tunnels into a dot that contains a dark neutral exciton, creating a charged exciton, followed by the original election with spin-down (-up) leaving the dot, creating a bright neutral exciton (process B). Therefore the neutral exciton is characterized by two lifetimes: the fast component is the decay of the bright exciton, and the slow component is the result of the electron spin-flip process via an exchange with the Fermi sea and subsequent radiative decay.

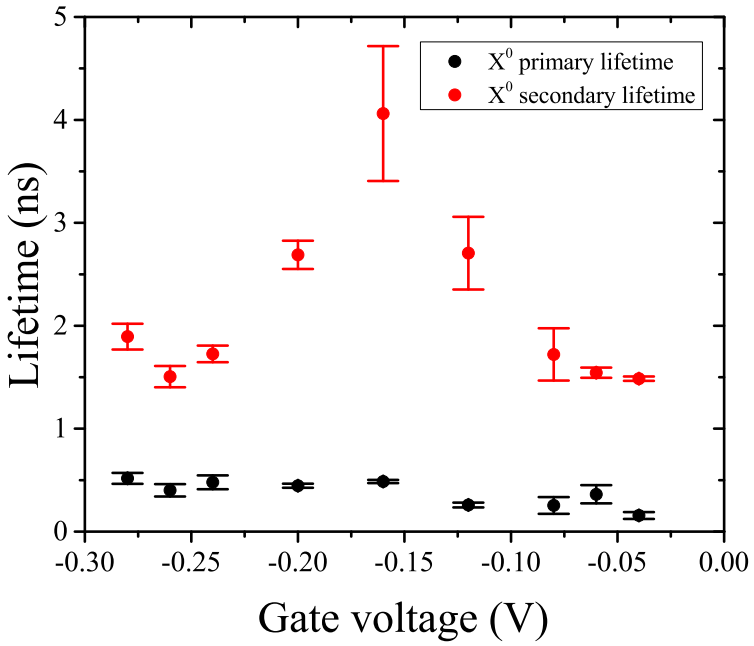

Figure 3.13: The primary (black dots) and secondary (red dots) lifetimes of a neutral exciton in a telecom wavelength QD under non-resonant excitation (830 nm) as a function of voltage applied to the top gate of a MISFET device. The error bars represent the errors in the exponential fits of the raw data.

The lifetimes of different exciton states of QDs emitting around λ =1300 nm are measured. In general, primary exciton lifetimes are around 300 to 600 ps, and slow decay times are around 1 to 4 ns (see Fig. 3.12(a)), which is significantly longer than previously reported for QDs emitting around λ=950 nm [20]. The lifetime of the negatively charged excitons was found to be in the 0.8 to 1.4 ns range (see Fig. 3.12(b)). The slow component of neutral exciton decay, and with it, the spin-flip rate, was found to be dependent on bias, while the fast component remained consistent at a range of biases. Slower dark exciton lifetimes are observed near the center of the plateau, and faster lifetimes are measured near the edges (see Fig. 3.13), which is in agreement with data from λ =950 nm QDs [20]. The spin-flip processes appear to be most effective on the edges of the neutral exciton plateau due to a direct coupling to the Fermi sea. Model calculations reported in Ref. [20] confirm that process A dominates on the low-bias side of the plateau and the process B, on the high-bias side.

The negatively charged exciton has a considerably longer lifetime than the neutral exciton. It appears that in a negatively charged exciton containing two electrons

and hole, the wavefunctions of the two electrons repel each other and, as a consequence, have less overlap with the hole wavefunction, which results in slower decay. In the case of the neutral exciton with just one electron-hole pair, the electron and the hole wavefunctions have a bigger overlap, and, accordingly, the exciton decay is more efficient than the decay of the charged exciton.

The lifetime of excitons is related to the confinement of electrons and holes within the QD. In general, the stronger confinement of telecom wavelength QDs was found to lead to an increase of exciton lifetimes compared to similar QDs emitting around 950 nm.

3.6 Discussion and further directions

In summary, by carrying out measurements on single self-assembled dot-in-a-well (DWELL) structures embedded in a charge-tunable MISFET device and emitting near $\lambda = 1300$ nm under applied electric and magnetic fields, their excitonic and carrier properties were characterized. By applying a perturbative Coulomb blockade model, large single electron and hole confinement energies, small electron-electron and electron-hole interaction energies were measured, leading to larger effective lengths of the electron and hole wavefunctions and confirming that the DWELL structures are in the strong confinement regime. Due to strong confinement, the excitonic transitions can be tuned over a larger wavelength range compared to QDs in similar devices emitting at 950 nm. Permanent dipole moments (p/e) of -0.5 to -3.0 nm and polarizabilities (β) of -0.5 to -1.2 μeV/(kV/cm)^2 were measured. The diamagnetic response and g-factors of DWELL dots in applied magnetic fields up to 9 T in both the Faraday and Voigt geometries were reported. The Zeeman splittings were found to be smaller compared to dots emitting at 950 nm. The values of the diamagnetic shift changed drastically when changing the magnetic field direction from the Faraday to the Voigt configuration, but did not change considerably with the addition of an extra electron. Finally, measurements of exciton lifetimes were conducted. The lifetime of the bright exciton was found to be about 300 to 600 ps, and the slow decay time was found to be about 1 to 4 ns, the lifetime of the charged exciton was about 0.8 to 1.4 ns. This data is in line with the results previously obtained in our group.

These results are the first step forward toward further quantum optics experi-

ments including resonant fluorescence, single-photon generation, and characterization of the spin-dynamics of deep-confinement quantum dots emitting at telecom wavelengths.

3.7 References

[1] Luca Sapienza, Rima Al-Khuzheyri, Adetunmise Dada, Andrew Griffiths, Edmund Clarke, and Brian D. Gerardot, Magneto-optical spectroscopy of single charge-tunable InAs/GaAs quantum dots emitting at telecom wavelengths, *Physical Review B*, **93**, 155301 (2016).

[2] R. J. Warburton, C. Schäflein, D. Haft, F. Bickel, A. Lorke, K. Karrai, J. M. Garcia, W. Schoenfeld, and P. M. Petroff, Optical emission from a charge-tunable quantum ring, *Nature*, **405**, 926 (2000).

[3] P. A. Dalgarno, J. M. Smith, J. McFarlane, B. D. Gerardot, K. Karrai, A. Badolato, P. M. Petroff, and R. J. Warburton, Coulomb interactions in single charged self-assembled quantum dots: Radiative lifetime and recombination energy, *Physical Review B*, **77**, 245311 (2008).

[4] B. D. Gerardot, R. J. Barbour, D. Brunner, P. A. Dalgarno, A. Badolato, N. Stoltz, P. M. Petroff, J. Houel, and R. J. Warburton, Laser spectroscopy of individual quantum dots charged with a single hole, *Applied Physics Letters*, **99**, 243112 (2011).

[5] R. J. Warburton, B. T. Miller, C. S. Dürr, C. Bödefeld, K. Karrai, J. P. Kotthaus, G. Medeiros-Ribeiro, P. M. Petroff, and S. Huant, Coulomb interactions in small charge-tunable quantum dots: A simple model, *Physical Review B*, **58**, 16221 (1996).

[6] P. A. Dalgarno, Time correlated single photon counting on charge tunable semiconductor quantum dots, *PhD thesis*, (2005).

[7] R. J. Warburton, C. Schulhauser, D. Haft, C. Schäflein, K. Karrai, J. M. Garcia, W. Schoenfeld, and P. M. Petroff, Giant permanent dipole moments of excitons in semiconductor nanostructures, *Physical Review B*, **65**, 113303 (2002).

[8] A. J. Bennett, M. A. Pooley, R. M. Stevenson, M. B. Ward, R. B. Patel, A. Boyer de la Giroday, N. Skld, I. Farrer, C. A. Nicoll, D. A. Ritchie, and A. J. Shields, Electric-field-induced coherent coupling of the exciton states in a single quantum dot, *Nature Physics*, **6**, 947 (2010).

[9] O. D. D. Couto, Jr., J. Puebla, E. A. Chekhovich, I. J. Luxmoore, C. J. Elliott, N. Babazadeh, M. S. Skolnick, A. I. Tartakovskii, and A. B. Krysa, Charge control in InP/(Ga,In)P single quantum dots embedded in Schottky diodes, *Physical Review B*, **84**, 125301 (2011).

[10] C. Schulhauser, D. Haft, R. J. Warburton, K. Karrai, A. O. Govorov, A. V. Kalameitsev, A. Chaplik, W. Schoenfeld, J. M. Garcia, and P. M. Petroff, Magneto-optical properties of charged excitons in quantum dots, *Physical Review B*, **66**, 193303 (2002).

[11] Ming-Fu Tsai, Hsuan Lin, Chia-Hsien Lin, Sheng-Di Lin, Sheng-Yun Wang, Ming-Cheng Lo, Shun-Jen Cheng, Ming-Chih Lee, and Wen-Hao Chang, Diamagnetic response of exciton complexes in semiconductor quantum dots, *Physical Review Letters*, **101**, 267402 (2008).

[12] M. Bayer, O. Stern, A. Kuther, and A. Forchel, Spectroscopic study of dark excitons in $In_xGa_{1-x}As$ self-assembled quantum dots by a magnetic-field-induced symmetry breaking, *Physical Review B*, **61**, 7273 (2000).

[13] M. Bayer, G. Ortner, O. Stern, A. Kuther, A. A. Gorbunov, A. Forchel, P. Hawrylak, S. Fafard, K. Hinzer, T. L. Reinecke, S. N. Walck, J. P. Reithmaier, F. Klopf, and F. Schäfer, Fine structure of neutral and charged excitons in self-assembled In(Ga)As/(Al)GaAs quantum dots, *Physical Review B*, **65**, 195315 (2002).

[14] B. Van Hattem, P. Corfdir, P. Brereton, P. Pearce, A. M. Graham, M. J. Stanley, M. Hugues, M. Hopkinson, and R. T. Phillips, From the artificial atom to the Kondo-Anderson model: Orientation-dependent magnetophotoluminescence of charged excitons in InAs quantum dots, *Physical Review B*, **87**, 205308 (2013).

[15] Robert Zielke, Franziska Maier, and Daniel Loss, Anisotropic g factor in InAs self-assembled quantum dots, *Physical Review B*, **89**, 115438 (2014).

[16] Anthony J. Bennett, Matthew A. Pooley, Yameng Cao, Niklas Sköld, Ian Farrer, David A. Ritchie, and Andrew J. Shields, Voltage tunability of single-spin states in a quantum dot, *Nature Communications*, **4**, 1522 (2013)

[17] Julien Houel, Jonathan H. Prechtel, Andreas V. Kuhlmann, Daniel Brunner, Christopher E. Kuklewicz, Brian D. Gerardot, Nick G. Stoltz, Pierre M. Petroff, and Richard J. Warburton, High resolution coherent population trapping on a single hole spin in a semiconductor quantum dot, *Physical Review Letters*, **112**, 107401 (2014).

[18] V. Jovanov, T. Eissfeller, S. Kapfinger, E. C. Clark, F. Klotz, M. Bichler, J. G. Keizer, P. M. Koenraad, G. Abstreiter, and J. J. Finley, Observation and explanation of strong electrically tunable exciton g factors in composition engineered In(Ga)As quantum dots, *Physical Review B*, **83**, 161303(R) (2011)).

[19] M. Bayer, A. Kuther, A. Forchel, A. Gorbunov, V. B. Timofeev, F. Schäfer, J. P. Reithmaier, T. L. Reinecke, and S. N. Walck, Electron and hole g factors and exchange interaction from studies of the exciton fine structure in $In_{0.60}Ga_{0.40}As$ quantum dots, *Physical Review Letters*, **82**, 1748 (1999).

[20] J. M. Smith, P. A. Dalgarno, R. J. Warburton, A. O. Govorov, K. Karrai, B. D. Gerardot, and P. M. Petroff, Voltage control of the spin dynamics of an exciton in a semiconductor quantum dot, *Physical Review Letters*, **94**, 197402 (2005).

Chapter 4

Resonance fluorescence of telecommunication wavelength quantum dots

Until now, experiments on telecom wavelength quantum dots (QDs) have been carried out using non-resonant excitation which is characterized by inhomogeneous broadening of lines as a consequence of spectral wandering caused by charge fluctuations as well as time jitter between photon absorption and emission due to non-radiative relaxation of carriers to the excited state before recombination [1]. In order to make the emitted photons more coherent, make single photon generation more efficient, and set the stage for the study of spin dynamics, resonant excitation is needed.

In this chapter resonance fluorescence (RF) from single QDs emitting around $\lambda \approx 1300$ nm is demonstrated. The first sample is VN2209A, a metal-insulator-semiconductor field-effect transistor (MISFET) with a ZrO_3 super solid immersion lens (s-SIL), the structure of which was discussed in Section 2.1.1. The second sample is a *p-i-n* diode sample provided by Toshiba Research Europe, Cambridge Research Laboratory, described briefly in Section 2.1 and Ref. [2]. RF detuning spectra for both samples are shown to be substantially broadened due to charge noise. The exciton plateau of the QDs is mapped out, and emission is characterized as a function of resonant excitation power. High-resolution spectroscopy of photons scattered by the QD under resonant excitation is performed. Finally, emission linewidth broadening due to charge noise is extracted from the measured data.

To perform resonant laser spectroscopy at 4 K a confocal microscope with a high numerical aperture ($NA = 0.68$) objective lens is used. The scattered laser light is suppressed using orthogonal linear polarizers in the excitation and collection arms of the microscope head. A high-performance telecom wavelength continuous wave (cw) laser diode tuned to resonance is used for excitation. A superconducting nanowire single photon detector (SNSPD) optimized for detection at 1310 nm at 2.8 K and an InGaAs single-photon avalanche diode (SPAD) at 90 K are used for single photon detection. The working principle of the detectors was outlined in Section 2.2.12.

The experiments described in this chapter are the first steps towards telecom wavelength single-photon generation under resonant excitation, the generation of on-demand polarization-entangled photons, and the characterization of spin-dynamics in 1300 nm wavelength quantum dots.

4.1 RF from QDs embedded in a MISFET structure

The first set of telecom RF measurements was carried out on a QD embedded in sample VN2209A, one of the MISFET structures studied in Chapter 3. A Sacher laser was used for resonant excitation and one of two SNSPD registered single photons. The microscope system was well-aligned, with efficiencies above 1%. Typical extinction ratios were around 10^5.

4.1.1 First signs of RF

Hole storage at the interface of the blocking barrier and the capping layer of this sample that occurs under non-resonant excitation results in the creation of an internal electric field within the sample that works to partially counter the effect of the applied external bias [3,4]. This effect does not occur under resonant excitation and can to be taken into account when searching for RF in one of two ways. First, measuring a dependence of QD emission wavelength on non-resonant excitation power can make it possible to estimate the shift in emission wavelength through interpolation. Second, a low power, long acquisition time PL map can be taken to determine the QD emission energy at excitation powers as low as possible, where the effect of hole storage is minimized.

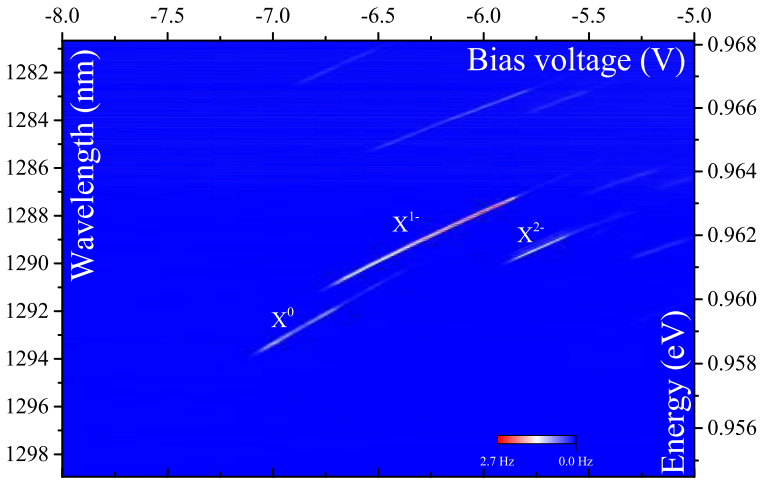

Figure 4.1: PL spectra collected as a function of applied diode bias under 1 μW 830 nm non-resonant excitation of a single charge-tunable QD embedded in a MISFET structure as measured on the 1200 groove/mm grating of the spectrometer. The lines corresponding to neutral (X^0) and charged (X^{1-} and X^{2-}) excitons are labeled. Maximum counts correspond to 2.7 counts/s.

Fig. 4.1 shows a microphotoluminescence (μ-PL) map of a telecom charge tunable QD from sample VN2209A taken under low power non-resonant excitation as a function of voltage applied to the device, revealing the presence of a neutral (X^0) and negatively charged (X^{1-}) excitons. At saturation, counts from this QD reach 50 counts/s, which is an order of magnitude higher than is typically seen from QDs on this sample.

In order to broaden the RF linewidth and make the signal easier to find, the pump power of the resonant laser can be increased, but a side-effect of this is an increase in the background counts, and, consequently, a decrease in the signal-to-background ratio (SBR) of the RF signal.

Using Fig. 4.1, a range of biases where RF can be found for a particular excitation wavelength were identified. To search for RF, we set the resonant excitation laser wavelength, scanned the voltage applied to the QD sample across the expected range, and recorded the collected signal on one of the SNSPDs. An increase in photon counts, such as that seen in the detuning spectrum in Fig. 4.2 signifies the presence of RF. The figure shows signal collected from the neutral exciton line in Fig. 4.1(b) under 5.7 nW resonant excitation at 1293.9327 nm. The full width at half maximum (FWHM) of the detuning spectrum is 94 ± 3 μeV, which is much larger

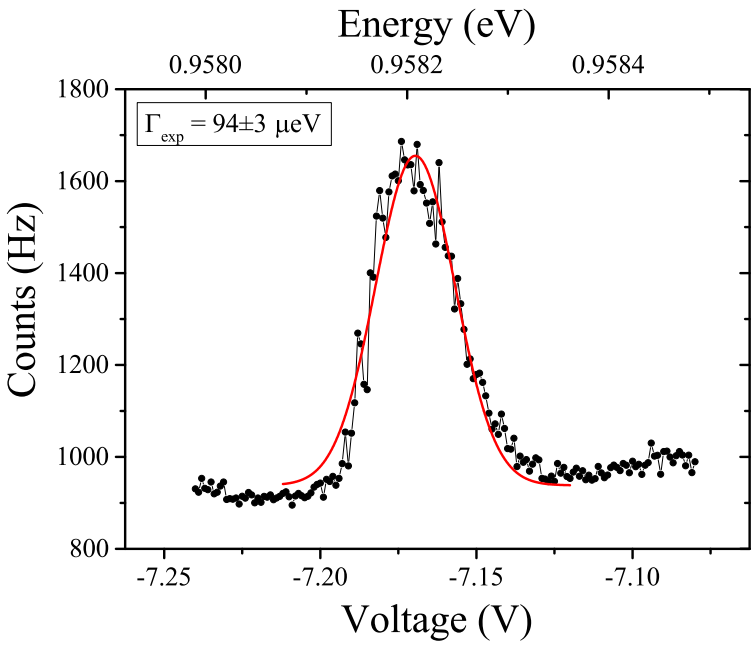

Figure 4.2: The RF signal collected from the neutral exciton from a QD in a MISFET structure with the resonant laser set at a wavelength of 1293.9327 nm. The scan was performed with a 1 mV step and a resonant excitation power of about 5.7 nW. The solid line is a fit to the data. Γ_{exp} is the linewidth of the detuning spectrum.

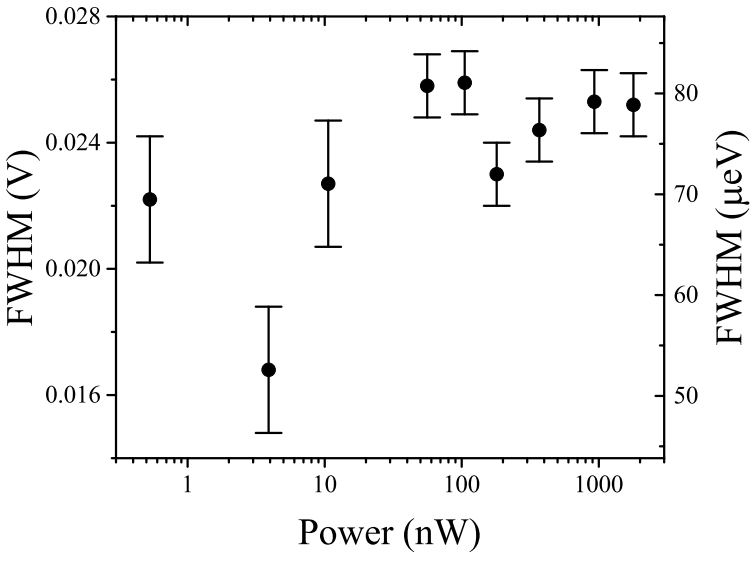

Figure 4.3: The FWHM of the fits to the detuning spectra of emission from a neutral exciton in a QD within a MISFET structure under resonant excitation set at a wavelength of 1293.9327 nm as a function of laser diode power.

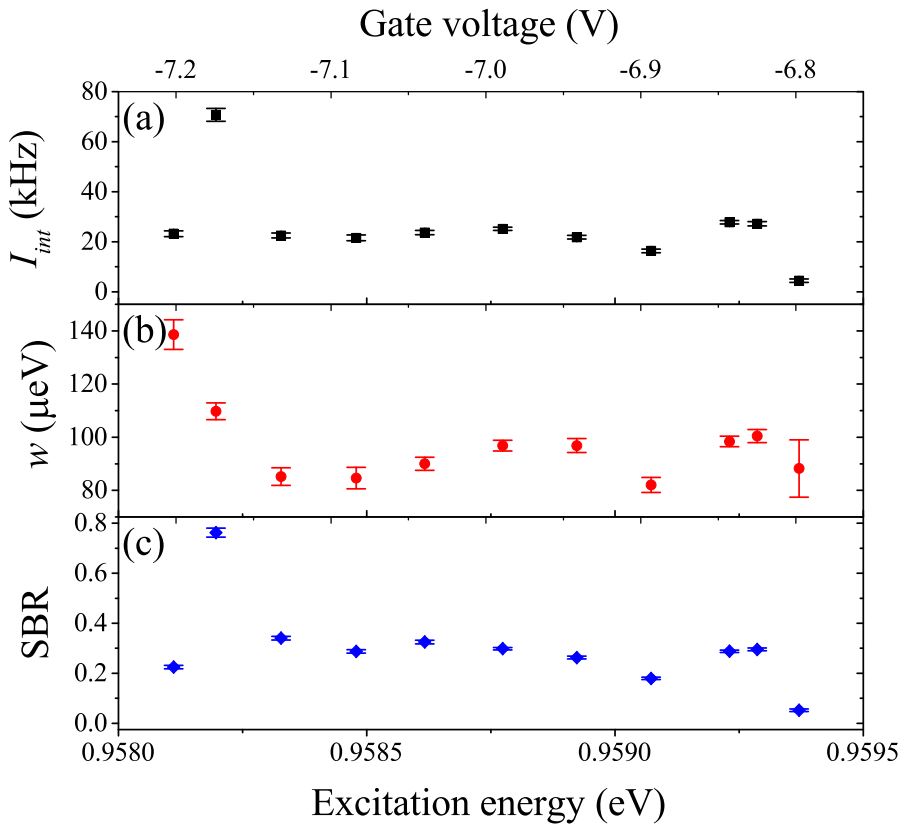

Figure 4.4: Plateau mapping of RF from the neutral exciton under 5.7 nW resonant excitation. The integrated intensity (a) and the FWMH (b) of the fits to the detuning spectra at different excitation laser wavelengths. (c) The SBR of the RF signal. The measurement at -7.17 V appears to be a random outlier.

than the typical homogeneous linewidth of about 1 μeV [5]. Spectral fluctuations caused by charge noise [6, 7] are the most likely main cause of line broadening. Additionally, the integrated RF counts (22.0 ± 0.5 kHz) are much lower than those calculated ($\approx 10^7$) using the estimated values of microscope head system and sample collection efficiencies, the efficiency of the SNSPD, and the typical lifetime for such QDs (about 1 ns, see Chapter 3).

Broadened linewidths were recorded at lower excitation powers as well, signifying that power broadening was likely masked by broadening caused by charge noise. Fig. 4.3 shows a dependence of the RF signal linewidth on resonant laser power.

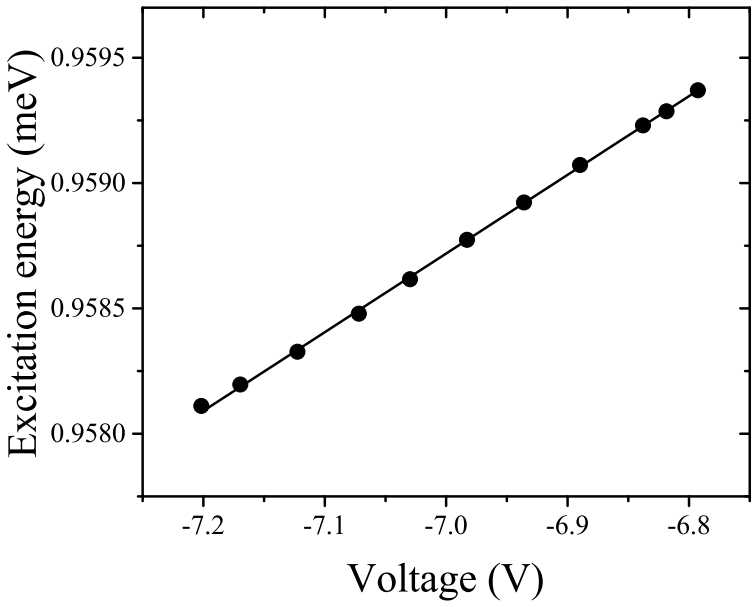

Figure 4.5: Dependence of RF energy from a neutral exciton as a function of bias applied to the top gate of the MISFET sample. The black line is a linear fit with a slope of 3.13 ± 0.02 μeV/mV.

4.1.2 Exciton plateau mapping in RF

Next, RF is detected across the full voltage extent of the neutral exciton plateau as it is seen on the PL map. Fig. 4.4(a) shows the integrated intensity of the measured detuning spectra, and Fig. 4.4(b) shows the signal linewidth across the plateau. Fig. 4.4(c) shows the SBR of the RF signal across the plateau, averaging about 0.3.

By measuring detuning spectra at different excitation laser wavelengths, it is possible to calculate the Stark shift of the neutral exciton line under resonant excitation (see Fig. 4.5). The data is fit by a line with a slope of 3.13 ± 0.02 μeV/mV. For comparison, the Stark shift measured under non-resonant (830 nm) excitation for this dot is about 2.82 ± 0.01 μeV/mV. The difference between the values is most likely a consequence of the change in the charge environment surrounding the QD under non-resonant excitation.

4.1.3 Discussion

While RF from the X^0 state was clearly visible, an attempt to find RF from X^{1-} state was unsuccessful. The low RF SBR from the X^0 state is most likely a consequence of a number of factors, including low detection efficiency of the SNSPDs, low collection efficiency of the sample, and broadening of the emission lines likely

caused by charge noise. Modest excitation laser cancellation (10^5) contributed to low SBR. To eliminate the possibility of the resonant laser wavelength drift over the measurement time, a way of locking the laser wavelength was realized for the second RF experiment on telecom wavelength QDs.

While RF from QDs emitting at around 1300 nm was demonstrated for the first time (to the best of our knowledge), the low amplitude of the signal and the high background make a further study of QDs in this sample difficult. A sample with a better collection efficiency or lower charge noise may offer a significant improvement to the RF counts.

4.2 RF from QDs embedded in a *p-i-n* diode

This section describes the investigation of RF from a QD embedded in a *p-i-n* diode and emitting around 1300 nm. Additionally, the effect of charge noise on RF from telecom wavelength QDs is characterized in detail.

The set up used for these measurements was similar to the one described in Section 4.1. A high performance Toptica laser replaced the Sacher laser as the source of resonant excitation. The Toptica laser was locked to a set emission wavelength using a HighFinesse wavelength meter and remained stable within 0.007 μeV of the set value. Both the SPAD (30% efficiency) and the SNSPDs were used for better detection efficiency and increased dynamic range respectively. The alignment efficiency of the microscope system was above 1%. Suppression of laser counts was above 10^6, more than an order of magnitude higher than in the previous experiment, most likely due to a smoother sample surface and a better performance of the new resonant laser.

The PL map in Fig. 4.6(a) was taken under non-resonant 830 nm excitation by sweeping the bias voltage applied to the diode. The map shows emission of the different states of a single QD. The brightest lines have a maximum intensity of about 16.7 counts/s, about 3 times less than the intensity of the neutral exciton line studied in Section 4.1 (about 50 counts/s at saturation). The loss of intensity of the signal at certain voltages is typical behavior for QDs within a *p-i-n* diode under non-resonant excitation that has not yet been explained. Interestingly, it was found that excitation at a wavelength of 1064 nm of a higher-energy state gave a much cleaner PL map with brighter lines (see Fig. 4.6(b)). The brightest lines under

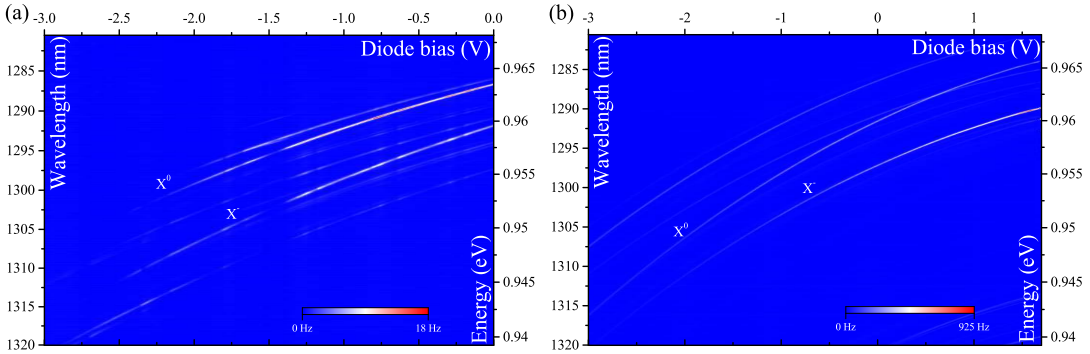

Figure 4.6: PL spectra collected as a function of the applied diode bias from a single QD within a *p-i-n* diode under two different excitation configurations: (a) represents 830 nm non-resonant excitation and (b), excitation with a wavelength of 1064 nm. The two lines of interest, corresponding to the emission from the neutral exciton and charged exciton from a single QD are labeled. The 830 grooves/mm spectrometer grating was used.

1064 nm excitation had an intensity of about 1 kHz. The neutral exciton line was identified by the presence of the fine-structure splitting (FSS), which was measured to be equal to 108.6 ± 3.8 μeV under 1064 nm cw excitation. This measurement was performed by Dr Jan Huwer, Toshiba Research Laboratory, Cambridge.

All further measurements were performed on the neutral exciton line. Measured under pulsed 1064 nm excitation, the lifetime of the neutral exciton was found to be equal to $T_1 = 1.394 \pm 0.006$ ns. The coherence time, measured using a Mach-Zehnder interferometer under cw 1064 nm excitation, was equal to $T_2^{non-res} = 89 \pm 8$ ps. These temporal measurements were performed by Dr Jan Huwer. Here $T_2^{non-res} \ll 2T_1$, which is expected from a measurement performed with non-resonant excitation. Later in this chapter it is demonstrated that photons generated resonantly from the same state have significantly improved coherence.

To look for RF the resonant laser was locked and the voltage swept in the range of interest. We were able to successfully find RF from the neutral exciton state from Fig. 4.6. A brief attempt to find RF from the X^{1-} state was not successful due to time constraints, but perhaps a more thorough investigation would have yielded better results. Fig. 4.7 shows the RF counts from the neutral exciton as the diode voltage was swept through the excitation laser resonance at powers below and above saturation (saturation power and Rabi frequency are $P_{sat} = 3.5$ nW and

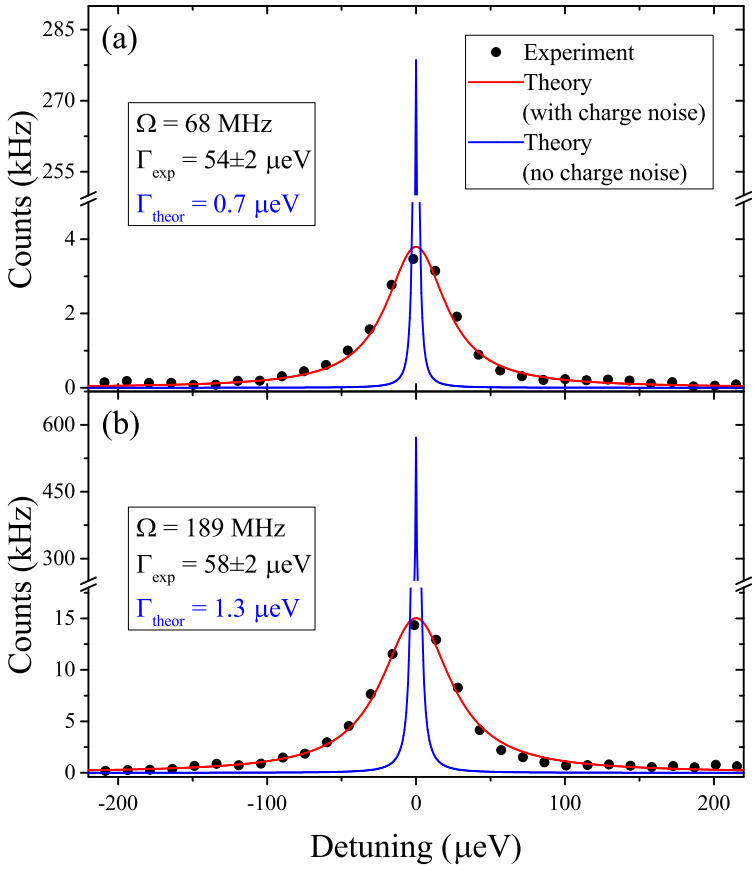

Figure 4.7: The RF detuning spectra (black points) collected from the neutral exciton from a single QD within a *p-i-n* diode below (a) and above (b) saturation with the laser background subtracted (1.76 ± 0.03 kHz and 5.9 ± 0.1 kHz, respectively). The resonant laser was locked at 1285.28200 nm. The scan was performed for diode bias voltages $1.30-1.45$ V in 5 mV steps. For each point in the figure the count rates were averaged over 5 s. The solid red curve is a simulated detuning spectrum obtained using the master equation method with non-zero charge noise to fit the measured data. The solid blue curve represents the simulated detuning spectrum without the spectral fluctuations caused by charge noise. Ω is the Rabi frequency, Γ_{exp} and Γ_{theor} are the linewidths of the analytically calculated detuning spectra with and without charge noise, respectively.

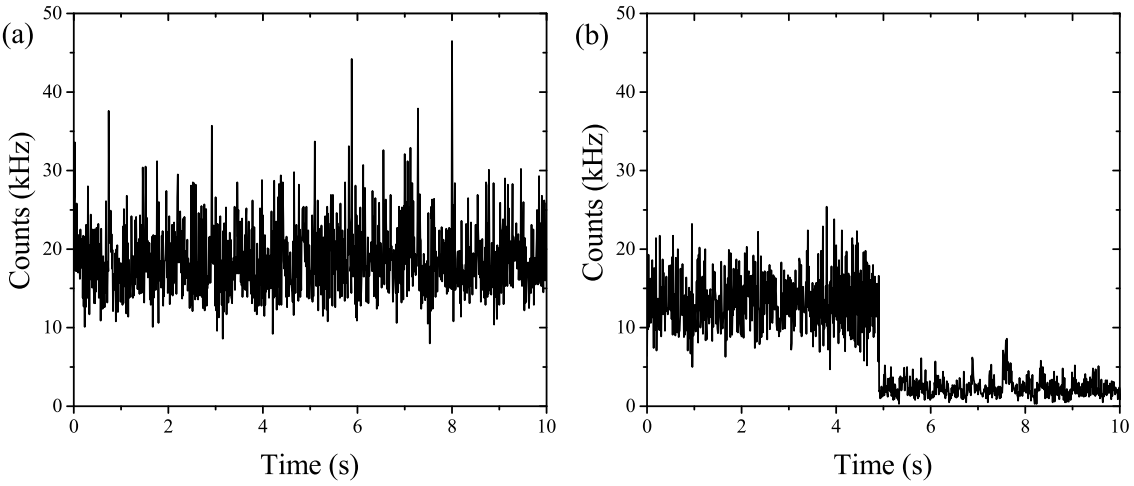

Figure 4.8: Timetraces of RF counts from a neutral exciton in a single QD within a *p-i-n* diode at resonant excitation powers (a) 60 nW and (b) 18 nW.

$\Omega_{sat} = 88$ MHz, respectively (see Section 4.2.3)). As is the case with RF from QDs in a MISFET device, the RF linewidth is significantly broadened (54 ± 2 μeV and 58 ± 2 μeV for RF at the low and the high excitation powers in Fig. 4.7, respectively) from the value expected based on the measured T_1, likely due to spectral fluctuations caused by charge noise. In order to estimate the effect of charge noise, detuning spectra with non-zero charge noise (red curves) were obtained analytically and found to be a good fit to the measured data (black dots) (see Fig. 4.7). The blue curve shows the simulated detuning spectra in the absence of charge noise. These and all other simulations, the results of which are described in this chapter, were performed by Dr Ted Santana.

A significant problem encountered during the RF experiment on QDs embedded in a *p-i-n* diode was the occasional disappearance of the RF signal at low resonant laser excitation powers (< 50 nW), possibly caused by a depletion of carriers. This problem did not appear in QDs in a MISFET device. RF reappeared if the diode bias was changed to a more negative value (about -4 V) for several seconds or once the sample was briefly illuminated with a high power 830 nm laser, presumably resulting in the reappearance of carriers. Fig. 4.8 shows timetraces of neutral exciton RF at resonant excitation powers equal to 60 nW and 18 nW, respectively. The higher power measurement shows continuous emission, while at a lower power the emission from the QD disappears after ≈ 5 s.

In the RF experiment only one line was observed in the detuning spectra. There

are several possible explanations for this. First of all, it is possible that the orientation of the linear polarizers in the excitation and collection arms of the microscope head caused the collected signal from one of the lines to become significantly lower in intensity than from the other. This effect was compounded by low RF SBR. Alternatively, it is possible that the QD is not located in the center of the aperture, in which case it is excited primarily with laser light reflected off the rough Al layer on the edge of the aperture. This would change the polarization of light exciting the QD, possibly causing the excitation of one linearly polarized component to become suppressed. Finally, a comparison of PL spectra taken under 830 nm and 1064 nm non-resonant excitation shows different lines being excited at a particular bias in each case. Based on this, it is possible that the charge state of lines excited resonantly does not correspond to what is expected from Fig. 4.6(b) due to a changing charge environment surrounding the QD.

While in this thesis the state under study is referred to as a neutral exciton, a two-level model was used to simulate the detuning spectra since only one peak is visible in RF.

4.2.1 Exciton plateau mapping in RF

By recording RF at a series of resonant excitation laser wavelengths, the full voltage extent of the neutral exciton plateau was mapped. Fig. 4.9(a,b) shows the peak position and the integrated intensity of the Lorentzian fits to the RF detuning spectra obtained at a range of excitation wavelengths. The linewidth of the Lorentzian fit to the RF detuning spectra over the extent of the exciton plateau is given in Fig. 4.9(c), and is shown to decrease slightly for emission at more positive biases. The plateau mapping was carried out at excitation laser powers above saturation due to the instability of the RF signal at lower powers.

Mapping the plateau of the neutral exciton under resonant excitation allowed us to calculate the Stark shift in RF. Fig. 4.10(a) shows the peak energy of the Lorentzian fit to the RF signal taken as function of the electric field resultant from the voltage bias applied to the diode. The solid red line is a quadratic fit to the data given by the following equation:

$$E_{PL} = E_0 - pF + \beta F^2; \tag{1}$$

where the electric field F is a function of the built-in voltage (V_0) and the thickness

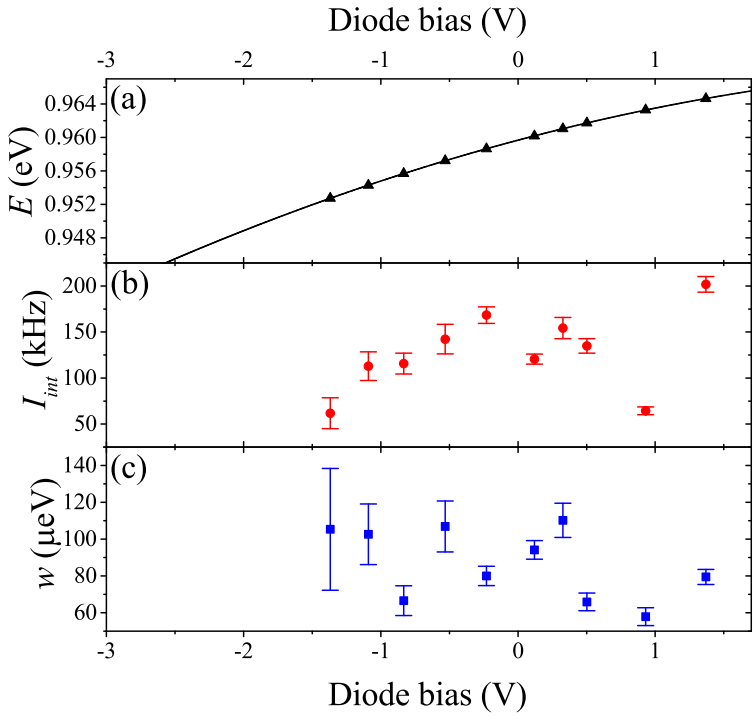

Figure 4.9: The linewidth (a), integrated intensity (b), and FWHM (c) of the Lorentzian fits to the RF detuning spectra of a single QD within a *p-i-n* diode taken at various excitation wavelengths at a power of 77 nW (Ω = 409 MHz > Ω_{sat} = 139 MHz). The solid black curve in (a) is a quadratic fit to the data.

of the intrinsic region (d):

$$F = -(V_g - V_0)/d. \tag{2}$$

For this sample, the built-in voltage is equal to 2.2 V and the thickness of the intrinsic region is 203 nm [2]. The permanent dipole moment (p/e, where e is the elementary charge) and the polarizability (β) are extracted from the fit, and are equal to 0.420 ± 0.004 nm and -0.2139 ± 0.0001 μeV/(kV/cm)^2, respectively for this QD.

The Stark shift was calculated for emission under 1064 nm cw excitation for comparison. Fig. 4.10(b) gives the peak energy of the fit to the PL signal taken as function of the electric field applied to the diode, and the red line is a quadratic fit. The Stark shift parameters extracted from the fit are $p/e = 0.385 \pm 0.001$ nm and $\beta = -0.2288 \pm 0.0004$ μeV/(kV/cm)^2. The differences in parameters observed for resonant and non-resonant excitation are most likely a result of additional charging of the host semiconductor material induced by non-resonant excitation.

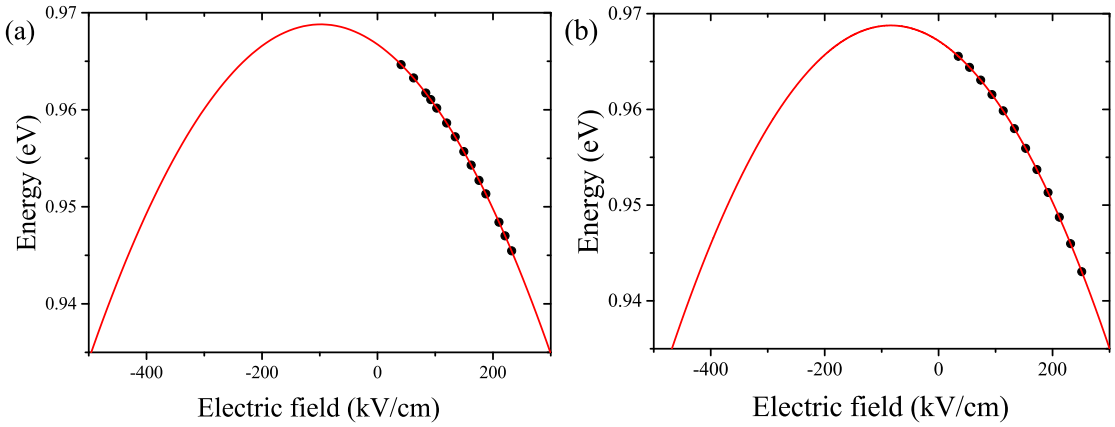

Figure 4.10: Peak energy of the Lorentzian fit to the RF detuning spectra versus electric field (calculated from the diode voltage using Eq. 2) for the X^0 line from a single QD within a *p-i-n* diode measured under resonant excitation at 77 nW (a) and non-resonant excitation (1064 nm) (b). The solid red curves are quadratic fits to the data using Eq. 1.

4.2.2 Modeling spectral fluctuations

The analytical detuning spectra in Section 4.2 were obtained using the model described below [8].

The following master equation is used to model RF from two-level system driven by a near-resonant electromagnetic field:

$$\dot{\rho} = -\frac{i}{\hbar}\left[\hat{\mathcal{H}}, \rho\right] + \hat{\mathcal{L}}\rho(\sigma_-) + \hat{\mathcal{L}}\rho(\sigma_z). \tag{3}$$

Here ρ is the density matrix, $\hat{\mathcal{H}}$ is the Hamiltonian describing the interaction of the system with the driving field, and σ_i are the transition operators for a two-level system with ground state $|1\rangle$ and excited state $|2\rangle$:

$$\hat{\sigma}_- = |1\rangle\langle 2|\,; \tag{4}$$

$$\hat{\sigma}_+ = |2\rangle\langle 1|\,; \tag{5}$$

$$\hat{\sigma}_z = |1\rangle\langle 1| - |2\rangle\langle 2|\,. \tag{6}$$

The Lindblad superoperator, acting on the density matrix, describes the photon emission process from the excited state and the pure dephasing:

$$\hat{\mathcal{L}}\rho(\sigma_-) = \frac{\Gamma\left(2\sigma_-\rho\sigma_+ - \sigma_+\sigma_-\rho - \rho\sigma_+\sigma_-\right)}{2}; \tag{7}$$

$$\hat{\mathcal{L}}\rho(\sigma_z) = \frac{\gamma\left(\sigma_z\rho\sigma_z - \rho\right)}{2}. \tag{8}$$

Parameter Γ is the radiative decay rate of the system, and $\phi = \Gamma/2 + \gamma$, where γ is the pure dephasing rate.

The Hamiltonian can be written in the following form:

$$\hat{\mathcal{H}} = \frac{1}{2}\left(\Omega_e\left(\hat{\sigma}_- + \hat{\sigma}_+\right) + \Delta\hat{\sigma}_z\right); \tag{9}$$

where Ω_e is the Rabi energy, and Δ is the transition detuning from resonance.

Eq. 3 can be used to write the optical Bloch equations, and their steady state solutions can be obtained by solving $\dot{\rho} = 0$. Of these, the following relation is of particular interest to us:

$$\rho_{22} = \frac{\Omega_e^2\phi}{2\Gamma\left(\Delta^2 + \frac{\phi\Omega_e^2}{\Gamma} + \hbar^2\phi^2\right)}. \tag{10}$$

Using Eq. 10 the average number of photons ($\langle n\rangle$) as a function of detuning (detuning spectrum) can be obtained:

$$\langle n\rangle = \eta\rho_{22}\Gamma = \frac{\eta\Omega_e^2\phi}{2\left(\Delta^2 + \frac{\phi\Omega_e^2}{\Gamma} + \hbar^2\phi^2\right)}; \tag{11}$$

where η is the photon detection efficiency, defined as the ratio between the expected number of photons in the absence of spectral fluctuation and the expected number of photons under perfect collection efficiency.

In the case of resonant excitation we have the following:

$$\langle n\rangle = \frac{\eta\Gamma}{2}\frac{\Omega_e^2}{\Omega_e^2 + \Omega_{e,sat}^2}; \tag{12}$$

where $\Omega_{e,sat}^2 = \hbar\sqrt{\phi\Gamma}$ is the saturation Rabi energy.

To account for the spectral fluctuations the average number of photons is integrated over the Lorentzian distribution:

$$\langle n_{ch}\rangle = \frac{w}{2\pi}\int_{-\infty}^{\infty}\frac{\langle n(\delta)\rangle\, d\delta}{\delta^2 + \left(\frac{1}{2}w\right)^2}. \tag{13}$$

Here w is the width of the distribution and is referred to as charge noise width, and δ is the additional detuning caused by charge noise.

Eq. 13 is used to obtain the red curves in Fig. 4.7. The free parameters in the simulation are the charge noise width and the photon detection efficiency. The blue curves are obtained using Eq. 11 and the measured T_1.

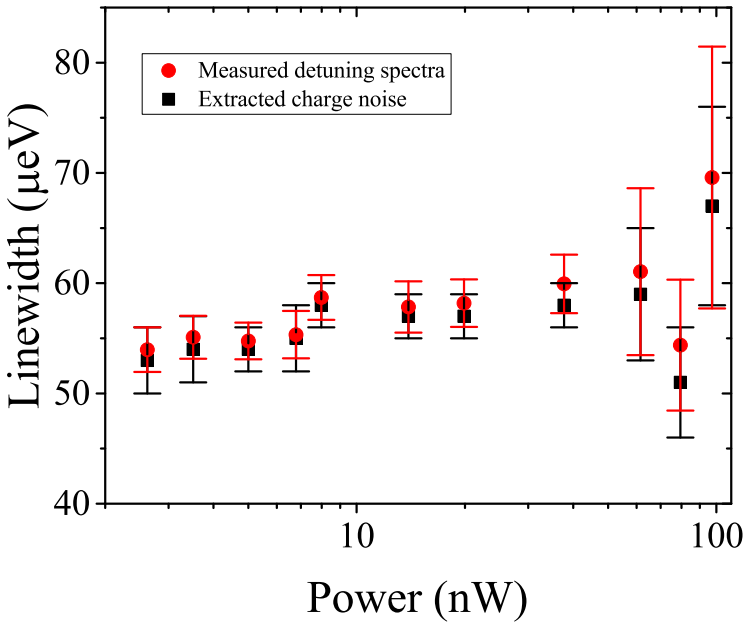

Figure 4.11: The red dots give the linewidths of the fits to the detuning spectra of a neutral exciton in a single QD within a *p-i-n* diode at different powers. Black squares give the width of the charge noise distribution extracted from the measured spectra. Resonant laser wavelength was set at 1285.28200 nm. The scan was performed for diode biases 1.3-1.45 V in 5 mV steps with each data point averaged over 5 s.

4.2.3 Power dependence

To investigate broadening of the RF signal, the linewidths of the detuning spectra are measured at different excitation powers (see Fig. 4.11, red dots). Some further broadening at higher excitation powers is observed. Charge noise is expected to contribute significantly to linewidth broadening at lower resonant laser excitation powers due to spectral fluctuations, while at higher Rabi frequencies the linewidth is increased considerably due to power broadening, decreasing the relative effect of charge noise. To estimate the effect of charge noise on the detuning spectrum, the width of the noise distribution is extracted from the measurements by fitting the raw data with Eq. 13 (see Fig. 4.11, black dots) and compared to the width of the detuning spectrum. The data presented provide strong evidence that spectral fluctuations due to charge noise are the main source of linewidth broadening of the detuning spectrum of these QDs.

The dependence of RF counts in the detuning spectra on excitation power (red dots) is measured and compared with the simulated detuning spectra RF count rate

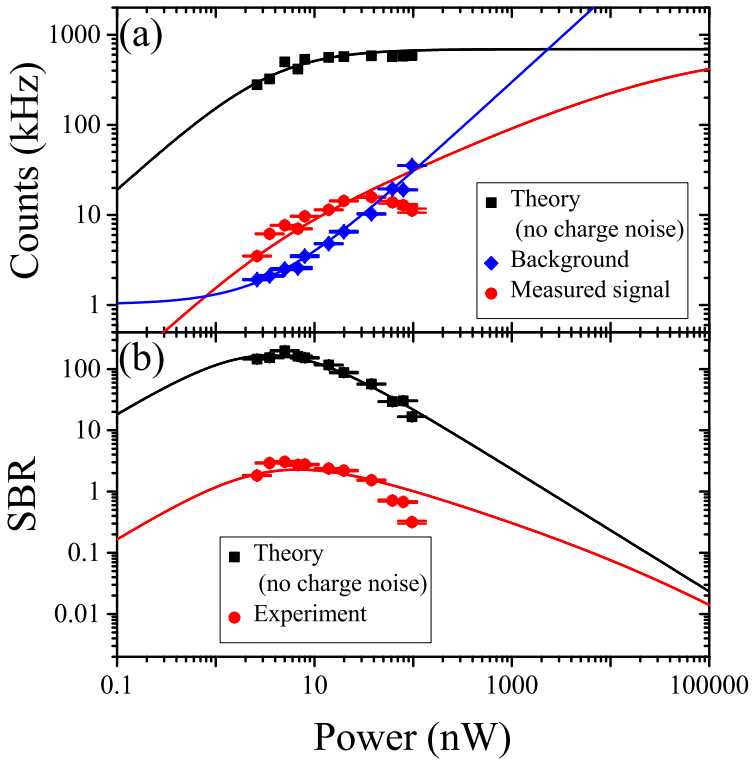

Figure 4.12: (a) The amplitude of the fits and the background counts of the detuning spectra at different powers from a neutral exciton in a single QD within a *p-i-n* diode (red dots and blue diamonds, respectively). The resonant laser wavelength was set at 1285.28200 nm. The scan was performed for diode biases 1.3-1.45 V in 5 mV steps with each data point averaged over 5 s. Black squares represent the amplitude of the simulated spectrum without spectral fluctuation. The red and black solid curves are the theoretical saturation curves for the corresponding cases. The blue line is a linear fit to the blue data points. (b) SBR power dependence of the measured detuning spectra (red dots) and simulated detuning spectra in the absence of charge noise (black squares). The solid curves are fits to the data points.

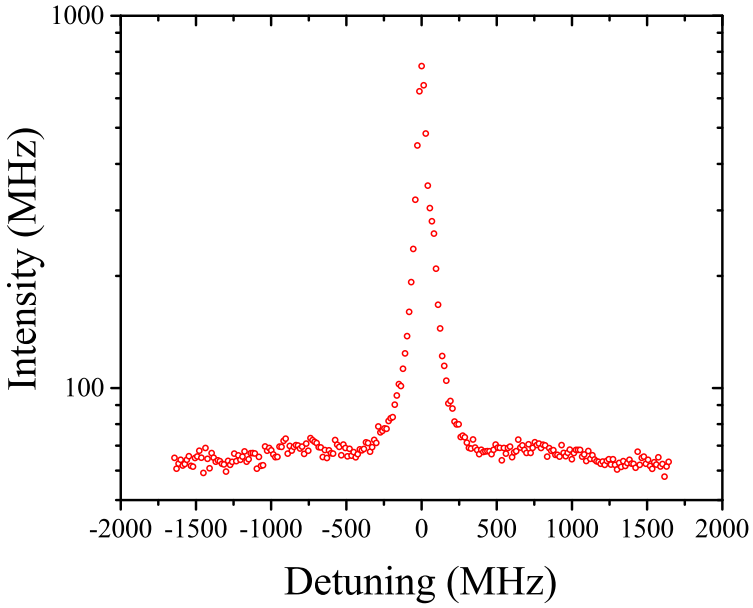

Figure 4.13: A high-resolution RF spectra of neutral exciton emission from a single QD within a *p-i-n* diode as a function of FPI detuning at a Rabi frequency equal to 859 MHz, showing the elastically and inelastically scattered components.

power dependence (black squares) in the absence of charge noise (see Fig. 4.12(a)). To obtain the latter, the experimental data is fit with Eq. 13, and the extracted value of the photon detection efficiency is used to calculate the theoretical detuning spectrum using Eq. 11. Both power dependencies are fit using Eq. 12, where $\Omega_e^2 \propto P/\hbar^2$ (P is the excitation power) and demonstrate saturation behavior (red and black curves). The saturation power (P_{sat} = 3.5 nW) is extracted from the analytically obtained power dependence of photon counts in the absence of charge noise. Using the power dependencies along with the background counts from the measured detuning spectra (blue diamonds), the experimental and theoretical SBR is calculated (see Fig. 4.12(b)). The average measured SBR is ≈ 3, about a factor of 10 increase compared to the RF SBR of QDs in a MISFET device. The high value of background counts is a result of imperfect cancellation of scattered excitation laser light on the relatively rough Al sample surface around the QD.

4.2.4 High-resolution RF measurements

High-resolution spectroscopy of RF from a single QD within a *p-i-n* diode was performed by filtering the emission signal with a Fabry-Pérot interferometer (FPI).

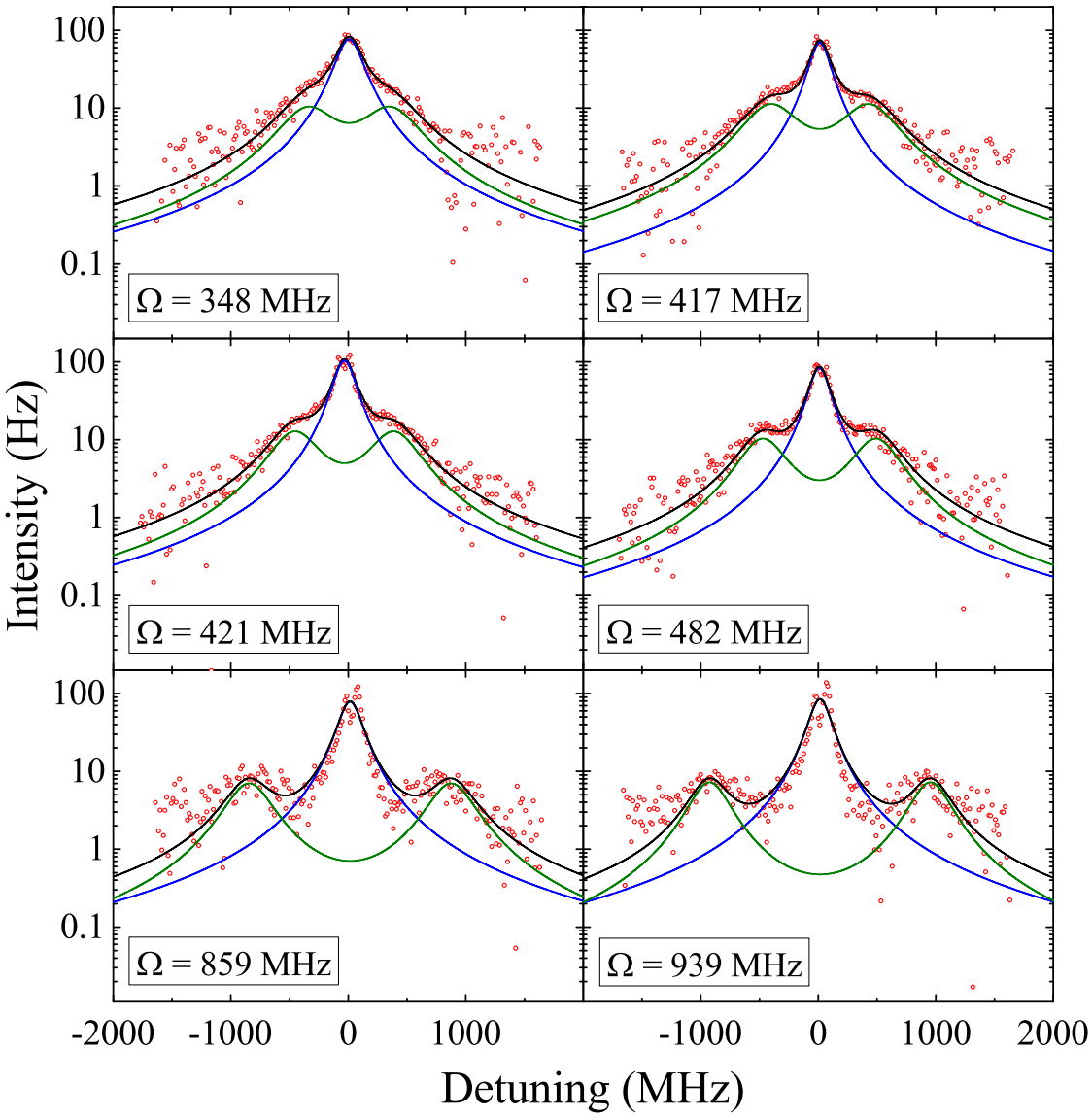

Figure 4.14: The inelastically scattered component of the high-resolution RF spectra of neutral exciton emission from a single QD within a *p-i-n* diode filtered through the FPI, shown as a function of FPI detuning for six different Rabi frequencies (red circles). The solid curves are the Lorentzian fits: the inelastic side peaks (green curve), the inelastic central peak (blue curve), and the sum of the above (black curve).

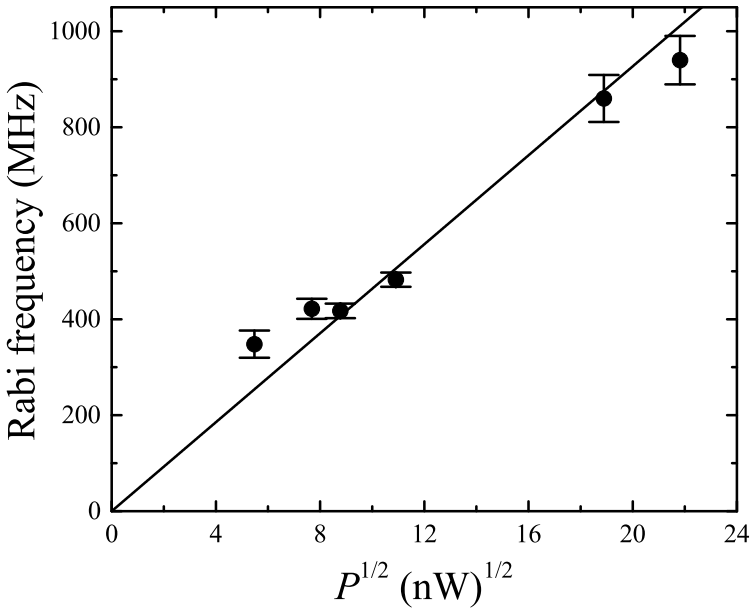

Figure 4.15: Rabi frequency as a function of the square root of power for a RF signal from the neutral exciton from a single QD within a *p-i-n* diode. The Rabi frequency is extracted from the Lorentzian fits to the high-resolution spectra as the splitting between the inelastic side peaks and the inelastic central peak.

A reference laser signal was used to track spectral drift of the FPI caused by changing ambient conditions over the measurement time. Spectra at each power were averaged over about 20 minutes. An example spectrum is shown in Fig. 4.13. Each spectrum was fit with four Lorentzian peaks in agreement with Eq. 35 from Chapter 1, with the delta function replaced by a Lorentzian peak with a width equal to the resolution of the FPI. The narrow central peaks were composed not only of the elastically scattered photons from the QD, but also background laser light. The elastic peak could not be extracted from the fit because it had the same linewidth as the laser. The considerable contribution of the laser light to the narrow peak is a consequence of poor cancellation. For further data analysis, the narrow peak was subtracted from the data.

Fig. 4.14 shows the inelastically scattered component of the high-resolution spectra at several different Rabi frequencies (red circles), with the Mollow triplet clearly visible. The components of the Mollow triplet (black curve) are the two inelastic side peaks (green curve) and the inelastic central peak (blue curve). The Mollow triplet is a feature of a two-level system driven by a strong resonant field.

In the spectral domain, the Rabi frequency is defined as the splitting between the

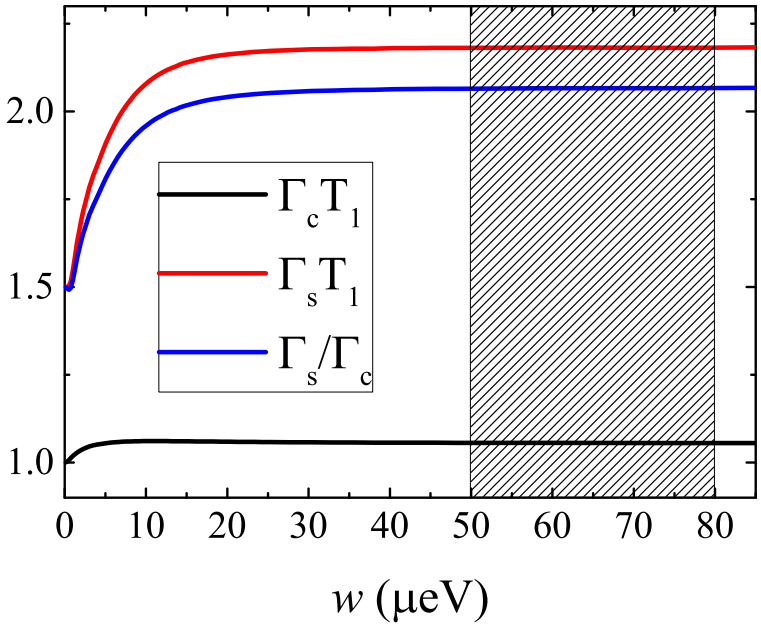

Figure 4.16: Simulation of high-resolution spectra linewidths of the inelastic central (black curve) and side (red curve) peaks and the ratio of the two (blue curve) as a function of charge noise width. The range of our high-resolution measurements is indicated by the patterned area.

inelastic side peak and the inelastic central peak. Fig. 4.15 gives the Rabi frequency as a function of the square root of excitation laser power. The splitting increases linearly with power, as expected. Central and side peak linewidths are measured to be around $\Gamma_c = 0.161 \pm 0.003$ GHz and $\Gamma_s = 0.47 \pm 0.02$ GHz, respectively. The average ratio of integrated central peak to side peak intensities is $I_c/I_s = 4.0 \pm 0.2$. We attribute the departure from theory ($I_c^{th}/I_s^{th} = 2$) to the effect of charge noise.

In the ideal case, the expected width of the central peak is $\Gamma_c^{th} = (2\pi T_1)^{-1} = 0.115$ GHz for $T_1 = 1.39$ ns. At higher Rabi frequencies the relative contribution of charge noise to linewidth broadening is reduced, and on average, widths of $\Gamma_c = 0.161 \pm 0.003$ GHz are observed, which is consistent with a case of negligible pure dephasing. Based on the lifetime ($T_1 = 1.394 \pm 0.006$ ns) and coherence time ($T_2^{non-res} = 89 \pm 8$ ps) for this state measured under cw 1064 nm excitation, the following relation is valid: $T_2^{res} \approx 2T_1 \gg T_2^{non-res}$. Consequently for all simulations, a dephasing rate equal to zero is assumed.

Fig. 4.16 shows the dependence of the inelastic central and side peak linewidths and their ratio on the charge noise width obtained by a numerical simulation. In this simulation the effect of charge noise on the high-resolution spectrum is accounted

for by integrating Eq. 36 from Chapter 1 over the Lorentzian distribution. In the ideal transform-limited case for these simulations $\Gamma_s/\Gamma_c = 3/2$ and $\Gamma_c T_1 = 1$ (see Section 1.1.5). Charge noise affects the widths of the central and side peaks, causing them to increase and then reach saturation. Due to the saturation nature of the curves, it is impossible to extract the charge noise width from the high-resolution spectroscopy data.

4.3 Discussion and further directions

Table 4.1: Comparison of RF experiments on QDs embedded in a MISFET device and on QDs within the intrinsic region of a *p-i-n* diode sample provided by Toshiba.

	MISFET	***p-i-n* diode**
Detectors	SNSPD1, SNSPD2	SNSPD1, SNSPD2, SPAD
Resonant excitation laser	Sacher	Toptica
Cancellation	10^5	$> 10^6$
Exciton state	X^0, no second peak, no RF signal on X^{1-}	X^0, no second peak, no RF signal on X^{1-}
Typical SBR	0.3	3
Detuning spectrum linewidth	90 μeV	55 μeV

In this chapter resonance fluorescence from QDs emitting around 1300 nm is reported for the first time. RF was detected from telecom wavelength QDs in two structures: a MISFET device and a *p-i-n* diode (see Table 4.1). RF from the QD within a *p-i-n* diode was found to have a SBR equal to about 3. The main drawback of RF from the *p-i-n* diode sample were high background counts. In the experiment, the background was partially suppressed by measuring at higher diode bias voltages, which may be evidence that the background is increased by electroluminescence from the sample. An attempt to quantify the effect of electroluminescence on background counts was inconclusive, however. To increase the SBR, the cancellation of the scattered laser light needs to be improved, potentially by growing a similar *p-i-n*

diode sample with a smoother surface.

For both samples, the exciton plateau was mapped and the Stark shift in RF was calculated. For the QD in a *p-i-n* diode a power dependence of RF counts and background was presented, and a simulated dependence in the absence of charge noise was obtained for comparison. The RF detuning spectrum linewidth (≈ 55 μeV) was much larger than the expected linewidth based on T_1 (≈ 0.3 μeV), most likely due to charge noise within the sample.

High-resolution RF measurements on the QD in a *p-i-n* diode sample demonstrated the presence of both coherent and incoherent photons, however the elastic peak was contaminated with background laser light. The three inelastic peaks were clearly visible in the high-resolution spectra, forming the Mollow triplet, and confirming RF of a two-level system. The inelastic side peaks moved further apart at higher powers. The distance between the peaks (Rabi frequency) was found to be linearly dependent on the square root of resonant excitation power. Finally, the measured central inelastic peak width demonstrated that pure dephasing in the system was negligible, indicating that the coherence of RF photons is significantly improved compared with photons generated non-resonantly. This opens up possibilities for resonant generation of photons at telecommunication wavelengths with improved indistinguishability.

The main problem encountered during measurements on the QD within the intrinsic region of a *p-i-n* diode, apart from low SBR, was the disappearance of RF at low excitation laser powers. To avoid this, it was necessary to work at higher powers, where the SBR was generally lower.

PL emission under 1064 nm excitation into a higher energy state was found to be much brighter than when exciting with a 830 nm laser diode for QDs in a *p-i-n* diode. Excitation with $\lambda = 1064$ nm may provide increased emission intensity from QDs in a MISFET structure as well, potentially solving some of the problems related to low signal intensity that were encountered during telecom PL measurements described in Chapter 3, particularly during the Voigt geometry experiment.

Some proposed changes to the experimental set up are the following: polarization control (fiber paddles, or a combination of a linear polarizer and a quarter-wave plate) for the high-resolution measurements in order to remove birefringence caused by the FPI the more easily, and more efficient single photon detectors.

4.4 References

[1] C. Santori, D. Fattal, J. Vuckovic, G. S. Solomon, and Y. Yamamoto, Single-photon generation with InAs quantum dots, *New Journal of Physics*, **6**, 89 (2004).

[2] M. B. Ward, M. C. Dean, R. M. Stevenson, A. J. Bennett, D. J. P. Ellis, K. Cooper, I. Farrer, C. A. Nicoll, D. A. Ritchie, and A. J. Shields, Coherent dynamics of a telecom-wavelength entangled photon source, *Nature Communications*, **5**, 3316 (2014).

[3] P. A. Dalgarno, J. McFarlane, D. Brunner, R. W. Lambert, B. D. Gerardot, R. J. Warburton, K. Karrai, A. Badolato, and P. M. Petroff, Hole recapture limited single photon generation from a single n-type charge-tunable quantum dot, *Applied Physics Letters*, **92**, 193103 (2008).

[4] S. Seidl, M. Kroner, P. A. Dalgarno, A. Högele, J. M. Smith, M. Ediger, B. D. Gerardot, J. M. Garcia, P. M. Petroff, K. Karrai, and R. J. Warburton, Absorption and photoluminescence spectroscopy on a single self-assembled charge-tunable quantum dot, *Physical Review B*, **72**, 195339 (2005).

[5] A. N. Vamivakas and M. Atature, Photons and (artificial) atoms: an overview of optical spectroscopy techniques on quantum dots, *Contemporary Physics*, **51**, 17 (2010).

[6] J. Houel, A. V. Kuhlmann, L. Greuter, F. Xue, M. Poggio, B. D. Gerardot, P. A. Dalgarno, A. Badolato, P. M. Petroff, A. Ludwig, D. Reuter, A. D. Wieck, and R. J. Warburton, Probing single-charge fluctuations at a interface using laser spectroscopy on a nearby InGaAs quantum dot, *Physical Review Letters*, **108**, 107401 (2012).

[7] A. V. Kuhlmann, J. Houel, A. Ludwig, L. Greuter, D. Reuter, A. D. Wieck, M. Poggio, and R. J.Warburton, Charge noise and spin noise in a semiconductor quantum device, *Nature Physics*, **9**, 570 (2013).

[8] T. S. Santana, Resonance fluorescence of self-assembled quantum dots, *PhD thesis*, (2016).

Chapter 5

Characterization of WSe_2 monolayer quantum emitters

In this chapter, the characterization of several bright and spectrally isolated emitters in a WSe_2 monolayer sample at 4 K under non-resonant excitation is presented. Multilayer WSe_2 structures are characterized by low intensity emission due to their indirect band gap [1, 2], while WSe_2 monolayers have a direct band gap and, consequently, a bright emission signal [1]. Therefore, WSe_2 monolayers are of particular interest. This work was particularly important as part of the preparation for a resonance fluorescence (RF) experiment on localized emitters in WSe_2, which will be described in Chapter 6. A key requirement for an emitter candidate for RF is an emission wavelength above 753 nm, since that is the lower wavelength limit of the resonant laser.

In this chapter, the polarization dependence of the signal collected from a number of emitters under non-resonant excitation was analyzed with the following objectives in mind. The first objective is to identify the exciton type. Trions are a spin singlet state and are expected to have linearly polarized emission, while neutral excitons are typically characterized by linearly polarized doublet emission with a fine-structure splitting (FSS) due to electron-hole exchange interaction. The second goal is to gather statistics on the FSS of neutral excitons to help determine whether it is possible to tune the FSS value to zero in order to create pairs of indistinguishable photons using the biexciton cascade. Additionally, an attempt to identify a neutral exciton and biexciton pair localized on the same defect was made. Finally, second-order correlation function measurements were performed to demonstrate the

quantum nature of an emitter in a WSe_2 monolayer.

The sample used for measurements described in this chapter is the 'Cairntoul' WSe_2 monolayer sample prepared via the viscoelastic stamping method by Artur Branny and described in Section 2.1.7. The monolayer was positioned on a gold-covered $[Pb(Mg_{1/3}Nb_{2/3})O_3]_{0.72}$-$[PbTiO_3]_{0.28}$ (PMN-PT) substrate, which had its top and bottom electrodes grounded to prevent charge build-up. Part of the monolayer was located on a boron nitride layer positioned on top of the gold. The sample was robust, showing the sample emitter lines over several cool-down cycles. In this chapter emitters were characterized using non-resonant excitation provided by a 532 nm wavelength continuous wave (cw) laser. Emitter microphotoluminescence (μ-PL) was analyzed either with a grating spectrometer or a single-photon avalanche diode (SPAD). White light imaging was used to align the confocal microscope system on the flakes. All measurements were performed with the sample in vacuum and cooled down to 4 K.

5.1 Spatial mapping of monolayer flakes

PL spectra of the monolayer flakes taken under non-resonant excitation are characterized by sharp peak emission in the 720 nm to 800 nm wavelength range. For this experiment bright isolated emitters were of particular interest, so in order to investigate the spatial character of the monolayer sample emission, a spatial map of the PL signal was collected and analyzed. The high power (17 μW) low-resolution (scanner step size 300 nm) spatial map shows the integrated signal of raw PL in the $680 - 850$ nm wavelength region (see Fig. 5.1(a)). Four monolayer flakes were identified on the sample, two of which (flake *3* and flake *4*) were located on the boron nitride/gold interface, flake *2* - on the edge of the boron nitride layer, and flake *1*, which turned out to be best suited for finding bright isolated emitters, entirely on the boron nitride layer. Due to the two-dimensional nature of the WSe_2 monolayers, the substrate is expected to have a significant effect on quantum emission. Sheets of hexagonal boron nitride are a disorder-free substrate that have been shown to decrease spectral wandering of the emitter transitions by minimizing non-radiative energy relaxation pathways [3].

It has been shown that localized strain pockets lead to isolated single emitters [4]. In this experiment, the local strain field was characterized using the emission wave-

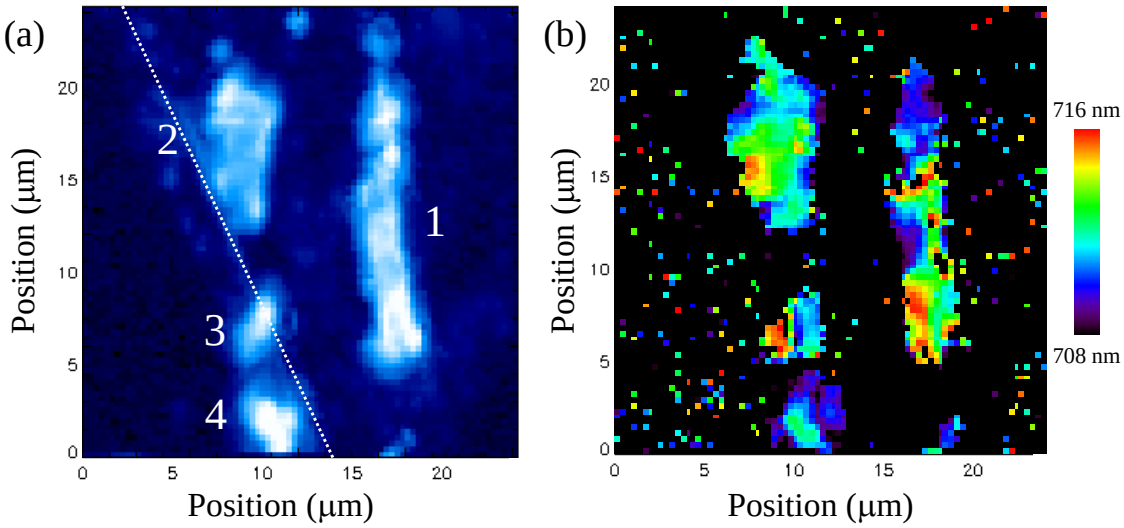

Figure 5.1: Spatial maps of the 'Cairntoul' WSe_2 sample taken at a high excitation power, showing four monolayer flakes. (a) The integrated intensity of the collected PL signal in the $680 - 850$ nm wavelength region. The bright regions correspond to the WSe_2 monolayer flakes, labeled *1* through *4*. The dashed line to the left of flake *2* marks the edge of the boron nitride layer. (b) The peak wavelength of the 2D free exciton characterizing the local strain in the monolayers. Red corresponds to 2D-X peak wavelengths of 716 nm (higher strain), and black correlates to peak wavelengths of 708 nm (weaker strain). The program used to plot spatial maps in this thesis was developed by Prof Dr Armando Rastelli, Linz University.

length of the 2D free neutral exciton (2D-X) (see Fig. 5.1(b)). Visible only at higher excitation powers, two-dimensional emission was primarily found at wavelengths below 720 nm, while comb-like emission from excitons localized on defects (0D-X) was observed at wavelengths above 720 nm at a much wider range of non-resonant laser powers. On the map longer (shorter) 2D-X peak wavelengths correspond to red (black) colored areas and higher (weaker) local strain.

In the experiment it was found that the emitters on flake *2* were neither well isolated nor very bright. The emitters on flake *4* were particularly bright, as can be determined from Fig. 5.1(a), but they were found to experience very strong jitter, leading to large linewidth broadening and spectral fluctuations over time. Emitter PL from flake *3* was found to have intense jitter as well. Nonetheless, several bright, spectrally isolated, and spatially resolved emitters were found on flake *1*. The stability of emitters on this flake is likely a consequence of its location on the boron nitride layer.

Fig. 5.2(a) shows a 6 by 24 μm^2 low power (3.5 μW) spatial map (scanner step size 150 nm) of the integrated intensity in the $720 - 750$ nm wavelength region of flake *1*. Bright points on the map correspond to spatially localized bright emitters or groups of emitters in the corresponding wavelength range. In this case the localized emitters efficiently capture the electron-hole pairs and PL emission from the 2D excitons is not visible.

Of all the bright flake *1* emitters (see Fig. 5.2(b)), P4, while not the brightest, had a sufficient emission wavelength ($\lambda = 787.02$ nm) and was identified as the best candidate for the RF experiment. For non-resonant PL, on the other hand, emitter P3 at $\lambda = 735.9$ nm was interesting due to its almost complete spectral isolation on the full range of the low resolution grating of the spectrometer.

For this sample the emitter PL peak full width at half maximum (FWHM) is normally around 200 μeV, with emitter P3 linewidth being slightly broader than usual (302 ± 27 μeV). The narrowest 0D-X linewidths recorded with this experimental set up on a different WSe_2 monolayer sample were less than 100 μeV. The most probable source of line broadening compared to previous experiments is more intense spectral fluctuations in this sample. Fig. 5.3 gives a map of a series of spectra taken at 600 nW non-resonant excitation with 0.1 s acquisition time, demonstrating the random shift of localized emitter energy over time, leading to a broadening of a PL signal collected over longer timescales. The most probable source of spectral fluc-

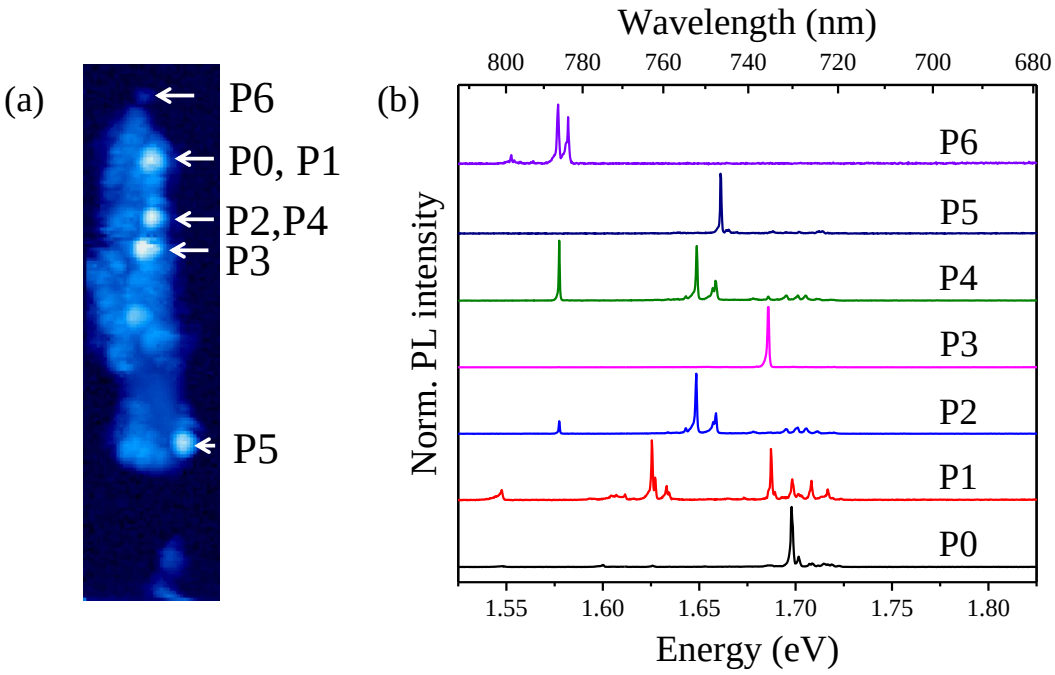

Figure 5.2: (a) A 6 μm by 24 μm high-resolution PL map of flake *1*, showing the integrated intensity of the collected signal in the $720 - 750$ nm wavelength region. The white spots on the map correspond to emitters in the monolayer, the brightest of which are labeled. (b) PL spectra of the brightest emitters on flake *1* measured at 4 K. Emitter P3 was chosen for the non-resonant excitation experiment due to its spectral and spatial isolation. Emitter P4 was identified as the best candidate for the RF experiment.

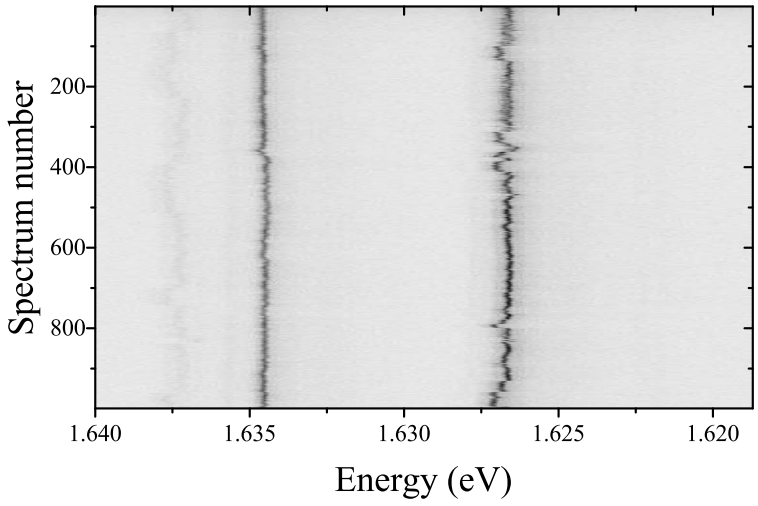

Figure 5.3: A map showing a series of emitter PL spectra taken every 0.1 s with a non-resonant excitation power of 600 nW demonstrating 0D-X spectral fluctuations over time.

tuations is the changing environment surrounding the emitter, which influences the dipole via the quantum confined Stark effect [5]. Since the gold electrode beneath the surface of the flake is grounded, we can eliminate charge build-up on the surface as a source of jitter. Ref. [6] reports on the dependence of InAs quantum dot (QD) emission linewidth on the distance from the sample surface. Linewidth broadening, likely caused by spectral diffusion, was found to be characteristic of QDs located less than 40 nm from the surface. Based on this, a capping layer atop the WSe_2 monolayer may decrease the effect of spectral fluctuations on emission linewidth.

5.2 Polarization dependent photoluminescence

The polarization of light collected from bright localized emitters on flake *1* of the WSe_2 monolayer sample was analyzed using a modified confocal microscope head. This included a rotatable Meadowlark Optics liquid crystal variable retarder acting as a half-wave plate (HWP) (see Section 2.2.10), a fixed quarter-wave plate (QWP), and a fixed linear polarizer (LP) in the collection arm.

Fig. 5.4 gives the polarization maps of emitters P0-P5, showing the intensity of emitter PL as a function of the HWP angle (vertical axis). Emitters P2-P5 are characterized by a single linearly polarized peak and likely originate from trions. Emitter P0 consists of two linearly polarized components of unequal intensity separated by a FSS equal to 713 ± 2 μeV, suggesting neutral exciton emission. For emitter P0 the angle between polarization directions of the doublet lines is $95^\circ \pm 4^\circ$ (see Fig. 5.5(a)), showing slight non-orthogonality. Local strain in the monolayer (see Fig. 5.1(b)) may be the cause of the observed unequal emission intensity and polarization direction non-orthogonality of the doublet lines. A similar effect is observed in GaAs/AlGaAs QDs in membranes, where anisotropic static stress caused by a mismatch of material lattice constants at lower temperatures can cause non-orthogonality in polarization directions and unequal emission intensity of linearly polarized components of a neutral exciton [7]. Emission from emitter P1 consists of two linearly polarized lines shifted in energy by 341 ± 3 μeV. The angle between polarization directions of emitter P1 lines is about 17° (see Fig. 5.5(b)). While significantly different from P0 parameters, the most likely source of P1 emission is a neutral exciton, as well.

Fig. 5.6 is a histogram showing the range of FSS of a number of emitters in

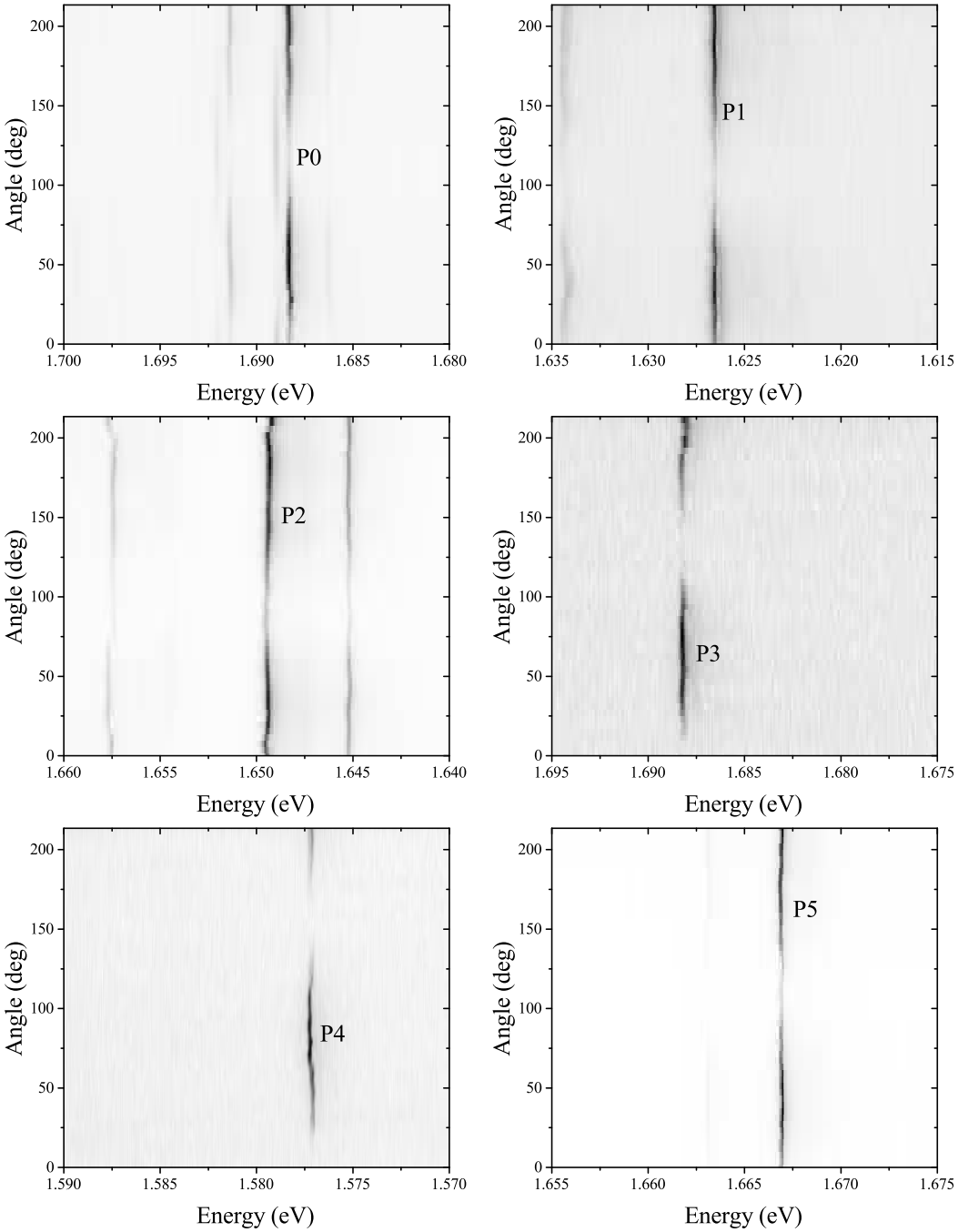

Figure 5.4: Polarization maps of bright emitters P0-P5 on flake *1* of the WSe_2 monolayer under non-resonant excitation. The vertical axis gives the relative angle of the half-wave plate in the collection arm of the confocal microscope. Lines P2-P5 are linearly polarized, suggesting trion emission. P0 and P1 emission consists of two linearly polarized lines with energy separation equal to 713 ± 2 μeV and 341 ± 3 μeV, respectively.

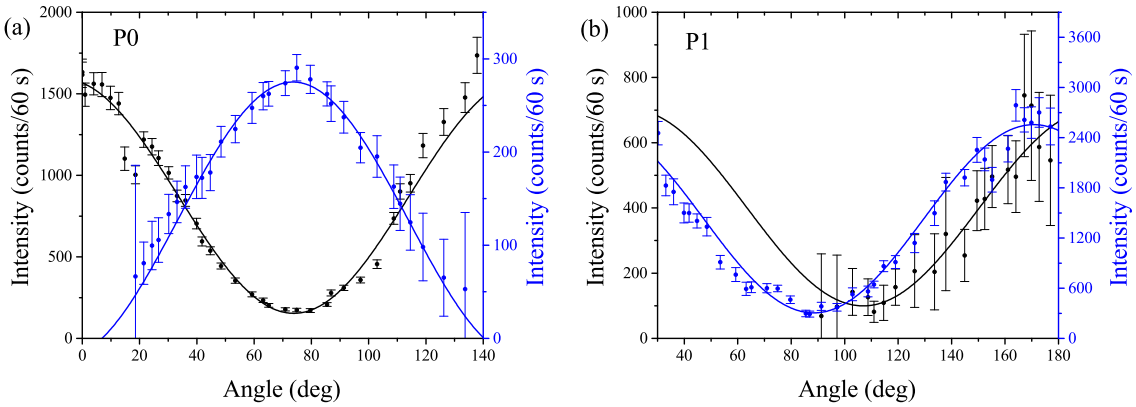

Figure 5.5: Data extracted from the polarization map of emission from bright isolated emitters P0 (a) and P1 (b) in Fig. 5.4. The horizontal axis gives the relative angle of the half-wave plate in the collection arm of the confocal microscope. The black and blue dots give the intensity of the two linearly polarized lines of the PL signal, and the solid lines are sine function fits. For each line the polarization direction is determined from the angle of maximum intensity. The difference of these values for the two linearly polarized lines is $95° \pm 4°$ (emitter P0) and about 17° (emitter P1).

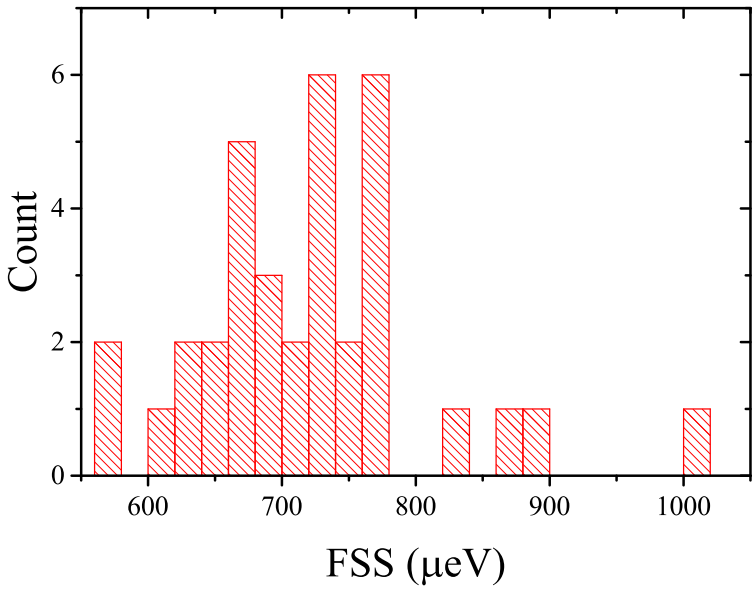

Figure 5.6: A histogram showing the range of FSS for several neutral excitons with near orthogonal polarization directions of the linearly polarized doublet lines.

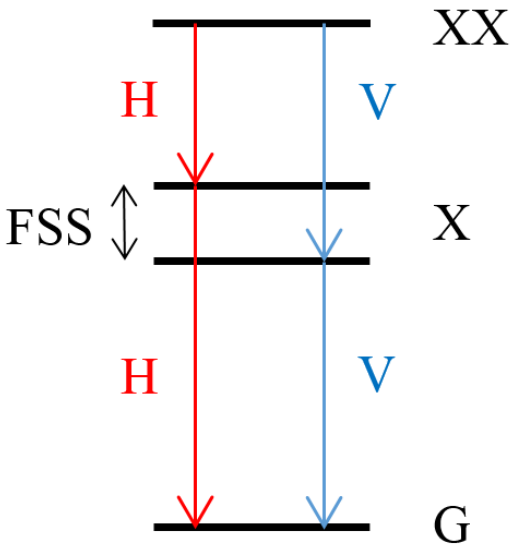

Figure 5.7: A schematic of a biexciton cascade, demonstrating that a biexciton (XX) and neutral exciton (X) pair have the same FSS, but opposite polarization phases. In the schematic the higher energy component of the biexciton (neutral exciton) is V (H) polarized.

a WSe_2 monolayer. For this measurement excitons with doublet line polarization direction close to orthogonal were chosen. The emission energy of the studied doublets, which are likely neutral excitons, were in the range of 1.65 to 1.72 eV. No clear dependence of FSS magnitude on emission energy was observed.

5.2.1 Search for an neutral exciton and biexciton pair

An attempt was made to find a neutral exciton and biexciton pair localized on the same defect in a WSe_2 monolayer. Biexciton emission consists of a linearly polarized doublet, similar to neutral excitons, but the following differences can be observed. The power dependence in logarithmic scale of the neutral exciton is linear, while a biexciton follows a quadratic power law because two electron-hole pairs need to be captured by the localized potential. The FSS of a neutral exciton and a biexciton that form a pair should be equal, and their phases opposite (see Fig. 5.7). The spectral wandering due to jitter that the two lines experience is expected to be the same, since they are localized on the same defect. A cross-correlation measurement between a neutral exciton and a biexciton from one emitter should have an asymmetric form [8]. Bunching occurs when a biexciton decay is registered followed by a neutral exciton decay, since in a cascade the latter closely follows the former. The

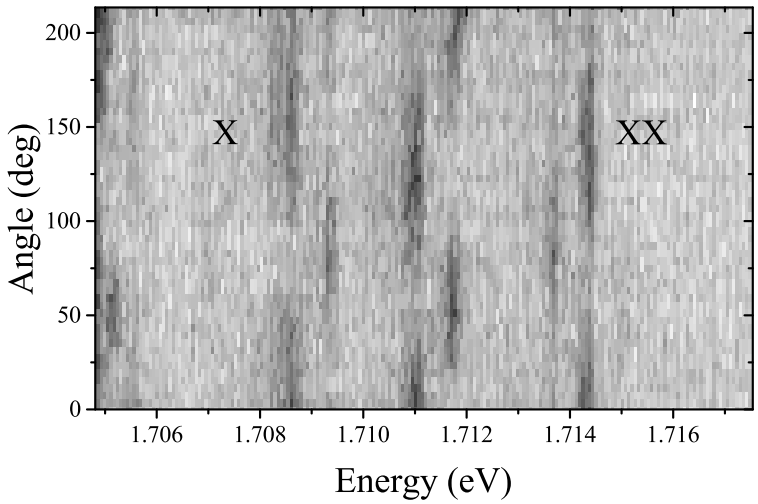

Figure 5.8: A polarization map showing a neutral exciton (X) with emission energy equal to ≈1.709 eV and possibly a biexciton (XX) with emission energy equal to ≈1.714 eV localized on the same defect.

opposite case results in antibunching. Finally, a neutral exciton and a biexciton from the same emitter should be localized at the same point in a PL map, but be separate in energy.

A large number of polarization maps were taken and analyzed for the presence of a neutral exciton and biexciton pair. The most likely candidate is shown on the polarization map in Fig. 5.8. The doublet at ≈1.709 eV is probably a neutral exciton because its phase is similar to that of the majority of doublet lines that were observed from emitters in this sample, most of which are likely to be neutral excitons. The doublet at ≈1.714 eV has a phase opposite to that of the exciton at ≈1.709 eV (see Fig. 5.9), and could conceivably be a biexciton. The FSS of the neutral exciton and the possible biexciton is 763 ± 11 μeV and 731 ± 8 μeV, respectively. The biexciton binding energy in this case would be $E_b = E_X - E_{XX} = -5.20 \pm 0.01$ meV, indicating that the neutral exciton state is more energetically favorable than the biexciton state. While a negative binding energy appears somewhat counterintuitive, there have been reports on negative biexciton binding energies in QDs. Lateral size and, consequently, carrier confinement in GaN QDs was reported to strongly affect the biexciton binding energy, with measured E_b values ranging from -6 meV to 6 meV in Ref. [9]. On the other hand, while evidence of both negative and positive biexciton binding energies in InGaAs/GaAs QDs was presented in Ref. [10], no dependence on QD size was reported. The difficulty of observing a localized biexciton in a WSe_2 monolayer may be a consequence of negative biexciton binding energies.

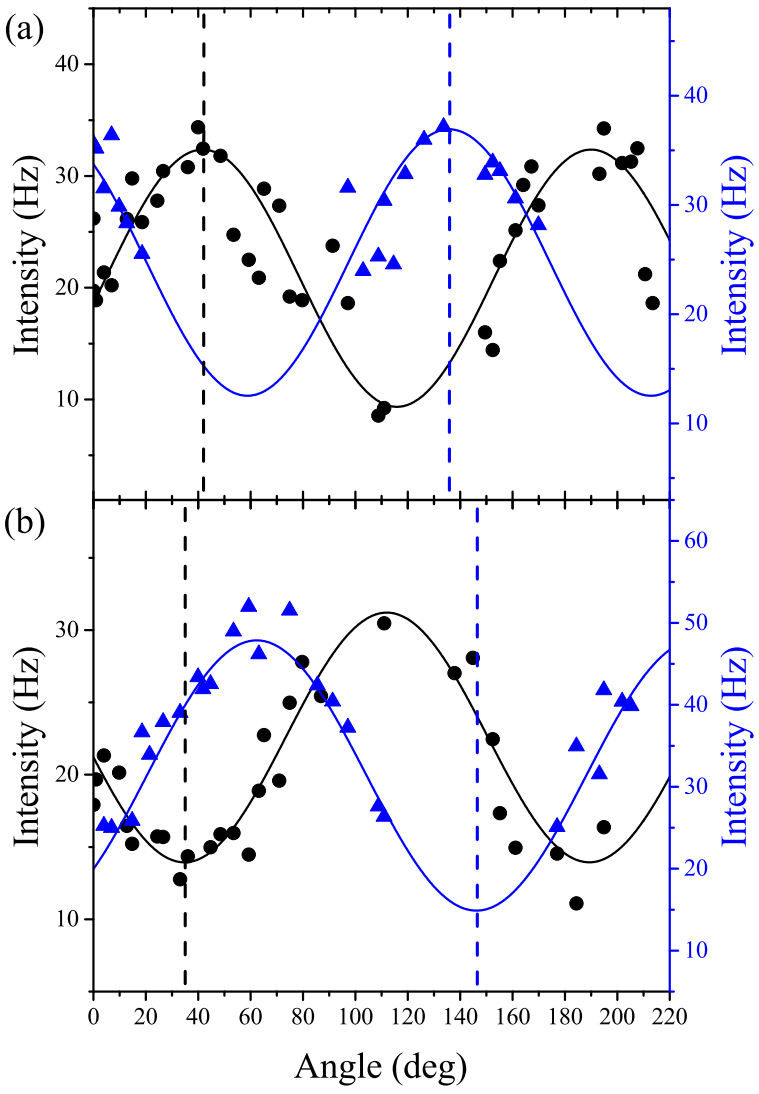

Figure 5.9: Data extracted from the polarization map in Fig. 5.8 for the neutral exciton (≈1.709 eV) (a) and possible biexciton (≈1.714 eV) (b). The horizontal axis gives the relative angle of the half-wave plate in the collection arm of the confocal microscope. The black and blue dots give the intensity of the linearly polarized lower and higher energy lines of the PL signal, respectively. The solid lines are sine function fits.

Unfortunately, due to poor signal cross-correlation measurements on this pair of lines could not be performed.

5.3 Characterization of a bright isolated emitter in a WSe_2 monolayer

Emitter P3 was demonstrated to be spectrally isolated in Fig. 5.2(b). Fig. 5.10 shows a high-resolution PL spectrum of emitter P3. The measurement was taken at a low power (0.2 nW) in order to limit the width of the PL peak, which broadens at higher powers due to increased jitter. The spectrum shows that emitter PL is composed of the zero-phonon line (ZPL) and a lower energy phonon sideband (PSB). The ratio of integrated intensities of the ZPL to the PSB for this measurement is 64:36.

Fig. 5.11(a) shows a high resolution (scanner step size 100 nm) spatial map of the integrated intensity for emitter P3 PL. From the vertical and horizontal linecuts shown in Fig. 5.11(b) it can be seen that the spatial resolution of emitter P3 is nearly diffraction limited, confirming that the system is well-aligned and the emission is highly localized. The spectral and spacial isolation of emitter P3 opened up the possibility of an attempt to show photon antibunching without the use of filtering on the collected signal.

5.3.1 Power dependence

Fig. 5.12 shows the integrated intensity of the P3 emitter PL peak as a function of non-resonant excitation laser power (P_{exc}). The red solid curve is a fit describing a two-level system under non-resonant excitation:

$$I = I_{sat} \times \frac{P_{exc}}{P_{exc} + P_{1/2}}; \tag{1}$$

where $P_{1/2} = 19 \pm 2$ nW is the excitation power at which the integrated intensity is half of its value at saturation ($I_{sat} = 158 \pm 7$ kHz). At saturation SPAD count rates of 3 MHz are reached.

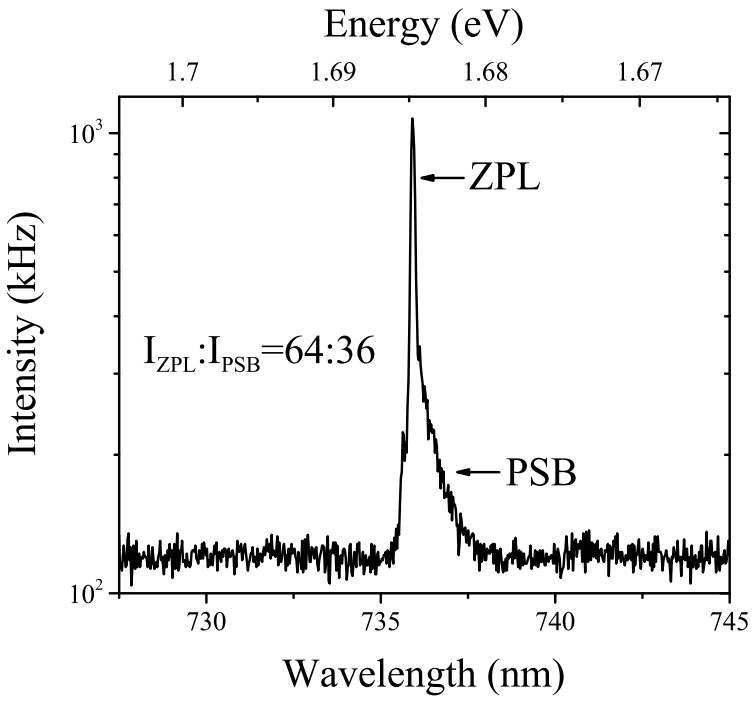

Figure 5.10: A low excitation power (0.2 nW) PL spectrum of emitter P3 on flake *1*. The spectrum has two components: a zero-phonon line and phonon sideband at lower energies. The ratio of the integrated intensities of the ZPL to the PSB is approximately 64:36.

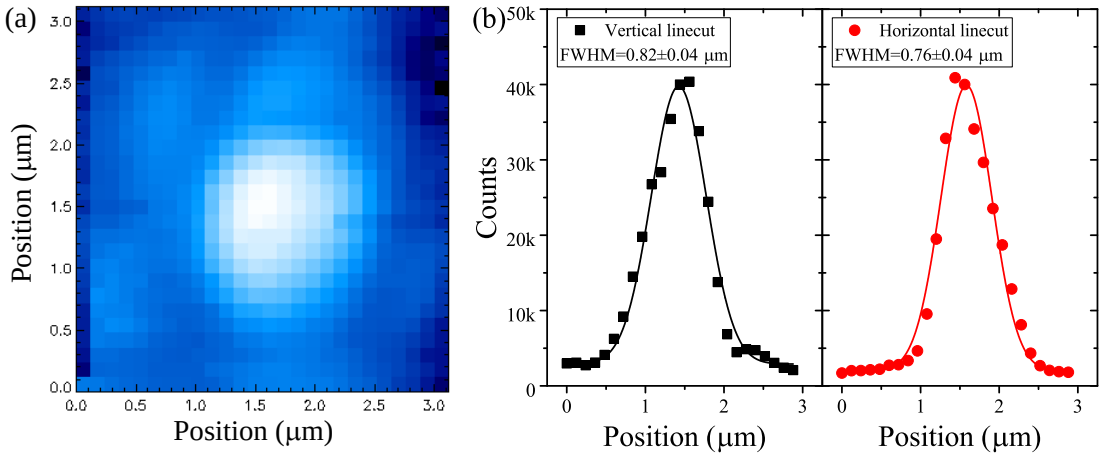

Figure 5.11: (a) High resolution spatial map of the integrated intensity for the emitter P3 PL signal. (b) Vertical and horizontal linecuts of the spatial map showing the spatial resolution of the emitter, which is close to the resolution of the confocal microscope system.

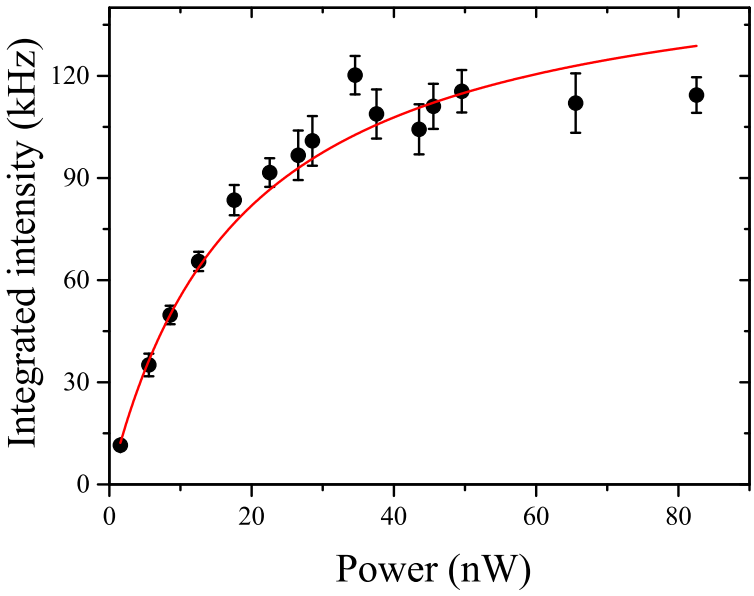

Figure 5.12: Excitation power dependence of the integrated intensity of the emitter P3 PL signal. The red curve is a fit using Eq. 1.

5.3.2 Photon antibunching

A measurement of the second-order correlation function was performed to investigate the quantum nature of bright isolated emitter P3. To measure the normalized second order correlation function ($g^{(2)}$(t)) under non-resonant cw excitation at 2 nW the signal collected from the emitter was passed through a tunable angle-dependent edge filter system described in Section 2.2.17 and an in-fiber Hanbury-Brown and Twiss interferometer before being directed to the SPADs. The filter FWHM was 4 nm for this experiment. Data analysis using the Bayesian approach was carried out by Guillem Ballesteros-Garcia. In the Bayesian approach modeling parameters are seen as variables and are assigned a probability distribution, referred to as the prior, while the measured data is expressed as likelihood. The two are combined into the posterior probability distribution, which is then optimized to obtain the most probable parameters. The Bayesian method is intuitive and allows to take into account both data and prior information. The obtained histogram of coincidence counts is given in Fig. 5.13(a) by solid black circles. The solid red curve is the best fit to the measured data, given by a convolution of the Gaussian function, representing the system response function, with the following relation:

$$g^{(2)}(t) = 1 - \rho^2 e^{\frac{-|t|}{\tau}}; \tag{2}$$

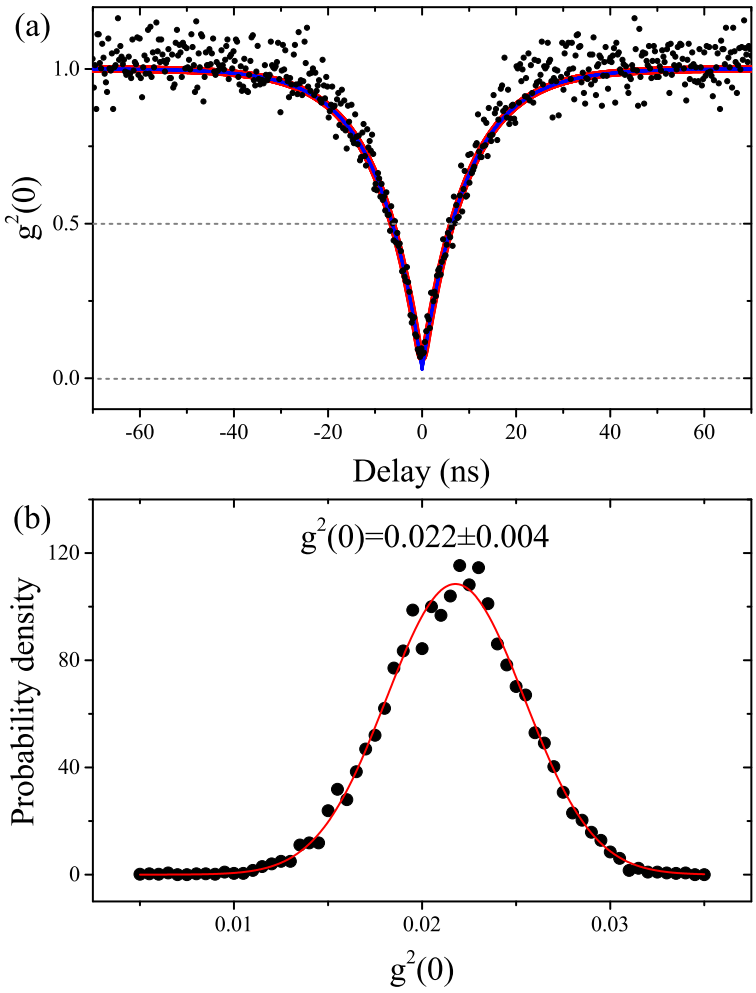

Figure 5.13: (a) Normalized second-order correlation function of bright isolated emitter P3 under 2 nW non-resonant cw excitation. Time bin size is 256 ps. The solid red curve is the best fit to the measured data using a convolved Eq. 2. The blue curve is the calculated deconvolved $g^{(2)}(t)$. (b) The probability density distribution of calculated deconvolved $g^{(2)}(0)$ values, the solid red curve is a Gaussian fit used to extract the deconvolved most probable value of $g^{(2)}(0) = 0.022 \pm 0.004$.

Here ρ accounts for non-zero background, τ is the decay time of the emitter, equal to the emitter lifetime under low power, and t is the time delay between coincidences. Convolution of the second order correlation function with the system response function allows us to take into account the instrument response time (0.5 ns per channel). The parameters extracted from the fit are used to calculate the deconvolved $g^{(2)}(t)$, given in Fig. 5.13(a) by the blue curve.

Fig. 5.13(b) gives the probability density distribution of deconvolved $g^{(2)}(0)$ values calculated using the probabilistic values of the fitted parameters. The most probable deconvolved value of coincidence counts at time zero and its standard deviation are extracted from this plot and are equal to $g^{(2)}(0) = 0.022 \pm 0.004$. This value demonstrates that photon emission is antibunched, which is conclusive proof that spatially isolated emitters in 2D WSe_2 structures are quantum in nature and are sources of single photons of high purity. The signal-to-background ratio is given by SBR$=\rho/(1-\rho)$, and reaches a value of 70.4 ± 0.2. The measured lifetime is equal to 9.6 ± 0.1 ns. Without the filter, a non-deconvolved $g^{(2)}(0) = 0.35 \pm 0.02$ was obtained.

5.4 Discussion and further directions

This chapter presents the results of PL experiments on emitters localized on defects in a WSe_2 monolayer at 4 K. Several particularly bright spectrally and spatially isolated emitters were identified and their polarization dependence was characterized. These results set the stage for a first attempt at resonantly exciting emitters in a two-dimensional structure, which will be described in Chapter 6.

Single quantum emitters in WSe_2 monolayers can be divided into several groups. In the first group are emitters with a FSS of 600 to 800 μeV and large g-factors that were reported in [4, 11–14]. The doublet lines of these emitters are nearly orthogonally polarized, suggesting that emission originates from neutral excitons. Emitter P0 belongs in this category. Strain in the monolayer appears to affect the polarization of light collected from emitter P0, leading to its doublet lines having unequal intensity, as well as changing the polarization direction between them from orthogonal. In the second group are emitters such as P1 with a FSS around 300 μeV and small g-factors. Emitters in the third group are characterized by single peak linearly polarized emission, suggesting trion emission. Emitters P2-P5 belong in this

group.

The FSS of several neutral excitons was measured and a potential candidate for a biexciton localized on a defect in a WSe_2 monolayer was observed.

Finally, second-order correlation function measurements revealed a deconvolved $g^{(2)}(0) = 0.022 \pm 0.004$, confirming the single-photon nature of emitters in WSe_2 monolayers.

5.5 References

[1] Sujay B. Desai, Gyungseon Seol, Jeong Seuk Kang, Hui Fang, Corsin Battaglia, Rehan Kapadia, Joel W. Ager, Jing Guo, and Ali Javey, Strain-induced indirect to direct bandgap transition in multilayer WSe_2, *Nano Letters*, **14**, 4592 (2014).

[2] Weijie Zhao, Zohreh Ghorannevis, Leiqiang Chu, Minglin Toh, Christian Kloc, Ping-Heng Tan, and Goki Eda, Evolution of electronic structure in atomically thin sheets of WS_2 and WSe_2, *ACS Nano*, **7**, 791 (2013).

[3] Jason S. Ross, Philip Klement, Aaron M. Jones, Nirmal J. Ghimire, Jiaqiang Yan, D. G. Mandrus, Takashi Taniguchi, Kenji Watanabe, Kenji Kitamura, Wang Yao, David H. Cobden, and Xiaodong Xu, Electrically tunable excitonic light-emitting diodes based on monolayer WSe_2 $p-n$ junctions, *Nature Nanotechnology*, **9**, 268 (2014).

[4] S. Kumar, A. Kaczmarczyk, and B. D. Gerardot, Strain-induced spatial and spectral isolation of quantum emitters in mono- and bilayer WSe_2, *Nano Letters*, **15**, 7567 (2015).

[5] Andreas V. Kuhlmann, Julien Houel, Arne Ludwig, Lukas Greuter, Dirk Reuter, Andreas D. Wieck, Martino Poggio, and Richard J. Warburton, Charge noise and spin noise in a semiconductor quantum device, *Nature Physics*, **9**, 570 (2013).

[6] C. F. Wang, A. Badolato, I. Wilson-Rae, P. M. Petroff, E. Hu, J. Urayama and A. Imamoğlu, Optical properties of single InAs quantum dots in close proximity to surfaces, *Applied Physics Letters*, **85**, 3423 (2004).

[7] S. Kumar, E. Zallo, Y. H. Liao, P. Y. Lin, R. Trotta, P. Atkinson, J. D. Plumhof, F. Ding, B. D. Gerardot, S. J. Cheng, A. Rastelli, and O. G. Schmidt, Anomalous anticrossing of neutral exciton states in GaAs/AlGaAs quantum dots, *Physical Review B*, **89**, 115309 (2014).

[8] A. Kiraz, S. Fälth, C. Becher, B. Gayral, W. V. Schoenfeld, P. M. Petroff, Lidong Zhang, E. Hu, and A. Imamoğlu, Photon correlation spectroscopy of a single quantum dot, *Physical Review B*, **65**, 161303(R) (2002).

[9] S. Amloy, K. H. Yu, K. F. Karlsson, R. Farivar, T. G. Andersson, and P. O. Holtz, Size dependent biexciton binding energies in GaN quantum dots, *Applied Physics Letters*, **99**, 251903 (2011).

[10] R. Trotta, E. Zallo, E. Magerl, O. G. Schmidt, and A. Rastelli, Independent control of exciton and biexciton energies in single quantum dots via electroelastic fields, *Physical Review B*, **88**, 155312 (2013).

[11] Yu-Ming He, Genevieve Clark, John R. Schaibley, Yu He, Ming-Cheng Chen, Yu-Jia Wei, Xing Ding, Qiang Zhang, Wang Yao, Xiaodong Xu, Chao-Yang Lu, and Jian-Wei Pan, Single quantum emitters in monolayer semiconductors, *Nature Nanotechnology*, **10**, 497 (2015).

[12] M. Koperski, K. Nogajewski, A. Arora, V. Cherkez, P. Mallet, J.-Y. Veuillen, J. Marcus, P. Kossacki, and M. Potemski, Single photon emitters in exfoliated WSe2 structures, *Nature Nanotechnology*, **10**, 503 (2015).

[13] Chitraleema Chakraborty, Laura Kinnischtzke, Kenneth M. Goodfellow, Ryan Beams, and A. Nick Vamivakas, Voltage-controlled quantum light from an atomically thin semiconductor, *Nature Nanotechnology*, **10**, 507 (2015).

[14] Ajit Srivastava, Meinrad Sidler, Adrien V. Allain, Dominik S. Lembke, Andras Kis, and A. Imamoğlu, Optically active quantum dots in monolayer WSe_2, *Nature Nanotechnology*, **10**, 491 (2015).

Chapter 6

Resonant laser spectroscopy of quantum emitters in WSe_2 monolayers

We are motivated to perform resonant laser spectroscopy of quantum emitters in WSe_2 monolayers cooled to 4 K in order to set the stage for the characterization of excitonic coherence, and spin and valley coherence of confined excitons. Spin and valley coherence can be demonstrated using polarization-resolved measurements. If the valley-dependent optical selection rules are valid (see Section 1.5.3), carriers will be pumped into a specific valley. Consequently, clockwise (counter-clockwise) circularly polarized excitation would lead to predominantly clockwise (counter-clockwise) emission. Valley-dependent optical selection rules have been demonstrated for two-dimensional emission from transition metal dichalcogenide (TMD) monolayers in microphotoluminescence (μ-PL) experiments [1–4], but have not yet been reported for quantum emitters in these materials. Resonant excitation is band-to-band, and is expected to decrease the effect of intervalley scattering, which may prove crucial in demonstrating valley-selective excitation of carriers in quantum emitters. Additionally, the experiments described in this chapter are a step towards more sophisticated experiments on emitters in WSe_2 monolayers, such as the direct preparation of the quantum state and the deterministic generation of indistinguishable single photons for applications in quantum information processing.

While the properties of excitons localized at defects in two-dimensional (2D) transition metal dichalcogenide (TMD) monolayers under non-resonant excitation

have been studied previously [5–9], coherent manipulation of excitons in this system has not been demonstrated. This chapter describes the first attempt at driving bright spatially isolated emitters in a WSe_2 monolayer resonantly by a tunable diode laser. Orthogonal linear polarizers in the excitation and collection arms of the confocal microscope were used to suppress the scattered excitation laser light, reaching a cancellation of 10^5 on a relatively rough gold coated substrate, and 10^7 on a smooth GaAs substrate. The temporal and spectral characteristics of emitters were investigated, and their quantum nature was probed through photon correlation measurements.

6.1 Resonance fluorescence

A bright isolated emitter is necessary for achieving a good signal-to-background ratio (SBR) in resonance fluorescence (RF), and emitters in two-dimensional WSe_2 monolayers fulfill that requirement, as discussed in Chapter 5. For this experiment emitters P4 and E3 on flake *1* of the 'Cairntoul' sample with emission wavelengths of 787.02 nm and 784.69 nm, respectively, were chosen.

The 'Cairntoul' WSe_2 monolayer sample, fabricated by Artur Branny and described in Section 2.1.7, can be used to tune the emission wavelength of emitters by about 10 meV by varying the bias voltage applied to the electrodes of the PMN-PT substrate. Initially strain tuning was used to tune the emission in resonance with the laser. However, it was found that tuning the emitter resulted in an uncontrollable increase in background counts due to a slight shift of the laser spot on the sample as a result of expansion or contraction of the piezoelastic material. This was confirmed by adjusting the linear polarizer and quarter-wave plate positions in the collection arm of the microscope head or by moving the sample using the scanner. Both methods lead to a reduction of background counts to the original value expected at zero bias applied to the actuator. The increase in background counts due to finite bias applied to the actuator was of the same order of magnitude as the expected signal, so this method of emitter wavelength tuning was not suited for our purposes. Instead the resonant laser was fine tuned to the emission wavelength of the emitter observed in a low power PL spectrum.

Fig. 6.1 shows a long integration time (100 s) fluorescence spectrum of emitter P4 on the high-resolution grating of the spectrometer under low power (4 μW) non-

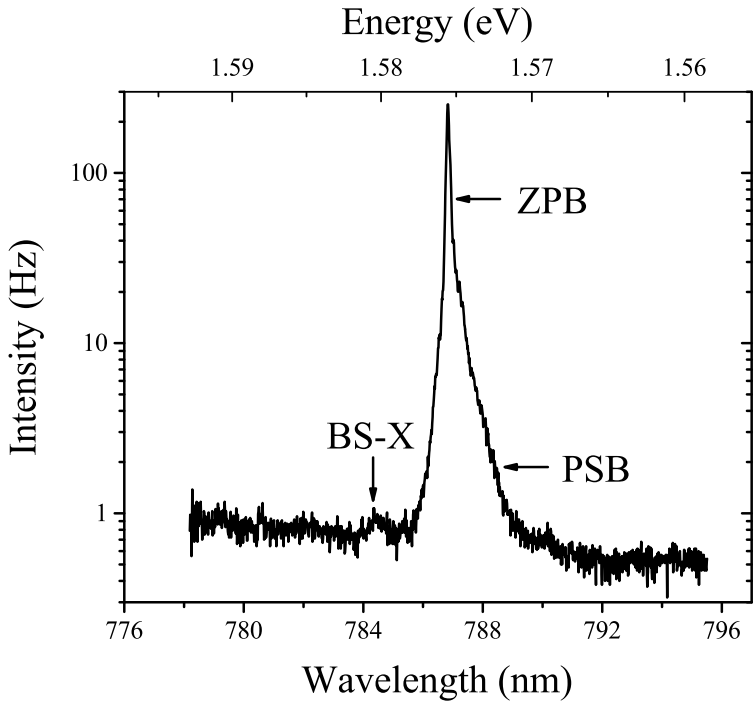

Figure 6.1: A PL spectrum on the high-resolution grating of the spectrometer showing the zero-phonon line (ZPL) and a lower energy phonon sideband (PSB) of emitter P4 located on flake *1* of the 'Cairntoul' WSe_2 monolayer sample. The spectrum also reveals the presence of a strongly suppressed blue-shifted exciton (BS-X) peak.

resonant excitation provided by a 532 nm wavelength continuous wave (cw) laser. The low power was chosen in an attempt to limit the width of the PL peak which increases at higher powers due to inhomogeneous broadening [6, 8, 9]. The main features of the spectrum are a lower energy phonon sideband (PSB) and a zero phonon line (ZPL) with a full width at half maximum (FWHM) of around 200 μeV, which is within the range of linewidths measured for emitters on this sample (see Chapter 5). The spectrum also shows a weakly-fluorescent blue-shifted exciton (BS-X) peak, which is discussed later in this chapter.

The high resolution grating of the spectrometer was used to measure the overlap of the laser peak and the emitter peak. A spectrum of the RF signal collected from emitter P4 is shown in Fig. 6.2(a). The signal is composed of a ZPL with a FWHM of about 228 μeV and a PSB. The spectral form of the signal is very similar to the emitter PL peak (see Fig. 6.1). As is shown later in this chapter, due to poor cancellation, the emitter signal is mixed with scattered laser light. For comparison, Fig. 6.2(c) shows the collected signal when the emitter is off resonance.

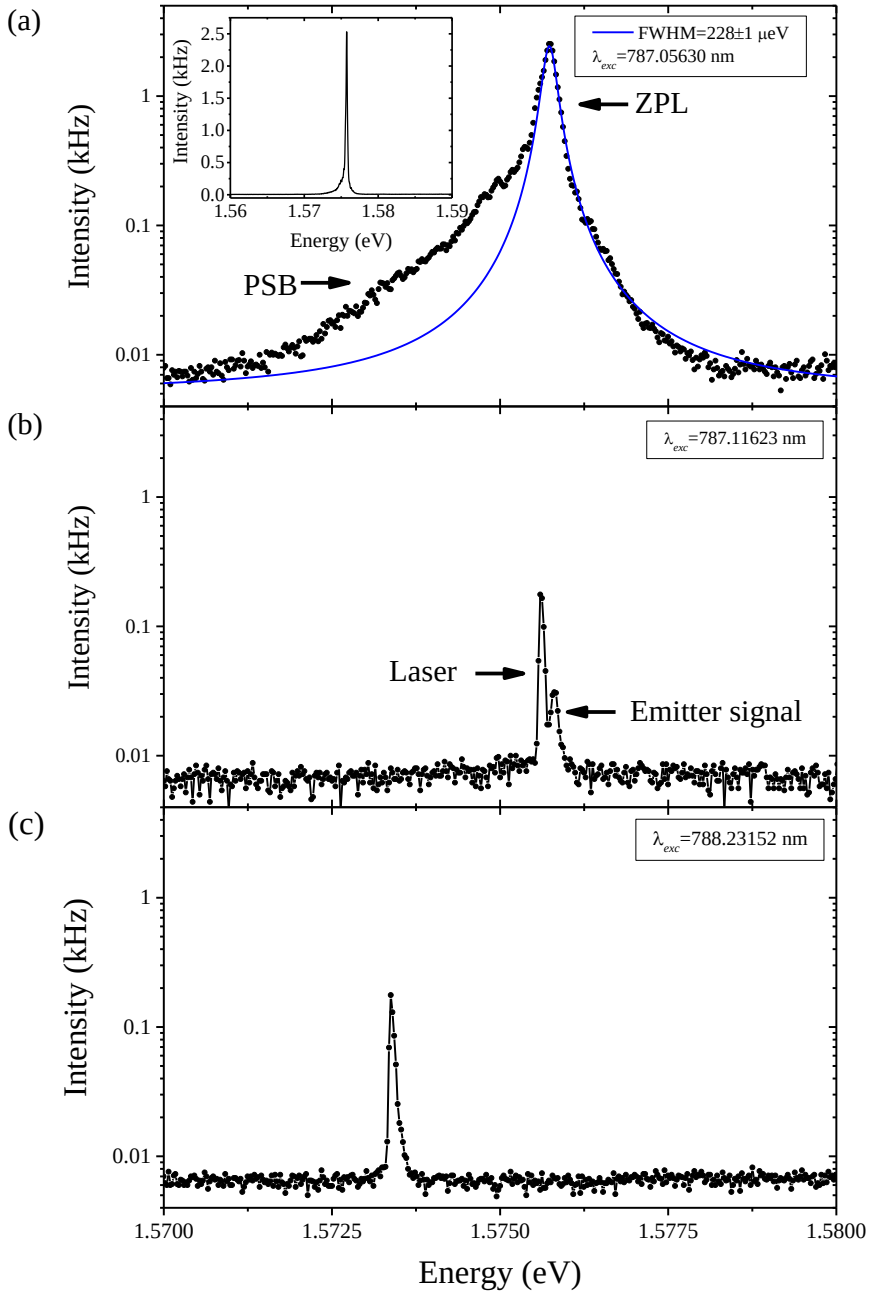

Figure 6.2: (a) RF signal collected from emitter P4 on a WSe_2 monolayer as seen on the spectrometer. The presence of a narrow high intensity ZPL and a broader low intensity PSB contributions is a sign that the excitation laser is in resonance with the emitter transition. The insert shows the collected signal with a linear intensity scale. (b) Data collected from the spectrometer when the excitation laser wavelength is close to, but not exactly on resonance. (c) Spectrum of the laser detuned from the emitter transition. All spectra were taken at a resonant laser excitation power of 600 nW with a 10 s acquisition time.

Here, a narrow high intensity peak, not accompanied by a sideband, originates from scattered laser light. Fig. 6.2(b) shows an intermediate case when the resonant laser (brighter peak) is fine-tuned 30 μeV away from the ZPL (weaker peak). When the excitation laser is sufficiently far away from resonance, the low intensity peak becomes no longer visible (Fig. 6.2(c)). When in resonance, single photon detector counts increase significantly over the background, for example with 2 μW excitation the change in detector counts is from $(2-3)\times10^4$ Hz to $(1-2)\times10^5$ Hz.

The RF signal is characterized by broader linewidths than expected. For emitter P4 the RF FWHM (228 μeV) is of the same order as the PL FWHM (200 μeV), with both being much broader than the resolution of the spectrometer grating. The broadening is attributed to spectral fluctuations on sub-millisecond timescales.

In summary, the signs we looked for to determine whether the collected signal from an emitter in a WSe_2 monolayer was RF are the following: first, the presence of a single ZPL on the spectrometer (detuning equal to zero); second, the presence of a lower energy PSB; and third, an increase of detector counts by about an order of magnitude above the background level.

6.1.1 Photon antibunching in RF

To characterize the quantum nature of emitter P4, its second-order correlation function is investigated using the Bayesian approach (see Section 5.3.2). Fig. 6.3(a) shows the experimental data (black circles) and the best fit (solid red line) calculated using a convolution of the Gaussian distribution with Eq. 2 from Chapter 5. The deconvolved $g^{(2)}(t)$ (blue line) is calculated using the parameters extracted from the best fit. The probability density distribution of $g^{(2)}(0)$ values was obtained by varying the parameters in Eq. 2 from Chapter 5. By fitting the probability density distribution (see Fig. 6.3(b)) the deconvolved most probable $g^{(2)}(0)$ value and its standard deviation equal to $g^{(2)}(0)=0.24\pm0.07$ were extracted. The lifetime extracted from the fit is equal to 3.7 ± 0.3 ns. The fitting procedure was carried out by Guillem Ballesteros-Garcia. The calculated signal-to-background ratio is about 61:10, suggesting that due to poor cancellation, the signal collected from the emitter is mixed with the laser light, decreasing single photon purity. To investigate this further Dr Santosh Kumar and Mauro Brotons-Gisbert carried out second-order correlation measurements on emitter E3 and monitored its detuning from resonance

and photon count-rate at the same time.

Using a fiber splitter, the RF signal from emitter E3 was measured simultaneously by a single-photon avalanche diode (SPAD) and a spectrometer. Fig. 6.4(a) shows a timetrace of detector counts, and Fig. 6.4(b) gives the laser detuning from resonance calculated from the data recorded on the spectrometer. The SPAD counts fluctuate between about 0.4 MHz (off resonance) and about 1.7 MHz (on resonance), giving a signal-to-background ratio of about 4.3. The measured background counts are high due to the inefficient suppression of laser light reflected off the rough surface of the sample. From Fig. 6.4, the magnitude of detuning corresponds to detector counts. The changing detuning is attributed to the shifts in emitter transition energy as a result of charge noise in the environment.

The second-order correlation function for emitter E3 was measured when the emitter transition was in resonance with the laser. Fig. 6.5(a) shows the data (black circles), the best fit (solid red line), and the calculated deconvolved fit (solid blue line). A fit of the probability density distribution of deconvolved $g^{(2)}(0)$ values (see Fig. 6.5(b)) yielded the deconvolved most probably value equal to $g^{(2)}(0)$=0.341 $\pm$ 0.007, demonstrating antibunching and confirming the quantum nature of the emitter. The lifetime was 2.87 ± 0.051 ns. The signal-to-background ratio was about 4.3, accounting for the high value of $g^{(2)}(0)$, and confirming the SBR value calculated using the maximum signal and mean background counts recorded on the SPAD (see Fig. 6.4(a)).

6.2 Photoluminescence excitation spectroscopy

To investigate the properties of quantum emitters further, photoluminescence excitation (PLE) spectroscopy is performed (see Fig. 6.6). The resonant excitation laser wavelength is manually detuned from the P4 emitter transition and emission at λ = 787.02 nm is monitored on the spectrometer. At negative detunings the signal disappears, with only the scattered laser light peak being visible in the spectrum. Next, the resonant laser is detuned towards shorter wavelengths. Spectra A and B correspond to RF from the emitter at slightly different detunings. Spectrum C corresponds to a regime where the phonon sideband is still visible, but the resonant laser peak and RF peak are no longer overlapping. When detuning the laser further towards shorter wavelengths, the peak at $\lambda = 787.02$ nm decreases in inten-

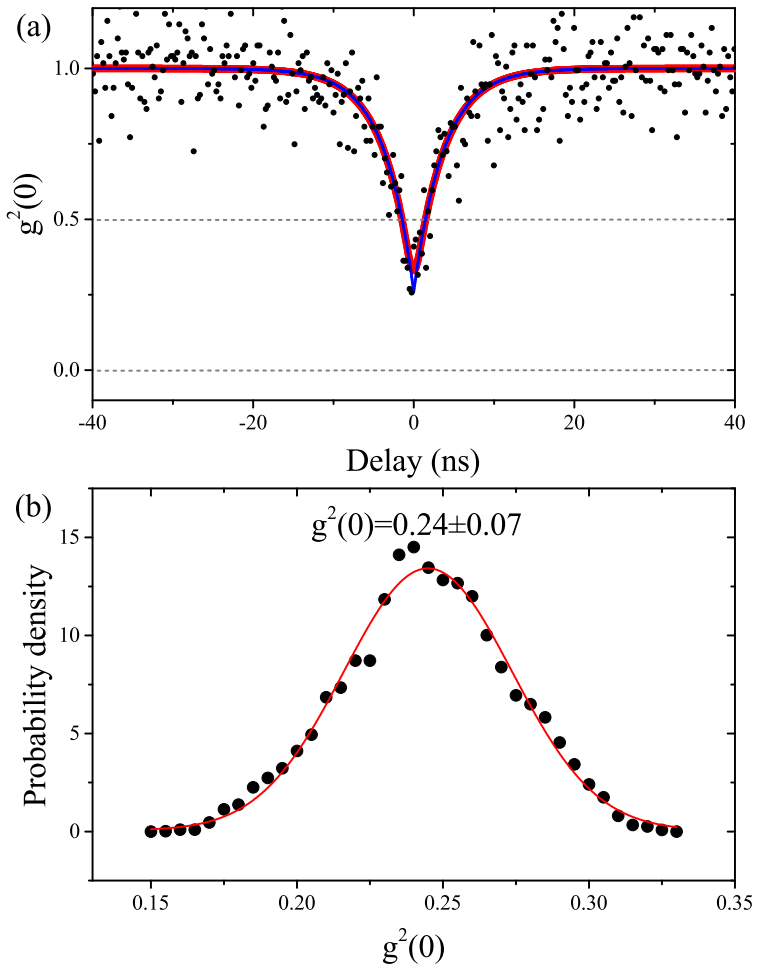

Figure 6.3: (a) Normalized second-order correlation function of bright isolated emitter P4 under 0.135 μW resonant excitation at λ = 787.01425 nm. Time bin size is 256 ps. The solid red line is the best fit to the data. The blue curve is the calculated deconvolved $g^{(2)}(t)$. (b) The probability density distribution of calculated deconvolved $g^{(2)}(0)$ values, the solid red line is a Gaussian fit used to extract the deconvolved most probable value of $g^{(2)}(0) = 0.24 \pm 0.07$.

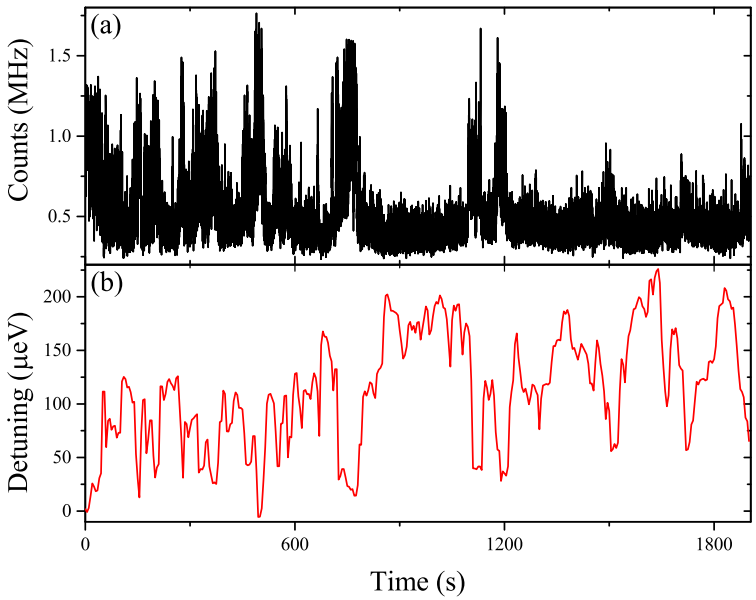

Figure 6.4: Timetraces of SPAD counts (a) and laser detuning from resonance (b) for emitter E3 measured under 1 μW excitation at a wavelength of 784.69460 nm. The acquisition times were 70 ms for the measurement on the SPAD and 5 s for the measurement on the high resolution grating of the spectrometer.

sity and eventually disappears (spectrum D). As the detuning from resonance nears about 2.4 nm (5 meV) the peak at $\lambda = 787.02$ nm goes through a sharp maximum (spectrum E). This increase in counts is the result of the excitation laser becoming resonant with a blue-shifted exciton transition (BS-X), and the subsequent relaxation of carriers to the lowest energy excitonic state, the $\lambda = 787.02$ nm wavelength transition. The PL from the blue-shifted exciton is suppressed by a factor of 1250 compared to the P4 transition (see Fig. 6.1). Further detuning results in the loss in intensity of the peak at $\lambda = 787.02$ nm (spectrum F). A summary of the integrated intensity of the $\lambda = 787.02$ nm peak as a function of detuning is given in Fig. 6.7.

Using PLE spectroscopy the scale of spectral fluctuations resultant from emitter jitter on short timescales is characterized. Fig. 6.8(a) shows the shift in PL energy of the lowest energy excitonic transition of emitter P4 with a timing resolution of 28 ms. Fig. 6.8(b) shows a histogram of the data in Fig. 6.8(a). The median transition energy for this measurement is 1.5760 ± 0.0001 eV.

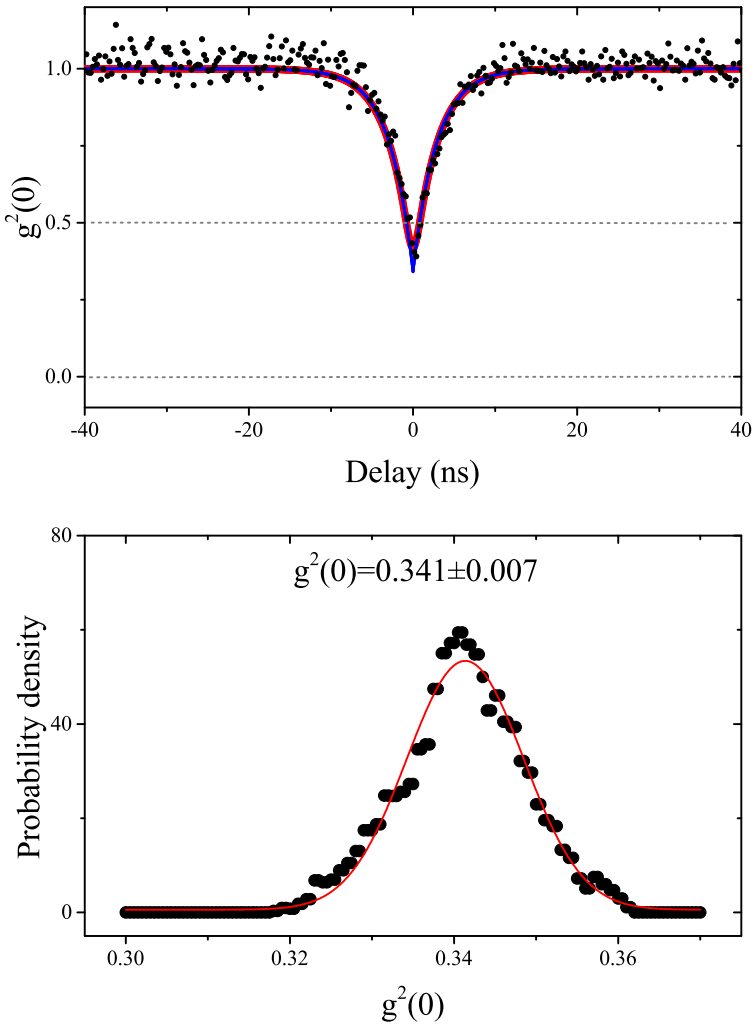

Figure 6.5: (a) Normalized second-order correlation function of bright isolated emitter E3 under 1 μW resonant excitation at $\lambda = 784.69460$ nm. Time bin size is 256 ps. The solid red (blue) line is the best fit (the calculated deconvolved fit) to the data. (b) The probability density distribution of calculated deconvolved $g^{(2)}(0)$ values, the solid red line is a Gaussian fit used to extract the deconvolved most probable value of $g^{(2)}(0) = 0.341 \pm 0.007$.

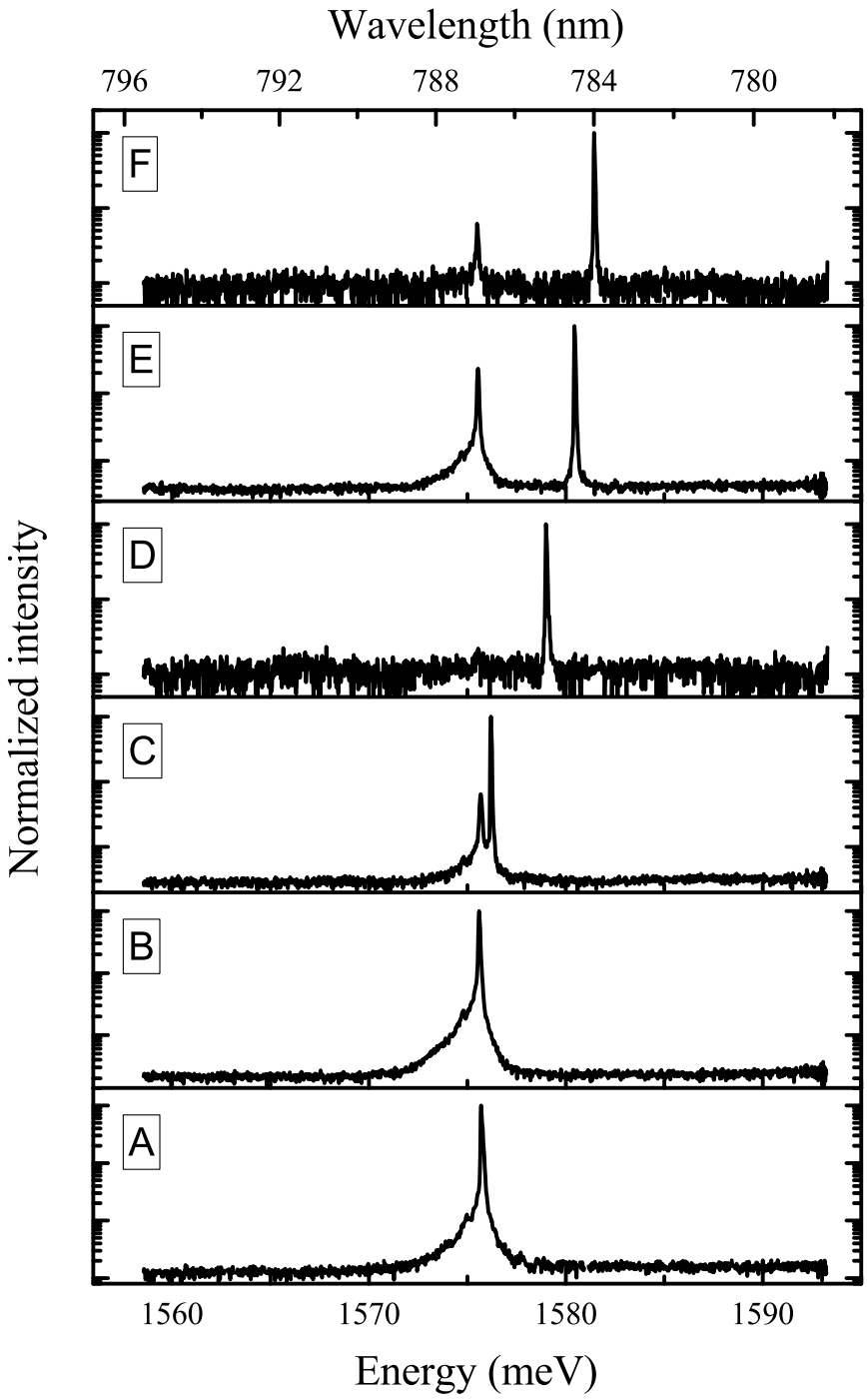

Figure 6.6: Normalized spectra of the signal collected from emitter P4 in a WSe_2 monolayer at different excitation laser detunings from resonance at $\lambda = 787.02$ nm. A and B correspond to the RF regime. Spectrum C was taken when the detuning was equal to about 0.5 meV. Spectrum D corresponds to a detuning of about 3.5 meV. Spectrum E reveals the presence of a higher energy excitonic state, which is detuned from the lowest energy excitonic state by about 5 meV, and can be used to efficiently excite the $\lambda = 787.02$ nm transition through PLE. Finally, spectrum F corresponds to a detuning of about 5.6 meV.

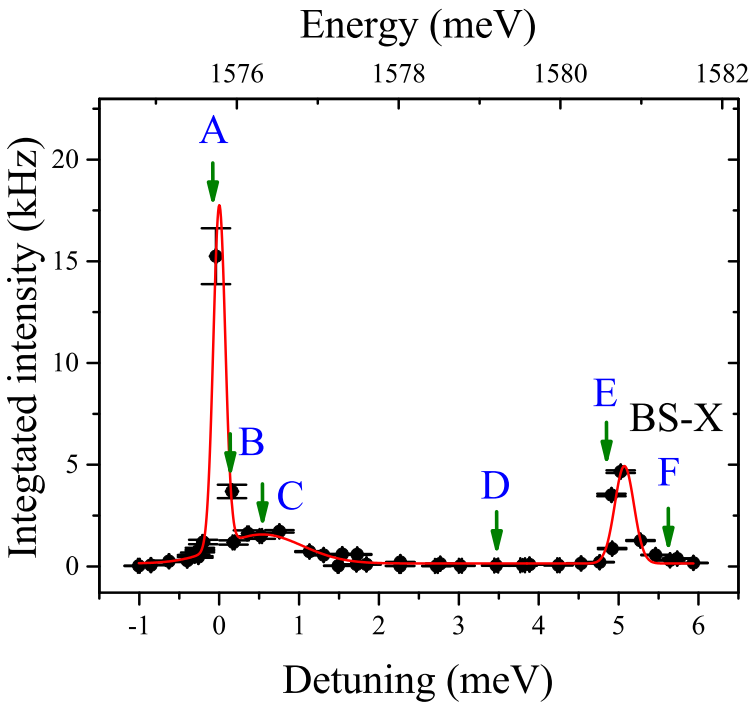

Figure 6.7: Integrated intensity of the P4 peak at λ=787.02 nm as a function of emitter detuning. The peak at zero detuning indicates RF from the emitter. A second peak at a detuning of around 5 meV suggests the existence of a higher energy excitonic state of the same emitter which can be used to excite the P4 transition through PLE. The blue labels correspond to the spectra in Fig. 6.6.

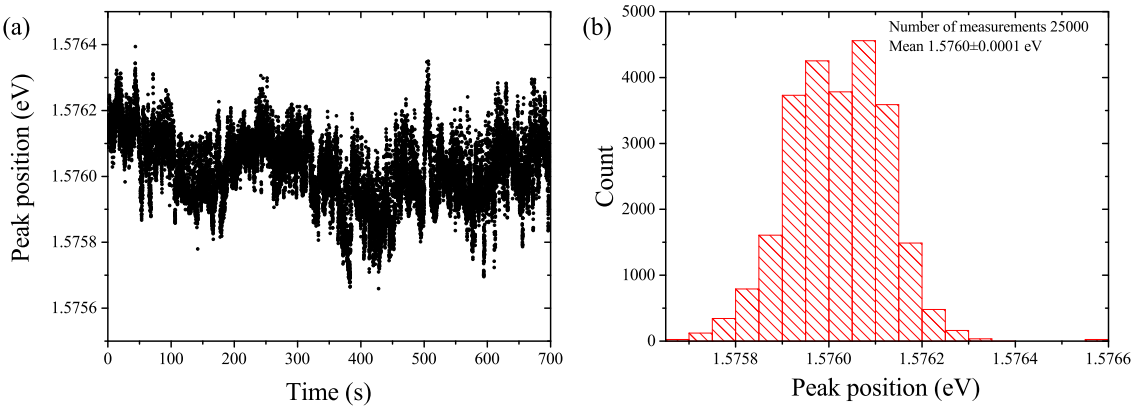

Figure 6.8: Spectral fluctuation as a result of jitter of the lowest energy exciton state of emitter P4 measured upon the resonant excitation of the BS-X state. (a) The positions of the lowest energy excitonic state peak taken over about 12 minutes with a measurement resolution of 28 ms. (b) Histogram of the timetrace data in (a).

6.2.1 High-resolution PLE spectroscopy

The following measurements on emitter E3 were taken by Dr Santosh Kumar and Mauro Brotons-Gisbert.

PLE data recorded on the spectrometer makes it possible to measure detuning with an accuracy of 5 μeV by keeping the excitation laser wavelength fixed, and making use of spectral fluctuations, which provide small detunings from resonance that change for each measurement. The intensity of emission at each measured detuning is extracted. A plot of intensity versus detuning is shown in Fig. 6.9. The black dots represent the data collected when manually scanning the laser wavelength, while the red and the blue dots represent high resolution PLE spectroscopy data. Using high resolution PLE spectroscopy the transitions p0 and p1 along with a phonon sideband were clearly observed. The RF linewidth of peak p1 was measured to be 65.3 ± 1.7 μeV. Similar to emitter P4, PLE spectroscopy reveals the presence of a blue-shifted exciton state detuned by 4.75 meV from transition p1, while its PL signal under non-resonant excitation was strongly suppressed.

6.3 Single photon emission via pumping of a BS-X state

The newly discovered BS-X state can be used to produce high quality single photons. The BS-X state is resonantly excited and emission from the lowest energy excitonic state of emitter P4 at $\lambda = 787.02$ nm is monitored. Using edge filters (see Section 2.2.17) the excitation laser light scattered from the surface of the sample is cut off. The resolution of the edge filter system (2 nm) was narrow enough to suppress the background counts, while transmitting the signal. Fig. 6.10(a) shows the measured data (black dots), the best fit (solid red line), and the calculated deconvolved $g^{(2)}(t)$ (solid blue line). Fig. 6.10(b) gives the probability density distribution of $g^{(2)}(0)$ values. A deconvolved $g^{(2)}(0) < 0.002$ is demonstrated, confirming single photon emission of high purity. The lifetime is equal to 3.50 ± 0.05 ns.

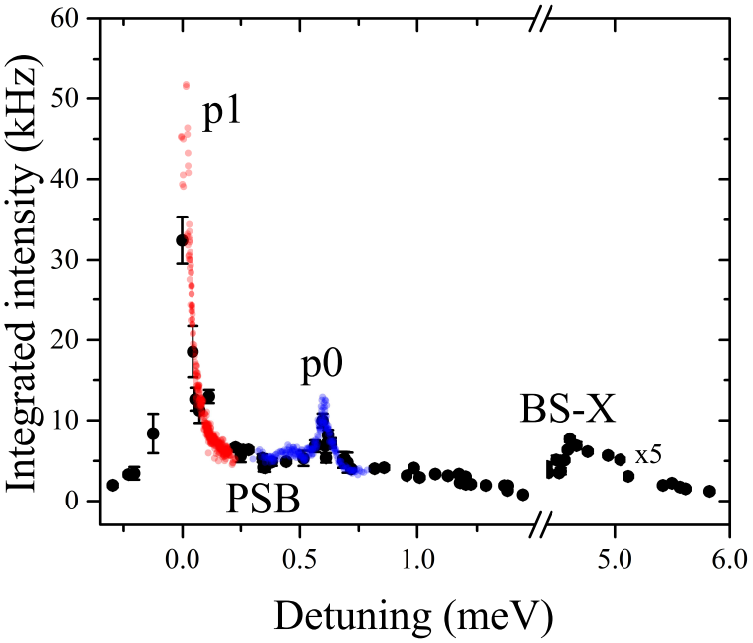

Figure 6.9: Two methods of PLE: the integrated intensity of the brightest peak of emitter E3 measured by manually scanning the laser wavelength (black dots) and by performing high-resolution PLE spectroscopy as a function of detuning. Blue and red data points, representing the latter, were taken at slightly different resonant laser wavelengths (784.38000 nm and 784.40900 nm) to map out peaks p1 and p0. The PLE spectrum shows p1, p0, and BS-X resonances, and a phonon sideband of peak p1.

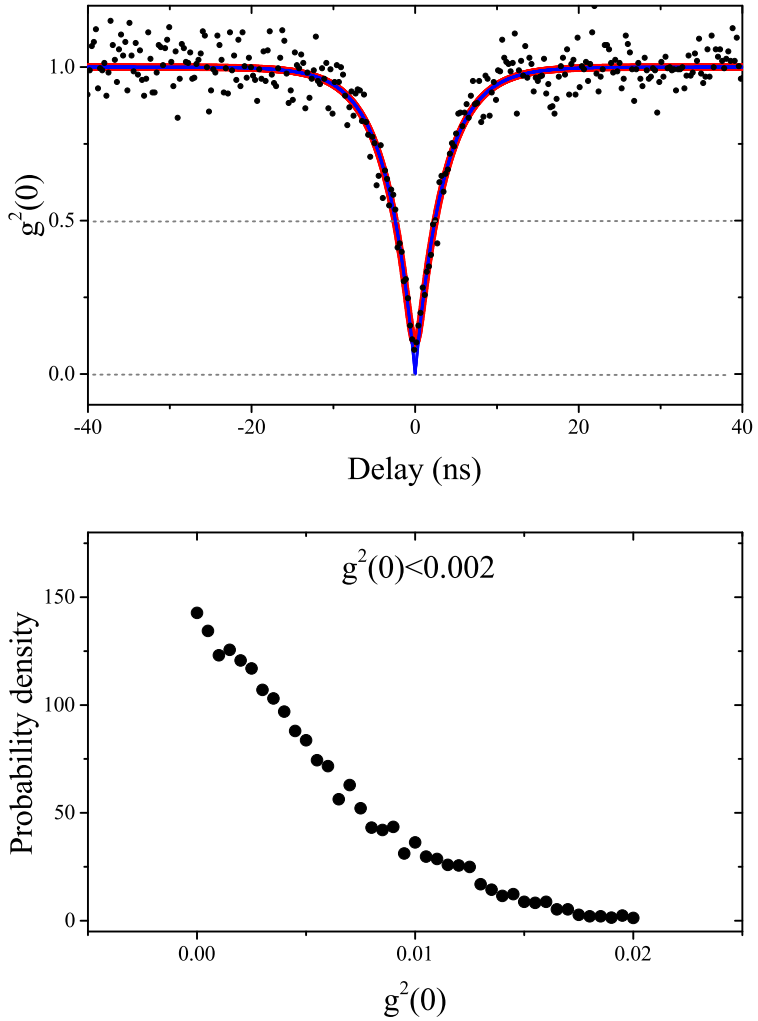

Figure 6.10: (a) Normalized second-order correlation function of the lowest energy transition of bright isolated emitter P4 excited through the BS-X state at 5.250 μW. Time bin size is 256 ps. The solid red (blue) line is the best fit (the calculated deconvolved fit) to the data, demonstrating a deconvolved $g^{(2)}(0) < 0.002$. (b) The probability density distribution of calculated deconvolved $g^{(2)}(0)$ values.

6.4 Discussion and further directions

For the first time, RF has been demonstrated on quantum emitters in a two-dimensional TMD structure, namely a WSe_2 monolayer cooled to 4 K. RF counts were strongly affected by excitation laser detuning from resonance. The tendency of the emitter transition to swiftly shift in energy in relation to the excitation laser energy necessitates longer measurement times and the subsequent post-selection of data. While single photon emission was demonstrated, the dymanic character of RF on these structures as well as its low SBR due to surface roughness are challenges to be overcome. A PLE method was found to lack this disadvantage and produce steady emission.

PLE spectroscopy utilized spectral wandering of transitions to map out resonances with a high resolution. Using PLE, a weakly-fluorescent exciton state blue shifted by about 5 meV from the lowest excitonic state of the emitter is observed. RF from such states was found to be suppressed, with carriers relaxing to the lowest excitonic state before recombination. The quantum nature of photons produced in this way was demonstrated. Such weakly-fluorescent blue shifted exciton states have been observed for at least two quantum emitters in experiments conducted in our lab. Further study is needed to determine whether this is a consistent feature for quantum emitters in WSe_2 monolayers, and whether this can be used to identify the nature of the emitter.

The measurements described in this chapter indicate that quantum emitters localized on defects in WSe_2 monolayers are sources of highly pure single photons, setting the stage for further experiments on these emitters such as on-demand single photon generation, generation of indistinguishable photons, and characterization of the spin and valley coherence.

6.5 References

[1] Hualing Zeng, Junfeng Dai, Wang Yao, Di Xiao, and Xiaodong Cui, Valley polarization in MoS_2 monolayers by optical pumping, *Nature Nanotechnology*, **7**, 490 (2012).

[2] Kin Fai Mak, Keliang He, Jie Shan, and Tony F. Heinz, Control of valley polarization in monolayer MoS_2 by optical helicity, *Nature Nanotechnology*, **7**, 494 (2012).

[3] Ting Cao, Gang Wang, Wenpeng Han, Huiqi Ye, Chuanrui Zhu, Junren Shi, Qian Niu, Pingheng Tan, Enge Wang, Baoli Liu, and Ji Feng, Valley-selective circular dichroism of monolayer molybdenum disulphide, *Nature Communications*, **3**, 887 (2012).

[4] Aaron M. Jones, Hongyi Yu, Nirmal J. Ghimire, Sanfeng Wu, Grant Aivazian, Jason S. Ross, Bo Zhao, Jiaqiang Yan, David G. Mandrus, Di Xiao, Wang Yao, and Xiaodong Xu, Optical generation of excitonic valley coherence in monolayer WSe_2, *Nature Nanotechnology*, **8**, 634 (2013).

[5] Yu-Ming He, Genevieve Clark, John R. Schaibley, Yu He, Ming-Cheng Chen, Yu-Jia Wei, Xing Ding, Qiang Zhang, Wang Yao, Xiaodong Xu, Chao-Yang Lu, and Jian-Wei Pan, Single quantum emitters in monolayer semiconductors, *Nature Nanotechnology*, **10**, 497 (2015).

[6] M. Koperski, K. Nogajewski, A. Arora, V. Cherkez, P. Mallet, J.-Y. Veuillen, J. Marcus, P. Kossacki, and M. Potemski, Single photon emitters in exfoliated WSe2 structures, *Nature Nanotechnology*, **10**, 503 (2015).

[7] Chitraleema Chakraborty, Laura Kinnischtzke, Kenneth M. Goodfellow, Ryan Beams, and A. Nick Vamivakas, Voltage-controlled quantum light from an atomically thin semiconductor, *Nature Nanotechnology*, **10**, 507 (2015).

[8] Ajit Srivastava, Meinrad Sidler, Adrien V. Allain, Dominik S. Lembke, Andras Kis, and A. Imamoğlu, Optically active quantum dots in monolayer WSe_2, *Nature Nanotechnology*, **10**, 491 (2015).

[9] S. Kumar, A. Kaczmarczyk, and B. D. Gerardot, Strain-induced spatial and spectral isolation of quantum emitters in mono- and bilayer WSe_2, *Nano Letters*, **15**, 7567 (2015).

Chapter 7

Conclusion

This thesis describes the investigation of telecommunication wavelength quantum dots (QDs) and excitons believed to be localized on defects in WSe_2 monolayers in microphotoluminescence (μ-PL) spectroscopy and resonance fluorescence (RF) experiments.

The motivation behind the study of telecom wavelength QDs is based on their applications for quantum information transfer over long distances in optical fibers with low attenuation. The effect of the morphology of telecom wavelength QDs on their exciton and carrier properties is examined with an aim of developing these QDs for quantum information applications. Single self-assembled dot-in-a-well (DWELL) structures embedded in a metal-insulator-semiconductor field-effect transistor (MISFET) that emit photons near $\lambda = 1300$ nm were excited non-resonantly and their properties examined under applied electric and magnetic fields. Making use of the Coulomb blockade effect, charge tuning of the device was demonstrated. The Coulomb blockade model revealed large single electron and hole confinement energies, small electron-electron and electron-hole interaction energies of excitons in these structures, demonstrating that electrons in DWELL structures were strongly confined. Stronger electron and hole confinement energies made it possible to tune the exciton transition over a larger wavelength range than comparable devices emitting at 950 nm, opening the possibility of canceling the fine structure splitting (FSS) in telecom wavelength QDs in a MISFET device by applying an external electric field to create sources of entangled photon pairs. By studying the QD PL response on applied electric fields, the permanent dipole moments and polarizabilities of a group of QDs were measured. The diamagnetic coefficients and g-factors of DWELL

dots in magnetic fields in both the Faraday and Voigt geometries are extracted. The exciton g-factors were found to be smaller compared to those of similar dots emitting at 950 nm. The diamagnetic coefficients changed drastically when changing the magnetic field direction from Faraday to Voigt configuration, but did not change considerably with the addition of an extra electron. Finally, time-correlated single photon counting (TCSPC) was used to measure primary and secondary lifetimes of neutral excitons and the lifetimes of charged excitons.

Resonant excitation of QDs offers enhanced coherence of the generated photons as a result of a decreased influence of its material surroundings, promising efficient generation of indistinguishable single photons, generation of on-demand polarization-entangled photons, and characterization of QD spin-dynamics. In this thesis resonance fluorescence of single telecom wavelength QDs at 4 K is reported for the first time. RF from QDs embedded in a MISFET and QDs located within the intrinsic region of a p-i-n diode is demonstrated. In both cases broadening of the RF signal in voltage-detuning spectra accompanied by a low count rate was observed. By modeling the effect of charge noise on RF spectra, we demonstrate that the broadening is a consequence of charge noise. Using high-resolution spectroscopy the Mollow triplet was observed, with Rabi splitting showing a square root dependence on excitation power, as expected. Finally, it was demonstrated that pure dephasing in the system is negligible, and $T_2^{res} \approx 2T_1 \gg T_2^{non-res}$.

Excitons believed to be confined on defects in two-dimensional (2D) transition metal dichalcogenide (TMD) monolayers cooled to 4 K have recently emerged as interesting quantum light sources. However, the nature of their emission is not understood completely. In this thesis, bright single quantum emitters localized on defects in a WSe_2 monolayer belonging to three different groups were identified and characterized in a PL spectroscopy experiment. Polarization-dependent measurements yielded fine-structure splitting (FSS) statistics of neutral excitons belonging to the first group and allowed to identify a candidate for a biexciton localized on a defect. Second-order correlation function measurements on a bright isolated emitter revealed near perfect antibunching, showing that emitters in WSe_2 monolayers are sources of single photons of high purity. For the first time, RF of quantum emitters in a WSe_2 monolayer was achieved. Despite the effect of spectral fluctuations most likely caused by charge noise, single photon emission was demonstrated. Spectral wandering of emission energy was key in performing high-resolution pho-

toluminescence excitation (PLE) spectroscopy. Utilizing PLE we were able to map out resonances and observe weakly-fluorescent blue-shifted exciton states. RF from these states was found to be strongly suppressed, with the carriers relaxing to the lowest excitonic state before recombination. Such emission was demonstrated to be single-photon in nature. These results set the stage for the characterization of spin and valley coherence of localized excitons in TMD monolayers.